
Multiwavelength study of high redshift galaxy clusters

Alessandro Nastasi



Munich, Oktober 2012

Multiwavelength study of high redshift galaxy clusters

Alessandro Nastasi

Dissertation
an der Fakultät für Physik
der Ludwig-Maximilians-Universität
München

vorgelegt von
Alessandro Nastasi

München, den Oktober, 12th, 2012

Erstgutachter: Prof. Dr. Hans Böhringer

Zweitgutachter: Prof. Dr. Gerhard Börner

Tag der mündlichen Prüfung: November, 27th, 2012

Contents

Summary	viii
1 Introduction	1
2 Cosmological context	3
2.1 The dynamics of the universe	3
2.2 Structure formation	5
2.3 Galaxy clusters components	12
2.4 How to detect galaxy clusters	15
2.4.1 Optical selection	15
2.4.2 Color overdensity selection	16
2.4.3 SZ selection	17
2.4.4 X-ray selection	19
2.4.5 Strong and weak Lensing selection	20
2.5 The importance of galaxy clusters	21
2.5.1 Galaxy clusters as cosmological probes	21
2.5.2 Mass proxies for galaxy clusters	24
2.5.3 Clusters as astrophysical laboratories	25
3 The XMM-Newton Distant Cluster Project (XDCP)	29
3.1 Target selection strategy	30
3.1.1 X-ray analysis	30
3.1.2 Photometric follow-up	34
3.1.3 Spectroscopic follow-up	35
3.2 Results	36
4 <i>F</i>-VIPGI: a new pipeline for FORS2 spectroscopy	39
4.1 Introduction	40
4.2 The VIMOS Interactive Pipeline and Graphical Interface	42

4.3	The FORS2-VIMOS Interactive Pipeline and Graphical Interface . . .	42
4.3.1	The FORS2 instrument	43
4.3.2	Conversion of FORS2 files into the VIMOS format	43
4.3.3	F -VIPGI calibration files	45
4.3.4	Wavelength calibration	47
4.3.5	Sky line subtraction and atmospheric absorption corrections .	48
4.3.6	The final product	51
4.3.7	Spectrophotometric calibration	51
4.3.8	Redshift accuracy test	52
4.4	An application to a sample of distant galaxy clusters	54
4.4.1	The spectroscopic sample	55
4.4.2	Spectral indices analysis results	55
4.5	A new library of spectroscopic templates	62
4.5.1	Comparison of the resulting passive template with previous library spectra	65
4.5.2	$U - B$ color of the templates	67
4.6	Summary and conclusion	71
5	The galaxy cluster XMMU J0338.8+0021 at $z = 1.49$	73
5.1	Introduction	73
5.2	Observations, data analysis, and results	74
5.2.1	X-ray selection with XMM- <i>Newton</i>	76
5.2.2	Near-infrared follow-up imaging	76
5.3	Spectroscopic analysis	77
5.3.1	Data reduction	77
5.3.2	Redshift measurements	78
5.4	A young cluster in formation?	81
5.5	Summary and conclusion	83
6	Kinematic analysis of a sample of distant galaxy clusters	87
6.1	Introduction	88
6.2	The HIFLUGCS sample	89
6.3	The distant cluster sample	90
6.3.1	The literature sample	90
6.3.2	The XDGP sample	92
6.4	X-ray analysis	93
6.5	Spectroscopic reduction	94
6.6	Kinematic analysis	95

6.6.1	Introduced bias	96
6.6.2	Test on accuracy of velocity dispersion measurements	96
6.7	Results	97
6.7.1	The $L_X - \sigma_v$ relation	99
6.7.2	The $L_X - T_X$ relation	99
6.7.3	The $\sigma_v - T_X$ relation	101
6.8	Summary and conclusion	103
7	Summary and Conclusions	107
A	Additional information on F-VIPGI	111
A.1	Compatibility with the current operating systems	111
A.2	How to obtain F -VIPGI	112
A.3	Link for spectroscopic templates	112
B	Redshifts list of “XDCP sample” clusters	113
C	Velocity histograms of “literature sample” clusters	125
	Acknowledgements	129

Untersuchung von Galaxienhaufen bei hoher Rotverschiebung in verschiedenen Wellenlängenbereichen

Zusammenfassung

Galaxienhaufen sind die massereichsten gravitationsgebundenen Objekte im Universum und als solche befinden sie sich an den Kreuzungspunkten des kosmischen Netzes der großräumigen Struktur. Durch das hierarchische Strukturwachstum bilden sich Galaxienhaufen relativ spät und daher können Untersuchungen bei hohen Rotverschiebungen ($z > 0.8$) wichtige Informationen zur beschleunigten Ausdehnungsrate des Universums liefern, die wiederum mit der Zustandsgleichung (equation of state) der *Dunklen Energie* zusammenhängt. Darüberhinaus sind entfernte Galaxienhaufen einzigartige Umgebungen, um eine Fülle an Erkenntnissen zur Entstehung, Wechselwirkung und Rückkopplungsprozessen über die in ihnen enthaltenen Galaxien zu gewinnen.

All diese Aspekte verdeutlichen die Bedeutung der Untersuchung der Galaxienhaufenpopulation, um wertvolles Wissen zum kosmologischen Weltbild und Galaxienentwicklungsmodellen zu erlangen. Insbesondere ist eine bessere Erforschung von Eigenschaften der noch immer wenig verstandenen *entfernten* Galaxienhaufen bei Rotverschiebungen von $z > 0.8$ von großer Bedeutung, was Rückschauzeiten (look-back times) von mehr als der Hälfte des Alters des Universums entspricht.

Ziel der vorliegenden Doktorarbeit ist die Untersuchung der Eigenschaften dieser entfernten Galaxienhaufensysteme, um herauszufinden, wie sie sich von gegenwärtigen Objekten unterscheiden und somit deren Evolution mit der Rotverschiebung zu beschreiben. Zu diesem Zweck untersuchte ich eine Stichprobe von röntgenhellen, entfernten Galaxienhaufen aus dem XMM-*Newton* Distant Cluster Project (XDCP). XDCP ist eine Durchmusterung (survey) mit der speziellen Zielsetzung, die entferntesten, röntgenhellen Galaxienhaufen bei $z > 0.8$ in XMM-*Newton* Archivdaten zu entdecken und zu charakterisieren. Die Beobachtungsstrategie und Ergebnisse dieses Projektes werden in Kapitel 3 präsentiert.

Innerhalb von XDCP hat sich meine Arbeit auf die optischen spektroskopischen Folgeuntersuchungen von potenziellen entfernten Galaxienhaufen fokussiert. Für diese Aufgabe habe ich als Teilprojekt meiner Arbeit ein halbautomatisches Datenreduktionssystem mit dem Namen *F-VIPGI* entwickelt, das diesen entscheidenden Schritt der Projektarbeit wesentlich schneller und effizienter macht. Durch *F-VIPGI*, das von mir auch öffentlich bereitgestellt wird, konnte in den letzten beiden Jahren die spektroskopische Bestätigungsrate von entfernten XDCP Galaxienhaufen wesentlich gesteigert werden. Die verbesserte Qualität der spektroskopischen Re-

duktion durch das neue Softwarepaket erlaubte auch erstmals die Möglichkeit, die spektroskopische Bestätigung von entfernten Galaxienhaufen bis in die vorher unerforschte “Rotverschiebungswüste” (“redshift desert”) bei $z \geq 1.5$ voranzutreiben. Als Demonstration dieser Möglichkeiten zeige ich in Kapitel 5 eine Analyse des neu entdeckten XDCP Galaxienhaufens XMMU J0338.8+0021 bei $z = 1.49$ in verschiedenen Wellenlängenbereichen.

Als weitere Anwendung der neuen *F*-VIPGI Einsatzmöglichkeiten habe ich die spektro-photometrischen Eigenschaften von 186 Haufengalaxien aus 16 XDCP Galaxienhaufen im Rotverschiebungsbereich $0.65 < z < 1.25$ untersucht. In dieser Arbeit, die in Kapitel 4 vorgestellt wird, habe ich herausgefunden, dass die *passiven* Mitgliedsgalaxien der entfernten Galaxienhaufen eine (U–B)-Farbe im Ruhesystem aufweisen, die *roter* ist als von vergleichbaren Feldgalaxien, aber nahezu identisch zu den passiven Galaxien in nahen Haufen. Diese Ergebnisse deuten auf eine Schlüsselrolle der Umgebung in Bezug auf die Regulierung der Aktivität der Sternentstehung in Galaxien hin und stimmen gut mit den Schlussfolgerungen mehrerer neuerer Studien von anderen Autoren überein.

Des weiteren habe ich noch die Skalierungsrelationen zwischen Röntgenobservablen (L_X , T_X) und der Geschwindigkeitsdispersion (σ_v) von Galaxien in einer Stichprobe von entfernten XDCP Haufen untersucht. Die Motivation für diese Analyse, die in Kapitel 6 vorgestellt wird, war die Suche nach Abweichungen zu den Skalierungsrelationen von lokalen Galaxienhaufen, die möglicherweise auf veränderte Röntgeneigenschaften des heißen Innerhaufengases durch nicht-gravitativ Prozesse innerhalb der Entwicklungszeitspanne hindeuten können.

Summary

Clusters of galaxies are the most massive gravitationally bound systems in the universe and they are placed in the nodes of the web of the large scale structure. Due to their hierarchical growth, they have formed relatively late and, because of that, the study of the cluster population toward high redshift ($z > 0.8$) can provide outstanding information on the acceleration rate of the universe and, hence, on the equation of state of *dark energy*. In addition, distant clusters are unique environments able to provide a wealth of information on the formation, interaction and feedback processes of their hosted galaxies.

All the above mentioned aspects make clear the importance of investigating the galaxy cluster population in order to provide precious knowledge on cosmological and galaxy formation models. In particular, it is crucial to unveil the characteristics of the still poorly known *distant* galaxy clusters residing at $z > 0.8$, corresponding to lookback times of more than half of the age of our universe.

The goal of this thesis is to study the properties of these different systems and to find out how they differ from the present day clusters and thus to describe their evolution with redshift. To this aim I have used a sample of X-ray luminous distant galaxy clusters drawn from the XMM-*Newton* Distant Cluster Project (XDCP). XDCP is a survey aimed at discovering and characterizing the most distant ($z > 0.8$) X-ray luminous galaxy clusters serendipitously detected in XMM-*Newton* observations. The strategy and the results of this survey are presented in Chapter 3.

Within XDCP, my work has been focussed on the optical spectroscopic follow-up of systems flagged as potential distant clusters. In this context, part of my work has been devoted to developing a new semi-automated pipeline (*F*-VIPGI) aimed at carrying out this crucial step in a faster and more efficient way. Thanks to *F*-VIPGI, the spectroscopic confirmation rate of distant XDCP clusters has received a significant boost in the last couple of years and the pipeline itself will be publicly released. The improved quality of the spectroscopic reduction, guaranteed by the new software, also enabled the possibility of pushing the spectroscopic confirmation of distant clusters into the previously deserted redshift range $z \geq 1.5$, the so-called “*redshift desert*”. As a demonstration of this, in Chapter 5 I present a multi-wavelength study of XMMU J0338.8+0021, a newly discovered XDCP cluster at $z = 1.49$.

As a further application of the new *F*-VIPGI capabilities, I have investigated the spectro-photometric properties of 186 galaxy members residing in 16 XDCP clusters with redshift $0.65 < z < 1.25$. In this work, discussed in Chapter 4, I have found that the *passive* galaxies residing in distant clusters exhibit a rest-frame (U–B) color *redder* than the coeval ones in the field but similar to the passive members of nearby

clusters. These results point toward a key role of the environment in regulating the activity of star formation in galaxies residing in it, a finding in agreement with results recently reported by other authors.

Finally, I have also studied the scaling relations between the X-ray observables (L_X , T_X) and the galaxy velocity dispersion (σ_v) in a sample of distant XDCP clusters. The motivation of this study, presented in Chapter 6, was to look for deviations from the trends observed in the local clusters, possibly indicative of non-gravitational processes that altered the X-ray properties of the hot intracluster medium throughout the clusters' lifetimes.

Chapter 1

Introduction

The aim of this thesis is a multi-wavelength study of a sample of X-ray luminous, distant galaxy clusters drawn from the XMM-*Newton* Distant Cluster Project (XDCP).

I start my thesis (Chapter 2) by discussing the cosmological framework and the importance of galaxy clusters, both as cosmological probes and astrophysical laboratories, allowing us to study the large variety of physical events intervening during the galaxy formation and evolution processes. I particularly stress the key role of the *distant* clusters in this context and, hence, the main reasons that motivated the start of the XMM-*Newton* Distant Cluster Project, discussed in Chapter 3, to which I actively contributed with the work presented in this thesis. More specifically, the need of a more efficient and fast reduction of the optical spectra of distant cluster members, motivated the development of a new semi-automated pipeline able to accomplish the above requirements. Part of my work has been devoted to the realization of such a software (*F-VIPGI*), which is presented in Chapter 4. In the same chapter I also present an application of the new software to a sample of 16 newly discovered XDCP clusters carrying out a spectro-photometric study on their galaxy members.

In Chapter 5, I present the multi-wavelength study of XMMU J0338.8+0021, one of the most distant XDCP clusters I spectroscopically confirmed.

In Chapter 6, I study the scaling relations between the X-ray observables (L_X , T_X) and the galaxy velocity dispersion (σ_v) of a sample of distant clusters.

Finally, in Chapter 7 I summarize the presented work and how it improved the knowledge of the galaxy cluster population in the high redshift regime.

Chapter 2

Cosmological context

2.1 The dynamics of the universe

The currently accepted cosmological model (Peebles 1993; Padmanabhan 1993; Peacock 1999) assumes that the universe started from a hot state where primordial density fluctuations were created during the *inflationary* phase (Guth 1981) that exponentially increased the early universe by a factor of $\sim 10^{78}$ in volume. The peaks of the density perturbations, initially connected with the Hubble flow, eventually decoupled from it under the action of self-gravity that stopped and then turned around the local expansion process leading to the formation of galaxies and clusters.

The dynamics of the universe can be described with a time-dependent, dimensionless scale factor $a(t)$ which is proportional to the evolving mean distance between galaxies at time t . The scale factor is related to the Hubble parameter, which represents the expansion rate of the universe, by the relation

$$H(t) = \frac{\dot{a}(t)}{a(t)} \quad (2.1)$$

and to the redshift, z , of a source whose radiation is emitted at a time t_{em} and observed at t_{obs} by

$$1 + z = \frac{a(t_{obs})}{a(t_{em})} . \quad (2.2)$$

From the former equation, the relation $v = (\dot{a}/a)|_{t_0} \cdot d$, expressing the apparent recession velocity v of a galaxy with respect to another one at a distance d , can be written as $v = H(t_0) \cdot d$; the well known Hubble Law. The value of the Hubble parameter at the current time t_0 is the so-called Hubble constant $H(t_0) = H_0$, whose value has been

accurately constrained from the calibrated magnitude-redshift relation¹ based on 253 Type Ia supernovae (SNe Ia) to $H_0 = 73.8 \pm 2.4 \text{ km s}^{-1} \text{ Mpc}^{-1}$ (“Supernovae and H0 for the Equation of State” (SH0ES) project, Riess et al. 2011)². Authors often refer to the normalized value of H_0 by using the dimensionless quantity $h = H_0/100 \text{ km s}^{-1} \text{ Mpc}^{-1}$.

The scale factor $a(t)$ also enters in the definition of the *deceleration* parameter

$$q \equiv -\frac{\ddot{a}a}{\dot{a}^2} ,$$

where $q > 0$ is for a *decelerating* ($\ddot{a} < 0$) universe and $q < 0$ is for an *accelerating* ($\ddot{a} > 0$) one.

For large enough ($> 100 \text{ Mpc}$) scales, our universe can be assumed *homogeneous* and *isotropic* and, only in this case, its metric can be described by the Robertson – Walker (RW) expression (Peacock 1999)

$$ds^2 = c^2 dt^2 - a(t)^2 \left(\frac{dr^2}{1 - kr^2} + r^2(d\theta^2 + \sin^2\theta d\phi^2) \right) , \quad (2.3)$$

where r , θ and ϕ are the spherical coordinates and k is the curvature parameter of the universe. The latter can assume the values $k < 0$ for an *open* universe with eternal expansion; $k = 0$ for a *flat* universe (where, in the case there is no dark energy component, the expansion stops at $t = \infty$); $k > 0$ for a *closed* universe characterized by the stop of the expansion and turnaround of the motion, eventually resulting in the collapse of the universe in a finite time.

Inserting the RW metric (Eq. 2.3) into the field equation of General Relativity, which describes the gravitational attraction between masses in terms of a space-time curvature caused by its matter and energy distribution, one can obtain the Friedmann – Lemâitre equations

$$\frac{\ddot{a}}{a} = -\frac{4\pi G}{3} \left(\rho + \frac{3p}{c^2} \right) + \frac{\Lambda c^2}{3} , \quad (2.4)$$

and

$$\left(\frac{\dot{a}}{a} \right)^2 = \frac{8\pi G}{3} \rho - \frac{kc^2}{a^2} + \frac{\Lambda c^2}{3} , \quad (2.5)$$

¹The apparent magnitude m of a source is a function of its real magnitude M and its *luminosity distance*, $d_L(z, H_0, \Omega_m, \Omega_\Lambda)$, as: $m = M + 5 \log(d_L) + 25$. Here d_L is expressed in Mpc and Ω_m and Ω_Λ are the dimensionless *energy densities* defined in Eq. 2.6.

²The current most tight constraint of H_0 is, however, obtained by combining the results of the 7-years WMAP mission with studies on the baryonic acoustic oscillations (BAO) and SNe Ia and corresponds to $H_0 = 70.2 \pm 1.4 \text{ km s}^{-1} \text{ Mpc}^{-1}$ (Komatsu et al. 2011).

where ρc^2 is the matter-energy density, p is the associated pressure and Λ is Einstein's cosmological constant. Λ owes its name to the fact that it was originally introduced by Albert Einstein as a modification of his original theory of General Relativity to achieve a stationary universe. It corresponds to a vacuum energy with a density of

$$\rho c^2 = \frac{\Lambda c^4}{8\pi G}$$

and an equation of state $p = -\rho_\Lambda c^2$, with a *negative* pressure component.

The above Friedmann equations can be solved by assuming an equation of state for each component of the universe that dominates at different cosmic epochs. Specifically, the equation of state is usually assumed to be the form of a perfect fluid $p = w\rho c^2$, with $w = 0$ for matter (ρ_m), $w = \frac{1}{3}$ for radiation (ρ_r) and $w = -1$ for the vacuum energy associated with the cosmological constant (ρ_Λ). The contribution to the total density of the universe associated with the different components can be expressed in terms of their dimensionless *energy densities*, $\Omega_i = \rho_i/\rho_{crit}$, i.e., the density of the i -th component relative to the critical density, $\rho_{crit} = 3H_0/8\pi G = 1.9 \cdot 10^{-29} h^2 \text{ M}_\odot \text{ Mpc}^{-3}$

$$\Omega_m = \frac{\rho}{\rho_{crit}} , \Omega_\Lambda = \frac{\Lambda c^2}{3H_0^2} , \Omega_r = \frac{8\pi G \rho_r}{3H_0} . \quad (2.6)$$

In addition, the parameter which describes the curvature density of the universe is defined as

$$\Omega_k = 1 - (\Omega_m + \Omega_\Lambda + \Omega_r) ,$$

that is equal to zero within an uncertainty of ± 0.007 (Komatsu et al. 2011), consistent with a flat spatial metric on cosmic scales.

All the previous density parameters are defined with respect to their values corresponding in the present universe at t_0 . Their dependence on redshift is shown in Fig. 2.1.

2.2 Structure formation

According to the standard model of structure formation and evolution, $\sim 380,000$ years after the Big Bang (or, equivalently, at $z \sim 1100$) the primordial optically thick photon-baryon plasma cooled below 3000 K and nuclei could start to capture

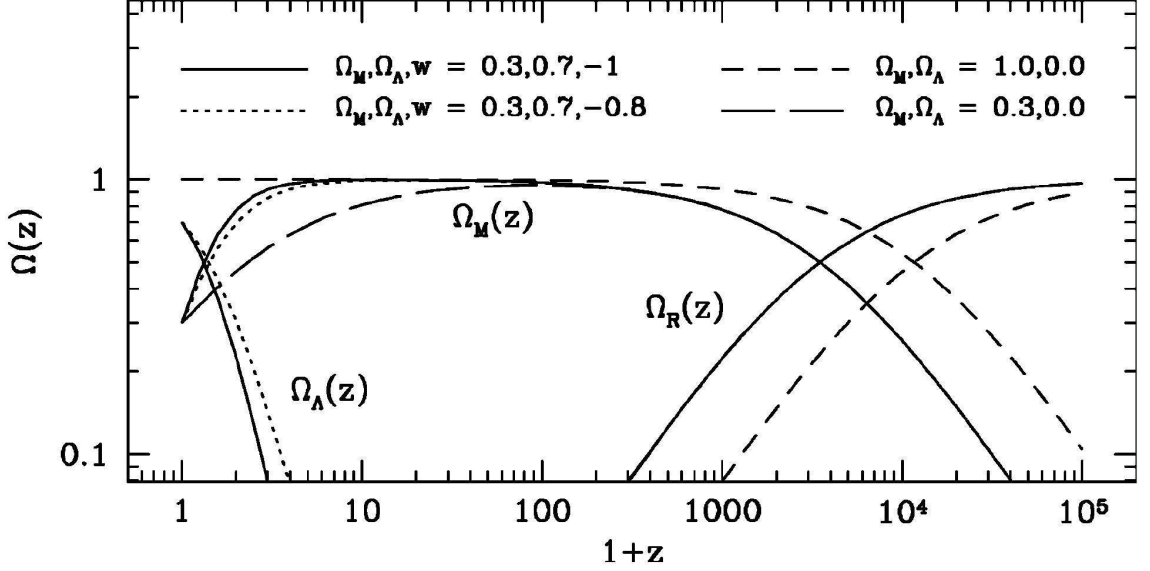


Figure 2.1: Energy density curves of the three main components of the universe (matter, radiation and dark energy) as a function of redshift and for different cosmological models. The plot shows how radiation, matter and dark energy alternately dominated throughout the history of the universe, with Ω_Λ starting to take over only from $z \leq 0.5$. Plot from Voit (2005).

and retain electrons. Owing to the reduced number of free electrons the Thomson scattering rate dropped and the photon mean free path became infinite, thus making the universe optically thin. This epoch, named the *recombination era*, marks the origin of the Cosmic Microwave Background (CMB) from the *last scattering surface*³ and the *decoupling* of radiation and baryonic matter. However, the recombination era also marks the epoch in the history of the universe when the first inhomogeneities in the density field of the baryonic matter could start to be amplified. In fact, without any radiative pressure opposing gravitational collapse, the local density fluctuations of baryonic matter could condensate and grow in mass. The density contrast of the fluctuations with respect to the mean density of the universe at any time is defined as

$$\delta_m(\vec{x}, t) = \frac{\rho_m(\vec{x}, t) - \rho_m(t)}{\rho_m(t)} \quad (2.7)$$

³Due to the tail of high energy photons in the primordial energy distribution, recombination was not *instantaneous*. Therefore, it would be more appropriate to refer to the region from where CMB originated as the last scattering *thick shell*.

with $\rho_m(\vec{x}, t)$ being the density of the fluctuations at given position \vec{x} at a time t and $\rho_m(t)$ being the mean density of the matter in the universe at the same time. The characterization of the density field is usually done in Fourier space, and so the density contrast is converted, i.e., $\delta_m(\vec{x}, t) \mapsto \delta_m(\vec{k}, t)$, by

$$\delta_m(\vec{k}, t) = \int d^3x \delta_m(\vec{x}, t) e^{i\vec{k} \cdot \vec{x}} . \quad (2.8)$$

The key quantity containing the statistical properties of $\delta_m(\vec{x}, t)$ is the averaged squared density fluctuations in the Fourier space, i.e. the *power spectrum*

$$P(\vec{k}, t) = \left\langle |\delta_m(\vec{k}, t)|^2 \right\rangle , \quad (2.9)$$

usually expressed in dimensionless units as

$$\Delta^2(k) \equiv \frac{k^3 P(k)}{2\pi^2} . \quad (2.10)$$

It has to be noted that, before the baryonic density fluctuations, the first overdensity that started to form and accrete was actually the *cold-dark matter* (CDM). This form of matter, experiencing only gravitational interactions, was not coupled with the photon-baryonic fluid during the radiation era. Hence, CDM fluctuations started to grow well before the decoupling epoch. This effect had a crucial consequence in the following structure formation process, as when recombination took place, the baryonic matter collapsed into the potential wells already created by the CDM, which thus significantly shortened the structure formation timescales. From now on all the aforementioned expressions describing the baryonic density fluctuations will be referred only to the CDM since this is the main driver of the matter density perturbation growth.

The evolution of the primordial fluctuations can then be followed by assuming that they grew only via gravitational interactions and by considering the accreting matter as an *ideal fluid*. If perturbations are small enough ($|\delta_m(\vec{x})| \ll 1$) systems evolve in the *linear regime*, as the nonlinear couplings between the various perturbation components (baryonic matter, dark matter, radiation and dark energy) are negligible. In this way, a linearized set of fluid equations are obtained and, together with the equation of motion (Euler's equation), the Poisson equation and the continuity equation (expressing the conservation of mass), they can be fully solved.

The final equation describing the evolution of the perturbations is a second order differential equation with the form

$$\ddot{\delta} = -2\frac{\dot{a}}{a}\dot{\delta} + 4\pi G\rho_m\delta , \quad (2.11)$$

where G is the gravitational constant. We recall here that the Hubble parameter $H(t)$, describing the expansion rate of the universe, is

$$H(t) \equiv \frac{\dot{a}}{a} ,$$

and acts as a “drag” term in Eq. 2.11, i.e., local overdensities are “stretched” as a consequence of the cosmological expansion, which opposes the collapse of the density perturbations. This effect is counteracted by the gravitational term on the right of Eq. 2.11, which then has two solutions: (i) a growing (D_g), and (ii) a decaying (D_d) mode, with the latter having no physical interest. It is interesting to note that, as Eq. 2.11 only has time (partial) derivatives, its solutions do not depend on the cosmic location \vec{x} : hence, the perturbations will grow with the **same rate at every location and at every scale**. This implies that, in the linear regime, the power spectrum will evolve *parallel* to itself and, at a certain cosmic epoch t_1 , it will be described by

$$P(k, t_1) = P(k, t_0)W^2(k)\frac{D_g(t_1)}{D_g(t_0)} , \quad (2.12)$$

where $W(k)$ is the *transfer function*, encoding the deviation of the power spectrum from a simple primordial power law $P(k, t_0) \propto k^n$. Many inflationary models predict, in fact, that the primordial power spectrum had a power-law form $P(k) = Ak^n$, with a preferred Harrison-Zel’dovich form ($n = 1$) (Harrison 1970; Zeldovich 1972). However, the growth of the fluctuations on particular scale-lengths can be suppressed for various reasons, including the exact values of the parameters describing the underlying cosmology, which changes the shape of the primordial power spectrum.

In 1992 the NASA satellite COBE (and more recently the satellite WMAP) detected for the first time (and studied in greater detail) the CMB anisotropies over a temperature scale of $\sim 10\text{--}30 \mu\text{K}$ (see. Fig. 2.2), with the average temperature of the CMB assessed to be $T_{CMB} \simeq 2.73 \text{ K}$. Assuming each perturbation as *adiabatic*, i.e., energetically isolated from the surrounding environment, the observed fluctuations translate into a corresponding density fluctuation

$$\frac{\Delta T}{T} \approx \frac{\Delta \rho_m}{\rho_m} = \delta_m \approx 10^{-5} . \quad (2.13)$$

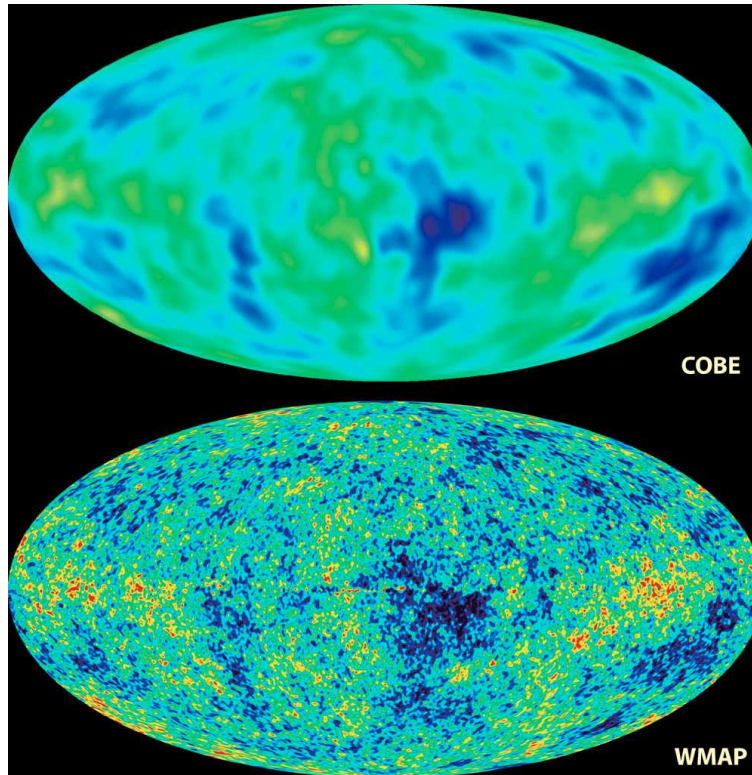


Figure 2.2: The Cosmic Microwave Background as seen by COBE (top) and WMAP (bottom) after the removal of the dipole and galaxy contributions. The red and blue spots are the hotter and colder regions of the CMB, respectively. Credits: NASA.

This observational result revealed that $\delta_m \ll 1$ for the primordial perturbations and, hence, that the linear approximation was indeed capable of describing the evolution of the density fluctuations, at least at the earliest times.

The *seeds* of the inhomogeneities we observe in the universe today then grew in mass and size by “swallowing” the neighbour ones. Therefore, this process followed a bottom-up hierarchy, with the most massive systems being formed only at later times. However, as the perturbations increase in density with time, the density contrast reaches $\delta(\vec{x}, t) \sim 1$ and thus the process enters the *non-linear* regime. From this point on, differences among the various mass contributions to the perturbation field cannot be neglected anymore and following evolution of the structures is a problem that can only be solved *numerically*.

The *Millennium Simulation* (Springel et al. 2005) and the *Millennium XXL* (Angulo et al. 2012) are, to date, the highest quality representations of this approach and

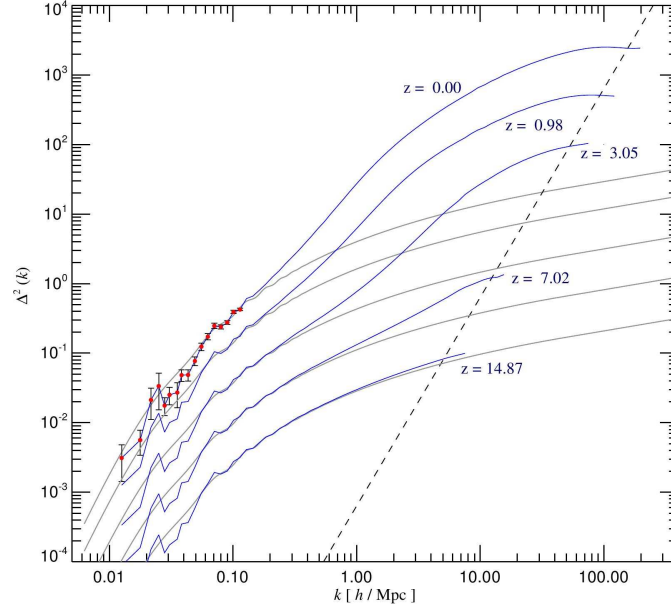


Figure 2.3: The time evolution of the dark matter power spectrum in the Millennium Simulation. Gray curves represent the power spectrum predicted in case of linear growth, while the blue ones are the “real”, simulated trends. The dashed line is the shot-noise limit, while the red points and their errorbars are plotted only for indicating the bin sizes and sample variance. In this figure it can be appreciated that the linear evolution (gray lines) of the power spectrum with time is overall consistent with a *shift* with respect to the ones at earlier epochs. However, there is also a deviation from the simple power law $P(k) \propto k^n$ of the primordial power spectrum. As time increases it is also clear that the non-linear regime encompasses larger physical scales (left side of the plot) albeit at $z = 0$ the largest systems (> 10 Mpc) are still found in the linear regime. Fluctuations on the largest scales are due to the limited volume of the simulation $(500h^{-1}\text{Mpc})^3$. Plot from Springel et al. (2005).

provide insightful contributions to understand and fully characterize the formation and distribution of the large scale structures observed in our universe (see Fig. 2.3).

One way to express how dark matter halos are distributed in the universe as a function of time is via the *mass function*, which gives the number of systems with mass in the range $(M, M + dM)$ at a given redshift z . In the *Press-Schechter* formalism (Press & Schechter 1974), dark matter haloes experiencing spherical collapse

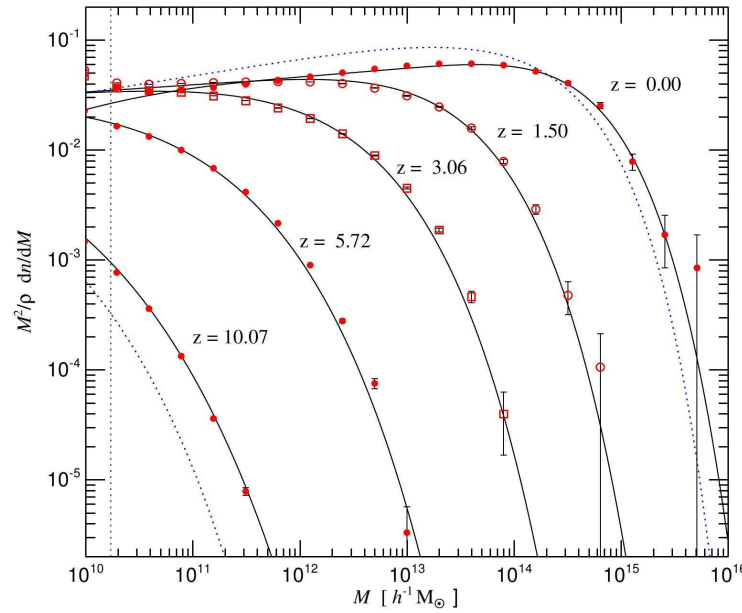


Figure 2.4: Differential dark matter halo number density as a function of mass and redshift in the Millennium Simulation. The dotted curves are the Press-Schechter model at $z = 10$ and $z = 0$ while the solid lines are the prediction from the empirical Jenkins fitting formula (Jenkins et al. 2001). Plot from Springel et al. (2005).

and hierarchical clustering, have the following mass function:

$$\frac{dn(M, z)}{dM} = \left(\frac{2}{\pi}\right)^{\frac{1}{2}} \frac{\rho_m}{M^2} \frac{\delta_c}{\sigma_M(z)^2} \left| \frac{d \log \sigma_M(z)}{d \log M} \right| \exp \left(-\frac{\delta_c^2}{2\sigma_M(z)^2} \right) dM, \quad (2.14)$$

where δ_c is the linearly extrapolated critical density contrast, σ is the variance of the linear density field smoothed over a mass scale M ,

$$\sigma^2 \equiv \langle |\delta M / M|^2 \rangle \quad (2.15)$$

and ρ_m is the mean matter density of the universe. Eq. 2.14 also depends on cosmological parameters through δ_c and, especially, $\sigma_M(z)$, the latter being connected to the power spectrum, $P(k)$, and the cosmological density parameters. In the limit of very massive objects the mass function is dominated by the exponential term. This implies that Eq. 2.14 becomes *exponentially* sensitive to the underlying cosmology in the mass regime of galaxy clusters, thus making these systems particularly powerful probes to test different cosmological models (see Sec. 2.5.1).

An example of the dark matter mass function and its evolution in the redshift range $10 \geq z \geq 0$ predicted by the Millennium Simulation is illustrated in Fig. 2.4. This figure clearly shows the increase of the characteristic value of M beyond which the exponential regime starts to dominate with time due to the bottom-up accretion of inhomogeneities and its transition into the galaxy clusters domain ($M > 10^{14} h^{-1} M_{\odot}$) for $z < 1.5$.

In conclusion, galaxy clusters are the final results of the coalescence of the primordial small DM fluctuations and represent the most massive gravitationally bound system in the universe. Since they sit on the top of the hierarchical formation process, they are actually the *most recently* formed systems. They are characterized by a total mass of $M \sim 10^{14} - 10^{15} M_{\odot}$ and, as shown in Fig. 2.4, they populate the exponential tail of the mass function at $z \lesssim 1.5$.

2.3 Galaxy clusters components

Galaxy clusters are typically characterized by a total mass of $M \sim 10^{14} - 10^{15} M_{\odot}$, a size of $\sim 1 - 3$ Mpc and $\sim 10^2 - 10^3$ member galaxies. Although dark matter is by far the dominating component of such a mass reservoir, baryonic matter makes a significant ($\geq 10\%$) fraction of the total mass. Specifically, the total cluster mass can be separated into three main components (see Fig. 2.5):

(i) Dark Matter Halo: it contributes $80\% - 87\%$ to the entire mass. One of the most remarkable findings of modern numerical simulations is that dark matter haloes within clusters exhibit a *universal* distribution that does not depend on the cluster mass and follows the so-called “Navarro-Frenk-White” (NFW, Navarro et al. 1997) profile

$$\rho(r) = \frac{\rho_0}{\left(\frac{r}{r_s} \left(1 + \frac{r}{r_s}\right)\right)^2}, \quad (2.16)$$

where ρ_0 is the central density and r_s is a characteristic scale length.

(ii) Intracluster Medium (ICM): it makes $11 - 15\%$ of the total mass and represents the dominant component of baryonic matter in clusters. In order to counteract the gravitational pull associated with the DM potential well, the intracluster medium confined within it reaches virial temperatures of $10^7 - 10^8$ K. Thus, the ICM is highly ionized and it strongly emits in X-ray via the thermal bremsstrahlung (free-free) process, whose specific emissivity, i.e., the luminosity per unit volume and

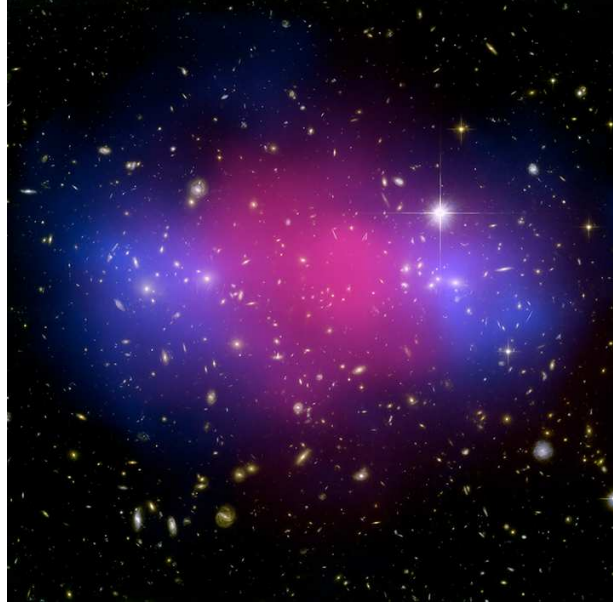


Figure 2.5: The composite color image of the galaxy cluster MACS J0025.4-1222 at $z = 0.586$ published by Bradač et al. (2008). Overlaid onto the Hubble Space Telescope image of the galaxies is the X-ray emission from the ICM detected by Chandra (in pink) and the DM distribution as inferred from the weak and strong lensing analysis (in blue). The system actually consists of two subclusters experiencing a major merger, which produces a remarkable offset between the DM and the ICM distributions.

frequency interval, is given by

$$\epsilon_\nu = 6.8 \times 10^{-38} Z_i^2 n_e n_i g^{ff}(\nu, T) \frac{e^{-\frac{h\nu}{k_B T}}}{\sqrt{T}} \text{ erg s}^{-1} \text{ cm}^{-3} \text{ Hz}^{-1}, \quad (2.17)$$

where h here represents the Planck constant, Z_i is the ion charge, n_e and n_i are the number densities of electrons (a typical value is $n_e \sim 10^{-3} \text{ cm}^{-3}$) and ions, respectively, and $g^{ff}(\nu, T)$ is the Gaunt factor, which takes into account corrections for quantum mechanical effects and distant collisions and has a value of approximately unity. From Eq. 2.17 it is evident that the X-ray emissivity strongly depends on the matter density ($\epsilon_\nu \propto n^2$), so that a very high surface brightness emission emerges from the innermost, densest regions of clusters. Since the amount of diffuse hot gas in clusters is significantly higher than galaxies, the ICM is believed to have a cosmological origin, i.e. it originated through infalling cold gas that was shock heated to

the virial temperature. However, as it shows non-primordial metal abundances ($Z \sim 0.3 Z_{\odot}$), at least part of the diffuse gas in clusters should have been ejected by galaxies. For temperature of $T_X \leq 2$ keV the ionization level of the ICM metals decreases and a considerable fraction of energy is then emitted via *recombination radiation* (free-bound) and line emission radiation (bound-bound). The most important X-ray line feature is the K-shell line of FeXXVI at ~ 6.7 keV.

The ICM electrons can interact with the low-energy photons of the Cosmic Microwave Background (CMB) via inverse Compton scattering as a results of their high kinetic energies. This results in the spectrum of the CMB to be significantly distorted in correspondence with the location of a cluster, producing the so-called Sunayev – Zel’dovich effect. This effect can be used to detect the most massive clusters of the universe, without *any* limitation on the maximum accessible redshifts. This aspect is further discussed in Sec. 2.4.

(iii) Galaxies: their contribution to the total mass is only a few per cent (2 – 5%) and they enclose the baryonic matter in the condensed state in the form of stars or cold gas. Galaxies trace the depth of the gravitational potential, and under the assumption of a virial equilibrium, their velocity dispersion σ_v is closely related to the total mass as (Longair 1998)

$$M(R, \sigma_v) = \frac{3\sigma_v^2 R}{G} = 6.9 \times 10^{14} \left(\frac{\sigma_v}{10^3 \text{ km s}^{-1}} \right)^2 \cdot \left(\frac{R}{1 \text{ Mpc}} \right) M_{\odot} . \quad (2.18)$$

Many observational results show that the population of galaxies in clusters is dominated by passive and old galaxies, preferentially located in the most central regions. These galaxies ended the formation of their stars at redshift $z \geq 2$. Such a population of “red and dead” galaxies usually exhibits a very tight scatter in color ($\lesssim 0.05$ mag), which defines a **red-sequence** in a color-magnitude diagram (Baum 1959). The study of this feature, observed in clusters up to $z \sim 1.3$, can provide constraints on the galaxy formation processes (see Sec. 2.5.3) and also be used as a distance indicator for clusters (Bower et al. 1992).

In addition to the three above components, the **intracluster light (ICL)** has also to be mentioned. This is diffuse optical light emitted by stars that are gravitationally bound not to any galaxy of the cluster but to the cluster itself. Likely, the stars associated with the ICL were ejected from galaxies experiencing dynamical interactions. Albeit the ICL is very faint ($\sim 1\%$ of the dark sky brightness) it accounts for $\sim 25\%$ of the luminosity of a cluster in the optical band. An example of the ICL detected in the Virgo Cluster is shown in Fig. 2.6.

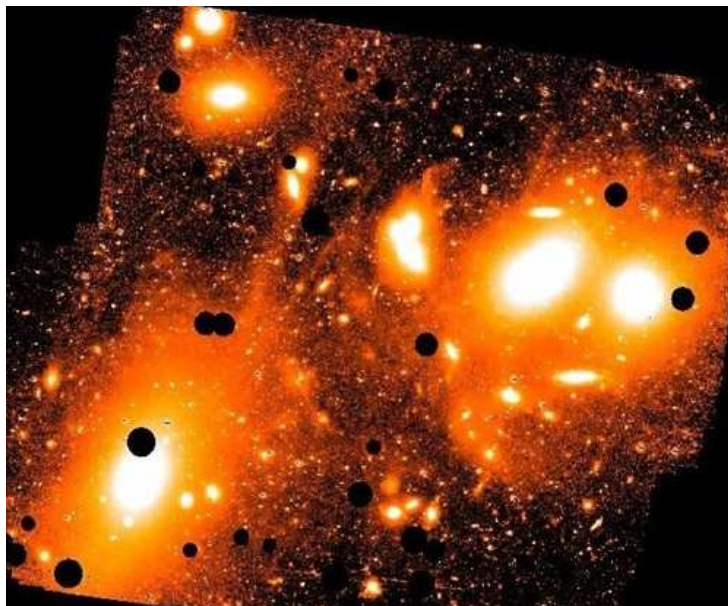


Figure 2.6: A deep ($\mu_v \sim 28.5 \text{ mag arcsec}^{-2}$) optical image of the Virgo Cluster revealing the intricate web of the intracluster light that fills the space around galaxies in the cluster. Image from Mihos et al. (2005).

2.4 How to detect galaxy clusters

Surveys are characterized in terms of flux sensitivity, sky coverage and redshift limit, quantities that vary according to the final aim of the survey itself and the instrumentation used. In addition, for each survey *purity* (i.e., the amount of contamination due to spurious selected objects) and *completeness* (the percentage of missed objects that, actually, should have been detected) should be known in detail. Several methods for detecting galaxy clusters exist, each one focussing on a specific cluster component (see Sec. 2.3). Hereafter, I describe these methods in brief and highlight their strengths and weaknesses.

2.4.1 Optical selection

The first identification of galaxy clusters dates back to 1784, when Charles Messier reported the discovery of the Virgo Cluster as an **optical overdensity of galaxies** in the sky. For almost two centuries since then, galaxy clusters have been identified in the same way, finally using photographic plates instead of naked eyes. Albeit this

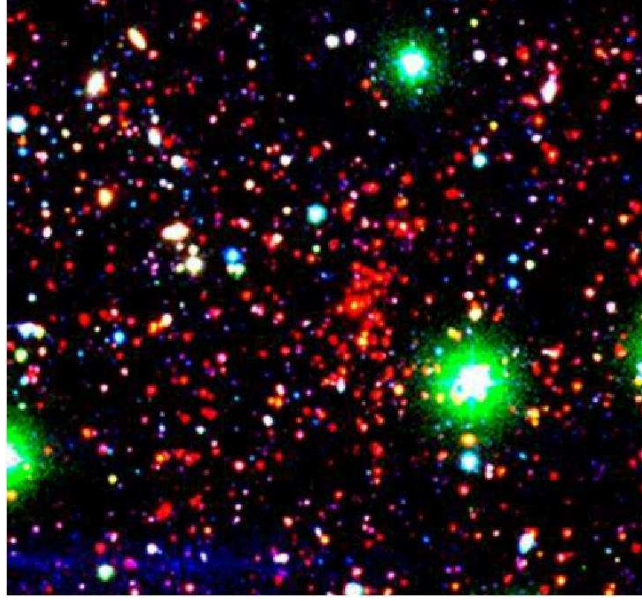


Figure 2.7: Color composite image in r' , z' and $3.6\mu m$ bands of SpARCS J003550-431224 at $z = 1.34$. The cluster clearly emerges as a red overdensity, well contrasted w.r.t. the surrounding galaxies. The field of view (FOV) is $5'$ (2.5 Mpc at the cluster redshift). Image from Wilson et al. (2009).

strategy yielded about two thousand clusters in the second half of the 20th century (Abell 1958; Zwicky et al. 1968), it is highly biased toward those systems whose galaxy distribution is highly contrasted with respect to the surrounding environment. As a consequence, the optical overdensity selection tends to preferentially identify the most *massive* clusters whose galaxy distribution is very peaked in the center, and the *nearby* clusters, whose galaxies are bright and the contamination from foreground galaxies is limited.

2.4.2 Color overdensity selection

A modification of the optical overdensity selection technique is based on the identification of the **red galaxy population** overdensity that, as mentioned in Sec. 2.3, commonly exhibits a very small scatter in color. This property translates into a tight red-sequence in a color-magnitude diagram, a feature widely found in galaxy clusters. This strategy makes use of photometry in at least *two* filters (in optical or infrared band) in order to create a *color* image of the observed galaxies and, hence, allows

the identification of the cluster as an overdensity of *red* galaxies, well contrasted from the fore/background (Fig. 2.7). Many surveys have adopted this strategy e.g., the Munich Near-Infrared Cluster Survey (*MUNICS*, Drory et al. 2001); the Red Sequence Cluster Survey (*RSCS*, Gladders & Yee 2005); the Spitzer Adaptation of the Red-sequence Cluster Survey (*SpARCS*, Wilson et al. 2006) and their outcomes have significantly increased the number of known clusters, also at *high redshift*. The weakness of this approach, however, is that it selects *only* those clusters heavily populated by red galaxies. This restriction may be safe in the local universe, where most of the galaxies in clusters are well known to be “red and dead”, but it may not hold anymore at high redshifts, where galaxies start to exhibit a noticeable star formation activity also in the densest, central regions of clusters (Tran et al. 2010; Fassbender et al. 2011c) resulting in the vanishing of the red-sequence feature. In addition, a non negligible population of clusters with a large fraction of *blue* galaxies in their cores seems to exist at intermediate redshift ($z \sim 0.3$), according to the so-called Butcher-Oemler effect (Butcher & Oemler 1978). As a consequence, it is extremely difficult to quantify the completeness of these surveys in order to enable their use for cosmological purposes (see Sec. 2.5.1).

2.4.3 SZ selection

As mentioned in Sec. 2.3, the hot electrons of the ICM can locally distort the spectrum of the CMB by scattering its photons via inverse Compton, thus resulting in a local decrement (increment) of the CMB intensity at millimeter (sub-millimeter) wavelengths. This effect is called the **Sunyaev–Zel’dovich (SZ) effect** as it was predicted theoretically for the first time in the 70s by Sunyaev & Zel’dovich (1972). The basic consequence of this theory is that galaxy clusters can indeed leave an imprint on the spectrum of the cosmic microwave background observed at millimeter wavelengths (Fig. 2.8). The magnitude of the SZ effect is defined by the Compton y -parameter which depends only on the physical properties of a cluster. It is a measure of the electron pressure integrated along the line of sight (l.o.s.) x , as

$$y = \int \frac{k_B T(x)}{m_e c^2} n_e(x) \sigma_T dx , \quad (2.19)$$

where k_B is the Boltzmann constant, T is the X-ray temperature of the hot gas, m_e is the electron mass and σ_T is the Thomson cross-section. For practical purposes, the SZ signal is usually quantified with the *integrated* Compton parameter $Y \propto \int y dA$, which provides a measure of the SZ signal over the cluster’s projected area dA . The main strength of the SZ surveys is that, unlike optical and X-ray observations, the

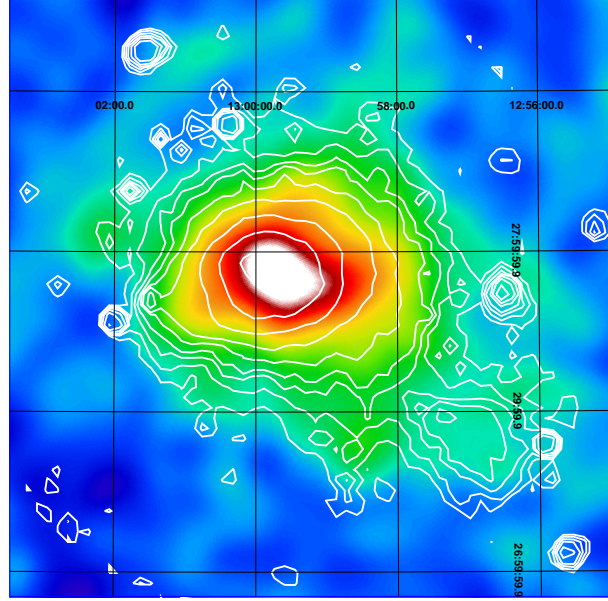


Figure 2.8: The SZ effect of the Coma Cluster as detected by *Planck* ($3^\circ \times 3^\circ$ patch), with the X-ray *ROSAT* contours overlaid in white. Image from Planck Collaboration et al. (2011b).

intensity of the SZ effect is *independent of distance*. This makes the SZ surveys potentially able of detecting the most distant clusters of the universe since they are only limited in mass rather than in flux (Fig. 2.9). Nevertheless, because of the poor spatial resolution ($\Theta \sim 60''$) that can be achieved in the millimeter band by the currently most widely used instruments for SZ cluster surveys, one weakness of such a selection technique is that foreground (background) SZ sources located just in front of (behind) a cluster are interpreted as a single source, thus altering the estimated parameters of the main target. In addition, the presence of radio point sources along the line of sight increases the local CMB flux, thus possibly cancelling out some of the SZ decrement due to the ICM. The two aforementioned issues can, however, be partially overcome by means of radio telescopes with a much higher spatial resolution. Currently, the only instrument able to provide observations in the millimeter band with a resolution of few arcseconds is the Multiplexed SQUID TES Array at Ninety Gigahertz (MUSTANG, Dicker et al. 2008) mounted at the Green Bank Telescope. In addition, enormous improvements in the quality of the mm-band observations are expected to come in the near future thanks to the Atacama Large Millimeter Array (ALMA, e.g. Testi 2010), which will be able to reach $\Theta \sim 0.01''$ at

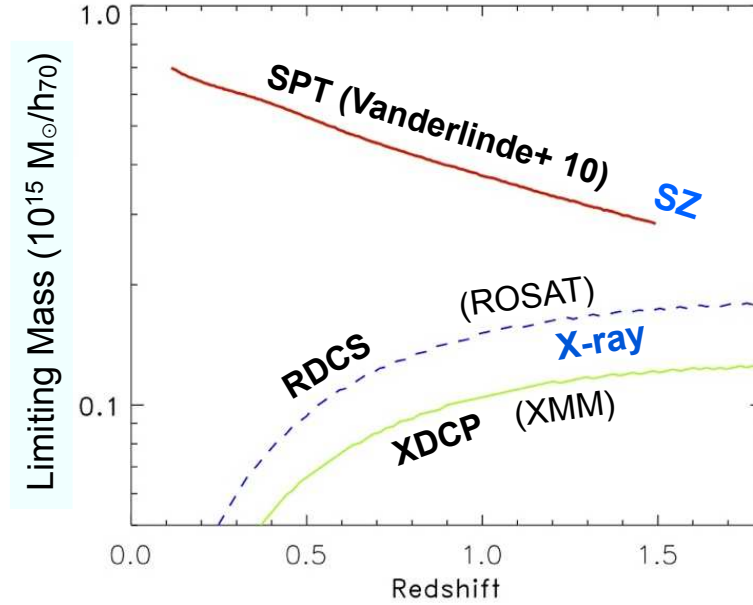


Figure 2.9: Dependence of the limiting mass M_{lim} on redshift for X-ray (green and dashed curves) and SZ (red line) surveys. The figure shows that M_{lim} is proportional to the square of the luminosity distance ($d_L(z)$) for the X-ray surveys. Such a dependence is instead absent for SZ observations, where actually *lower* masses tend to be observed toward higher redshifts. The SZ performances are estimated by using the sample of 21 clusters selected with the South Polar Telescope (SPT) and published in Vanderlinde et al. (2010). Plot courtesy of B. Sartoris.

millimeter wavelengths.

The first large catalogues of clusters selected via the SZ effect are currently under construction by using instruments like the Atacama Cosmology Telescope (*ACT*, Marriage et al. 2011), the South Polar Telescope (*SPT*, Carlstrom et al. 2011) and the Planck satellite (Planck Collaboration et al. 2011a).

2.4.4 X-ray selection

Dark matter haloes associated with clusters keep the baryonic gas confined within them and, because of the depth of their potential wells, heats the gas until it reaches temperatures of $\sim 10^6 - 10^8$ K. The baryonic gas (with typical densities of $n_e \sim 10^{-3} \text{ cm}^{-3}$) is then highly ionized and vigorously emits in the X-ray domain via **thermal bremsstrahlung**, whose emissivity is given by Eq. 2.17. As a consequence, galaxy

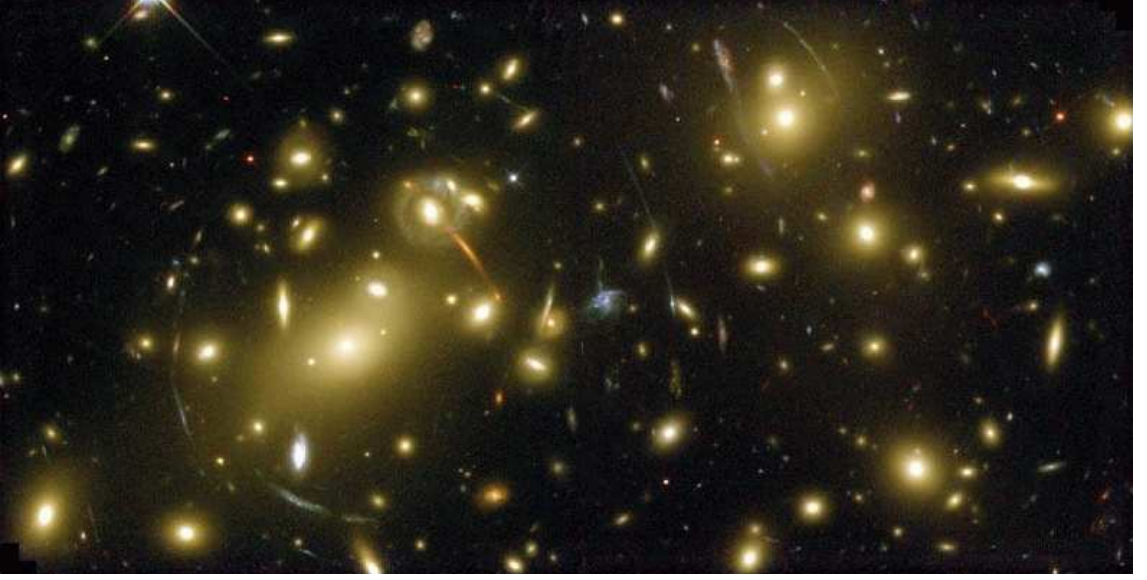


Figure 2.10: A color composite image of the massive cluster Abell 2218 at $z = 0.18$, taken with HST. Many strong lensing features, such as arcs and multiple images, can be seen. The gravitational lensing always gives rise to arcs which are mainly tangential to the center of the mass distribution. Credits: NASA.

clusters are easily identified in X-ray, appearing as extended X-ray sources, with a high surface brightness in the central regions and a total luminosity of $L_X \sim 10^{44} - 10^{45} \text{ erg s}^{-1}$ (see the contours in Fig. 2.8). Every survey aimed at constructing a sample of X-ray selected clusters is actually limited in *surface brightness*, i.e. objects too faint or too diffuse are missed (see Fig. 3.3). However, once the detailed technical information of the instrument used for observations are provided, together with a model able to statistically describe the physical properties of galaxy clusters, all the characteristics of the survey can be determined *exactly* by means of extensive numerical simulations. This is the aspect that makes X-ray surveys particularly useful for cosmological purposes. Finally, as the X-ray gas is a collisional fluid, it reaches the thermodynamic equilibrium in relatively short time scales w.r.t. galaxies, for example (White et al. 2010). This guarantees that also high redshift clusters exhibit a strong emission in the X-ray band.

2.4.5 Strong and weak Lensing selection

According to the theory of General Relativity theory, massive bodies distort the surrounding space-time, hence bending the paths of light rays passing in their proximity.

This effect is observable for galaxy clusters and, for the most massive ones, it can produce strong features, like arcs and multiple images of the background galaxies behind the lensing cluster. This phenomenon is called “strong lensing” (Fig. 2.10). Gravitational lensing also induces statistically significant deformations of the shapes of background galaxies, producing a signal called “shear lensing” which can be used to accurately define the mass profile of a lensing cluster out to large radii. Although this method is usually used to assess *a posteriori* the *true* total mass of a cluster already confirmed via other methods, Wittman et al. (2006) reported for the first time a sample of a few clusters completely selected via shear lensing and with redshifts up to $z \sim 0.7$. Such a strategy produces a survey limited *purely* in mass but possibly affected by projection effects due to mass distributions in the fore- and/or background, for which an identification, and hence a correction, is currently hard to obtain.

2.5 The importance of galaxy clusters

2.5.1 Galaxy clusters as cosmological probes

Galaxy clusters are the most recently formed gravitationally-relaxed objects. Due to the fact that density peaks have higher amplitudes at smaller scales, the first structures which deviated from the Hubble flow and started to collapse and virialize, under their own self-gravity, had sub-galactic sizes. These small objects then merged and created galaxies, which eventually were collected inside clusters. Hence, the formation and evolution of galaxy clusters directly trace structure growth in the universe. For this reason galaxy clusters yield valuable information about the underlying cosmological model and can be used to conduct a number of critical tests both for the underlying cosmological parameters characterizing our universe and for the physics of structure formation in the primordial universe. Specifically, the most important cosmological studies involving galaxy clusters can be summarized as follows:

1. the accurate determination of the cluster *mass function* (Eq. 2.14) observed in the local universe and its evolution toward earlier cosmic epochs (see Fig. 2.4) can provide important constraints on the **matter and dark energy content** of the universe. This effect is clearly shown in Fig. 2.11 via an N-body simulation result, which demonstrates how assessing the abundance of clusters beyond $z = 0.6$ can easily help to discriminate between models with and without a cosmological constant. The revelation of massive clusters at $z > 0.6$ at the end of the 90s (Donahue et al. 1998; Bahcall & Fan 1998) indeed started

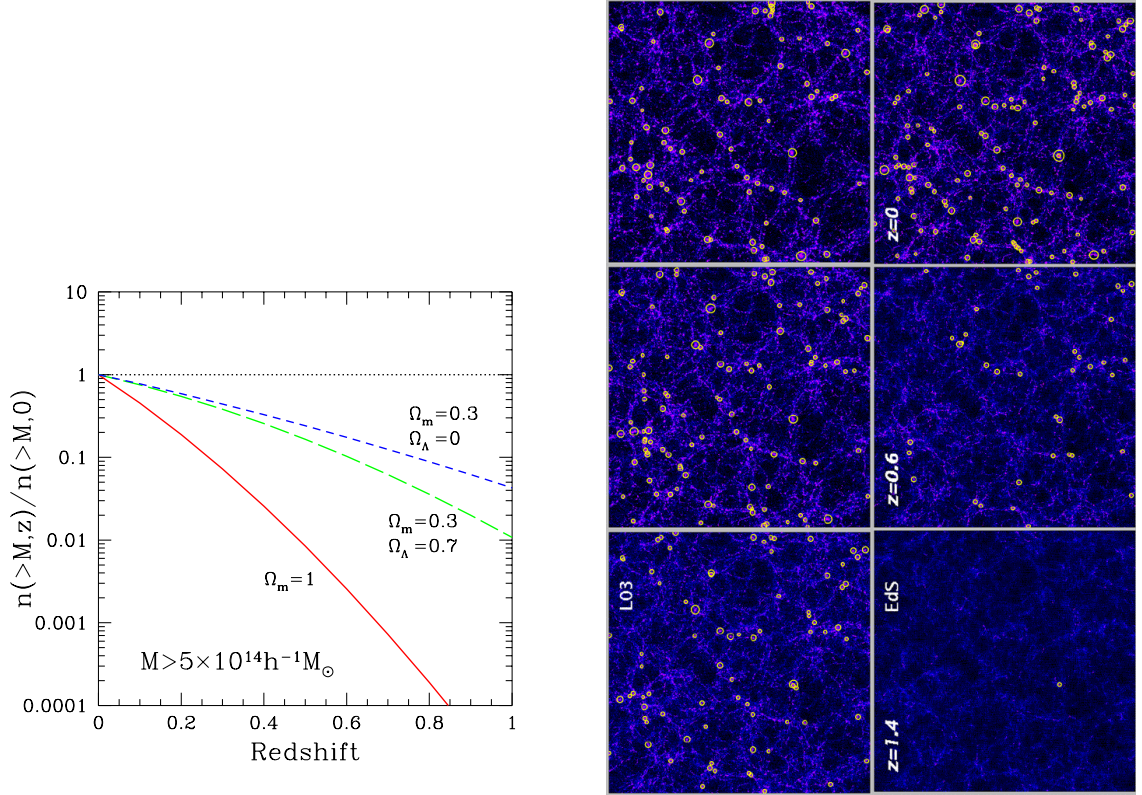


Figure 2.11: *Left*: Evolution of the cluster number density with redshift $n(> M, z)$ (normalized to the value at $z = 0$) for different cosmological models. *Right*: Visualization of the results reported in the left panel. The simulation shows the evolution of the cluster number density from $z = 1.4$ (bottom side) to $z = 0$ (top side) for a flat, low density universe with $\Omega_m = 0.3, \Omega_\Lambda = 0.7$ (left column) and for a flat, matter dominated universe with $\Omega_m = 1, \Omega_\Lambda = 0$ (right column). Yellow circles mark the position of clusters. Each snapshot is $250 h^{-1}\text{Mpc}$ across and $75 h^{-1}\text{Mpc}$ thick. Plots from Borgani (2006).

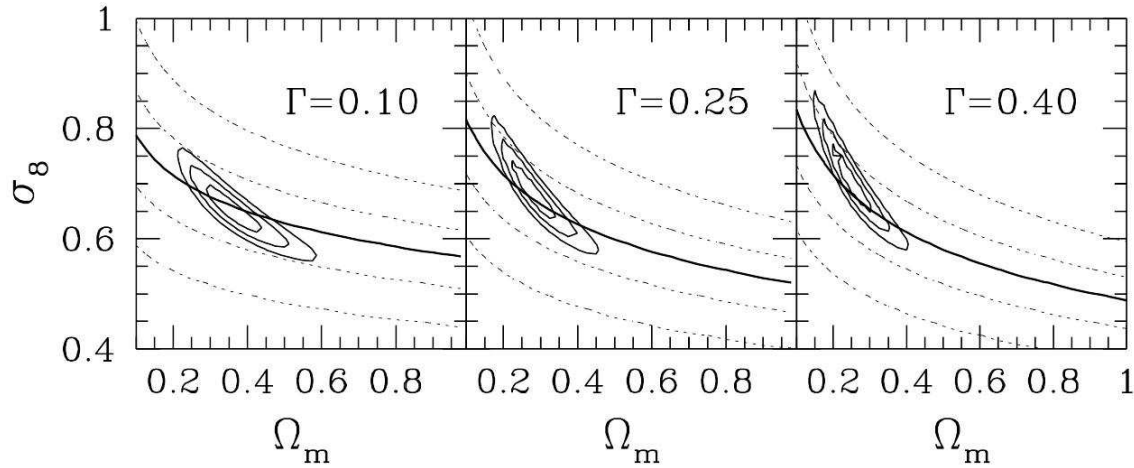


Figure 2.12: Confidence regions of σ_8 and Ω_m constrained by means of the RDCS-1 sample of 4 clusters at $z > 0.9$. The three panels refer to different values of the power-spectrum shape parameter $\Gamma = h\Omega_m$. The dotted curves indicate the expected $\Omega_m - \sigma_8$ relations for different numbers of $z > 0.9$ clusters ($N = 0.1, 1, 10, 30$ from bottom to top); the solid line refers to the actual value of 4. Plot from Borgani et al. (2000).

to challenge the standard model (at that time with $\Omega_\Lambda = 0$ and $\Omega_m = 1$) and hence anticipated the ultimate discovery of a dark energy component currently accelerating the expansion of the universe, achieved via the Type Ia supernova surveys (Reiss et al. 1998; Perlmutter et al. 1999).

2. the characterization, from simple cluster counts, of the spatial distribution of the clusters at redshift zero and its evolution up to $z > 1$ contains a wealth of information on the statistical properties of the large scale structure of the underlying dark matter. This aspect is parametrized by using the *power spectrum*, $P(k)$, already defined in Eq. 2.9. The shape of $P(k)$ can be defined analytically, and is actually also constrained by the cluster mass function at $z = 0$, but its normalization can only be assessed empirically. This is obtained by introducing the parameter σ_8 , generically defined as the mass variance (Eq. 2.15) smoothed within a sphere of radius $8 h^{-1}\text{Mpc}$. Specifically, σ_8 and $P(k)$ are linked to one other according to the relation

$$\sigma_8^2 = \left\langle |\delta M/M|_{8h^{-1}\text{Mpc}}^2 \right\rangle_{z=0} = 4\pi \int \frac{dk k^2}{(2\pi)^3} P_{z=0}(k) W_{8h^{-1}\text{Mpc}}^2(k) \quad (2.20)$$

i.e., σ_8 is the *rms* of the dark matter density contrast linearly evolved to the present epoch ($\delta(\vec{x}, t_0)$) and smoothed with a filter of $8 h^{-1}\text{Mpc}$. Currently, the most accurate value for this parameter is provided by the WMAP7 mission (Komatsu et al. 2011): $\sigma_8 = 0.816 \pm 0.024$. There exists a strong degeneracy between Ω_m and σ_8 , as low matter density values can be compensated by higher values of σ_8 , and vice versa. One way of breaking such a degeneracy is to measure the evolution of the cluster mass function, which is particularly sensitive to Ω_m . An example of such an approach is shown in Fig. 2.12, where a sample of 4 distant clusters extracted from the ROSAT Distant Cluster Survey (RDCS, Rosati et al. 1998) has been used.

3. Already at the beginning of the 90s, the comparison of the baryon content in the local clusters (Fabian et al. 1991; Briel et al. 1992) with the primordial nucleosynthesis expectations, helped to rule out models of the universe with a critical matter density (White et al. 1993).
4. X-ray and SZ emissions coming from galaxy clusters are complementary as the former provides the integral along the line of sight of ρ_{gas}^2 and a gas temperature T_{gas} . By dividing the product of $T_{gas} \times \int \rho_{gas}^2 d(l.o.s.)$ by y -Compton (Eq. 2.19) one can obtain the mass *density profile* of the cluster ICM matter that can then be used to infer the physical thickness of the system. Under the assumption of spherical symmetry, the obtained physical size can be compared with the apparent angular size in order to get a constraint on cosmological parameters by means of the *angular distance*, $d_A(z)$. This is the method that was used for the first time by Birkinshaw et al. (1991).

As discussed for the aforementioned methods, a key ingredient for enabling the use of galaxy clusters as cosmological probes is the accurate measurement of their **masses**. However, cluster masses are not physical quantities that can be *directly* determined from observations, they have to be inferred from observables which correlate with mass. This aspect always motivated the need of understanding possible systematic effects associated with the use of different observables as mass proxies (e.g., Henry et al. 2009), some of which are discussed in the next session.

2.5.2 Mass proxies for galaxy clusters

Under the assumption that the intracluster gas is in *hydrostatic equilibrium*, the radial mass profile of clusters can be written as

$$M_{tot}(< r) = -\frac{k_B T_X(r) r}{G \mu m_P} \left(\frac{d \ln \rho_{gas}}{d \ln r} + \frac{d \ln T_X}{d \ln r} \right) \quad (2.21)$$

where μ is the mean molecular weight and m_P is the proton mass. An estimate can thus be obtained by measuring the radial profile of density and X-ray temperature of the ICM in annular regions, a task feasible only for relatively nearby clusters or with particularly long exposure times.

We note here, that as clusters do not have clear boundaries, their total mass is commonly assumed to be approximately the virial mass, M_{200} , i.e., the mass enclosed by a sphere of a radius within which the mean density at redshift z_{cl} is $200 \times \rho_{crit}(z_{cl})$ (see Sec. 2.1). In this way, also a corresponding cluster radius R_{200} is defined.

As mentioned in Sec. 2.3, galaxies in clusters trace the DM potential well and the dispersion of their velocity distribution can provide an estimate of the total mass via Eq. 2.18. However, unlike the gas particles making the ICM, galaxies in clusters are *non-collisional* systems which, hence, relax on a longer timescale. As a consequence, the masses based on kinematical measurements may significantly differ from the M_{200} , especially if the cluster experienced a merging event in the recent past.

As galaxies and the ICM particles share the same potential well, the assumption of a *virial* equilibrium between them would produce $T_X \propto \sigma_v^2$. The X-ray temperature is a good proxy for the total cluster mass, with a dependence, empirically confirmed (Arnaud et al. 2005), as $M_X \propto T_X^{3/2}$. Also the X-ray bolometric luminosity well correlates with the total mass, but with a slope *steeper* than expected from pure gravitational effects ($L_X \propto M_{200}^{1.8}$ (Pratt et al. 2009) instead of $L_X \propto M_{200}^{4/3}$). The disagreement between the expected/observed exponents in the above relation may indicate the presence of some non-gravitational effects altering the physical properties of the hot gas (e.g., AGN and SNe feedback).

One of the tightest ($\leq 15\%$ of scatter (Arnaud et al. 2007; Mantz et al. 2010)) correlations associated with the cluster's total mass is obtained for the quantity $Y_X = T_X \cdot M_{g,500}$, i.e., the product of the X-ray temperature and gas mass enclosed within R_{500} , the radius corresponding to a density contrast of $\delta = 500$. Y_X is the X-ray analog of the integrated SZ Comptonisation parameter Y_{SZ} defined in Sec. 2.4.3 and was proposed by Kravtsov et al. (2006).

Finally, the masses measured with lensing (strong and weak) techniques are currently believed to be the most reliable and, hence, considered as an element of comparison for other mass estimates.

2.5.3 Clusters as astrophysical laboratories

While current numerical simulations are able to accurately describe the purely gravitational interactions among dark matter components, such an accuracy cannot be reached for baryonic matter, as its physics is heavily non linear and comprises of

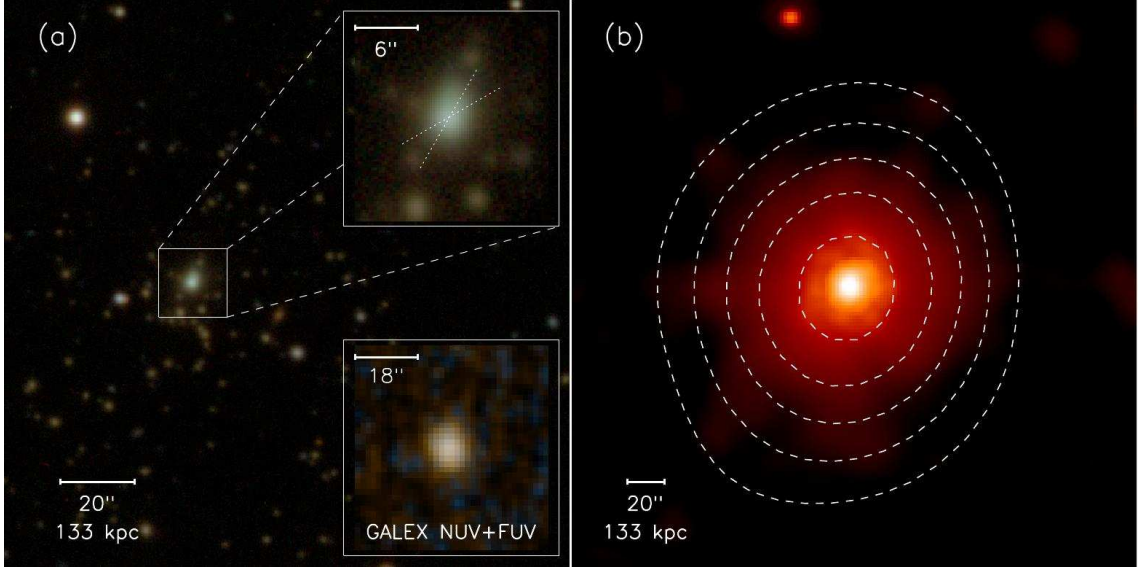


Figure 2.13: *Left:* Optical r , i , z color composite image of the inner region of SPT-CLJ2344-4243. The central galaxy is the most massive and luminous galaxy in the cluster, but it is considerably *bluer* than the rest of the member galaxies, suggesting significantly younger stellar populations. This is evident in the zoomed-in lower right inset, showing an ultraviolet color-composite image with the same size of the larger panel. In the UV-color inset the central galaxy is actually the only visible one and appears as a bright UV source. *Right:* False-color image of the X-ray emission of the cluster with an overlay of its SZ signal as white-dashed contours. This image clearly shows the luminous, centrally-concentrated core, as well as the relatively smooth, relaxed morphology of the intracluster medium. Image from McDonald et al. (2012).

hydrodynamical effects.

The physics of the ICM and of galaxies in clusters are deeply connected. Many studies have shown that baryonic condensation, and hence galaxy formation, in clusters is highly inefficient (and actually this is the reason why galaxy clusters shine in X-ray). Giodini et al. (2009) recently found that the stellar mass is only $\sim 12\%$ of the total baryon fraction, with the percentage decreasing with the total halo mass. Such an inefficiency may be explained by assuming non-gravitational mechanisms acting in the direction of *re-heating* the cooling gas in a *self-regulating* way, i.e. by injecting exactly the amount of energy needed to keep the gas in thermodynamical equilibrium. Among the different processes proposed in this sense, the most widely

accepted one assumes the presence of a radio AGN in the center of the brightest cluster galaxy (BCG). This engine is supposed to act in a way to prevent the formation of a *cooling flow* that should originate from the bremsstrahlung cooling mechanism itself: as the central region of the ICM distribution is also the most dense, it should also cool faster (see Eq. 2.17). This would further increase its density resulting in a runaway process, which would finally result in vigorous star formation activity ($\sim 10^2 - 10^3 M_\odot \text{ yr}^{-1}$) systematically observable in the cores of most galaxy clusters. However, this effect has not been observed, which suggests that a balancing mechanism has indeed to exist and must act in a very short time-scale.

Nevertheless, McDonald et al. (2012) recently reported the observation of a SZ-selected cluster (SPT-CLJ2344-4243 at redshift $z = 0.596$) which seems indeed to be experiencing a cooling-flow event, with a luminous, massive central galaxy exhibiting strong star formation activity ($\sim 740 \pm 160 M_\odot \text{ yr}^{-1}$). If confirmed, this finding is one of the most striking evidences of the existing interconnection between the ICM and (central) galaxies in clusters.

In fact, galaxies in clusters have long since been found to be affected by the dense environment through which they continuously move. Specifically, effects like *ram pressure stripping*, by the hot gas, can remove a significant amount of cold, atomic (HI) gas from disk galaxies (e.g., Gunn & Gott 1972; Kenney et al. 2004), possibly accelerating their evolution toward the final passive state. In dense environments galaxies can also interact among each other via *merging*, *collisions* and *tidal effects* (see Boselli & Gavazzi (2006) for a review). All these processes eventually yield a galaxy that resembles an elliptical galaxy in shape or color and with a similarly extremely poor gas reservoir.

The above mentioned mechanisms are thought to actively contribute to the creation of the ubiquitous red galaxy population found in clusters up to $z = 1.4$ (Mullis et al. 2005). In addition, the extremely low scatter observed in color (typically $\lesssim 0.05$ mag) should also indicate that the formation of passive galaxies must have happened at high redshifts ($z > 2$) and within timescales $\leq 1 \text{ Gyr}$. In this way galaxies had enough time to evolve passively and to achieve a similar red color at $z = 0$ (Bower et al. 1992). Similar findings about the importance of the environment in regulating the evolutionary timescales of early type galaxies (ETGs) were also reported by Thomas et al. (2005). By studying a sample of 124 ETGs in low- and high-density environments, the authors showed that ETGs in clusters appear to have experienced the bulk of their star formation between $z \sim 5$ and 2 and that this activity seems to have been delayed by $\sim 2 \text{ Gyr}$ in the lowest density environments. However, in addition to environmental effects the authors also reported evidence of the importance of the galaxy *mass* in this context. Their findings suggested, in fact, that the

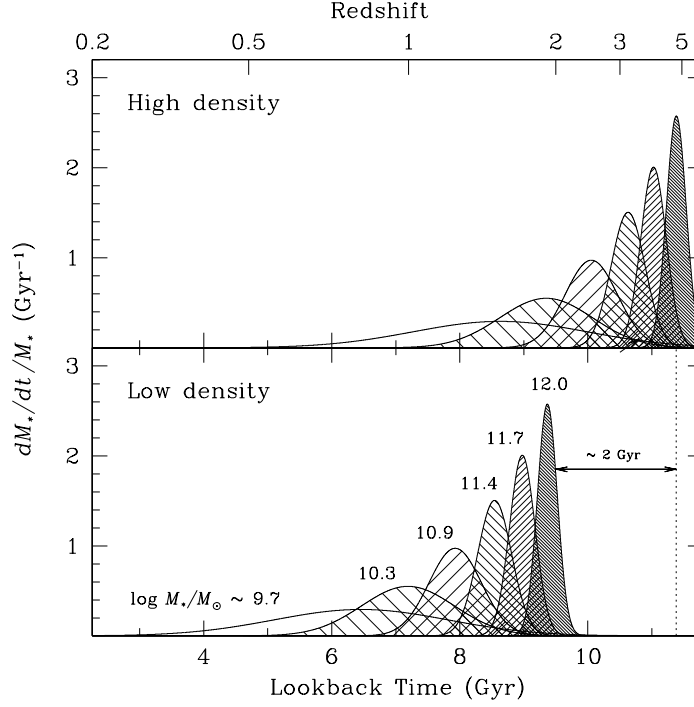


Figure 2.14: Qualitative summary of the evolutionary scenario proposed by Thomas et al. (2005) for the average star formation history of early-type galaxies of different masses and residing in different environments. The numbers reported on the top of each curve in the bottom panel refers to the logarithmic values of the galaxy masses. Plot from Thomas et al. (2005).

most massive ($M \gtrsim 10^{11} M_\odot$) ETGs have completed their star formation activity in shorter timescales (~ 1 Gyr) w.r.t. the less massive ($M \lesssim 10^{10} M_\odot$) ones, for which the star formation lasted more than 2 Gyr. The results of Thomas et al. (2005) are qualitatively summarized in Fig. 2.14.

Chapter 3

The XMM-*Newton* Distant Cluster Project (XDCCP)

The first systematic search and study of galaxy clusters based on their X-ray luminous ICM started in the 1980s with the first X-ray satellite HEAO-1 (Piccinotti et al. 1982). 10 years later, the first X-ray imaging telescopes, EINSTEIN (Gioia et al. 1990) and ROSAT (Truemper 1992), started to carry out the first deep and all sky (RASS) X-ray surveys, respectively. The outcome of these two surveys were complementary as the former provided indications of the evolution of cluster abundance with redshift (up to redshift $z = 0.58$, Henry et al. 1992), whereas the latter enabled the construction of a sizable sample (~ 500) of clusters at redshift $0.02 \lesssim z \lesssim 0.5$, usable for cosmological studies (Böhringer et al. 1993). With ROSAT, only 10 clusters were observed at $z > 0.8$ in the ROSAT Deep Cluster Survey (RDCS Rosati et al. 1998; Rosati 2001) but they were enough to demonstrate the existence of well formed systems already at $z \sim 1.3$. In addition, the inferred lack of a significant evolution of the luminosity function at $z > 1$ was totally in contrast with the theoretical expectations at that time for an Einstein De Sitter (EdS) universe with $\Omega_m = 1$ (Borgani et al. 2000), implying a lower matter density of the universe.

Two of the RDCS clusters were also particularly interesting to address questions related to how clusters and their galaxy population are interconnected: RX J0848+4453 at $z = 1.26$ (Stanford et al. 1997) and RX J0849+4452 at $z = 1.27$ (Rosati et al. 1999). As discussed in Rosati (2001), these two close (in projected and redshift space) systems show a completely different X-ray morphology (the former symmetric and centrally peaked, the latter patchy and irregular) indicative of two different dynamical states (relaxed and merging, respectively). In addition, in both cases the red galaxy population is found to closely follow the distribution of

the corresponding ICM. Despite these remarkably different dynamical aspects, the two populations of red galaxies seem to be *indistinguishable*, as they show the same color within 0.05 mag. This was one of the first observations revealing that galaxy clusters assembled their mass at relatively late epochs ($1.5 \lesssim z \lesssim 3$) w.r.t. the typical redshifts ($z > 3$) at which their hosted early type galaxies completed the formation of their stellar mass .

The XMM-*Newton* Distant Cluster Project (XDCP) started in 2003 and was conceived as a *third* generation X-ray cluster survey for exploring and characterizing systems lying in the first half of the age of the universe ($z > 0.8$) and *serendipitously* detected in XMM-*Newton* observations. Its final goal is to build a sizable sample (~ 50) of X-ray luminous clusters at high redshift, with a flux limit of $\sim 10^{-14}$ erg s $^{-1}$ cm $^{-2}$ and a survey area of ~ 80 deg 2 (Fig.3.1). In this sense, it is intended to be complementary to *contiguous sky area* X-ray surveys, i.e. surveys based on new X-ray observations, possibly carried out with new, specific instruments (e.g. eROSITA). Serendipitous surveys are, in fact, sensitive to lower fluxes, an aspect that makes them optimally suited for studying the high redshift universe.

3.1 Target selection strategy

3.1.1 X-ray analysis

XDCP is a serendipitous X-ray survey, meaning that the first selection of the potentially distant clusters is done on archive XMM-*Newton* fields which targeted different kinds of extragalactic sources. A total of 2960 fields, corresponding to the public data of the first 5 years of the mission, were considered. Out of those, 575 were selected for XDCP after imposing the following constraints:

1. imaging mode available for at least one of the three cameras;
2. minimum nominal exposure time of 10 ksec;
3. fields' positions outside of the galactic plane ($|b| \geq 20^\circ$) and accessible to the Very Large Telescope (VLT) pointings ($\text{DEC} \leq +20^\circ$), a constraint needed to enable the follow-up campaigns.

The sky distribution of the considered 575 XMM-*Newton* fields is shown in Fig.3.2. Finally, after removing those fields flared and/or containing corrupted data, **469** XMM-*Newton* fields were used as input for the survey, corresponding to a total exposure time of 15.2 Msec and a sky coverage of 76.1 deg 2 .

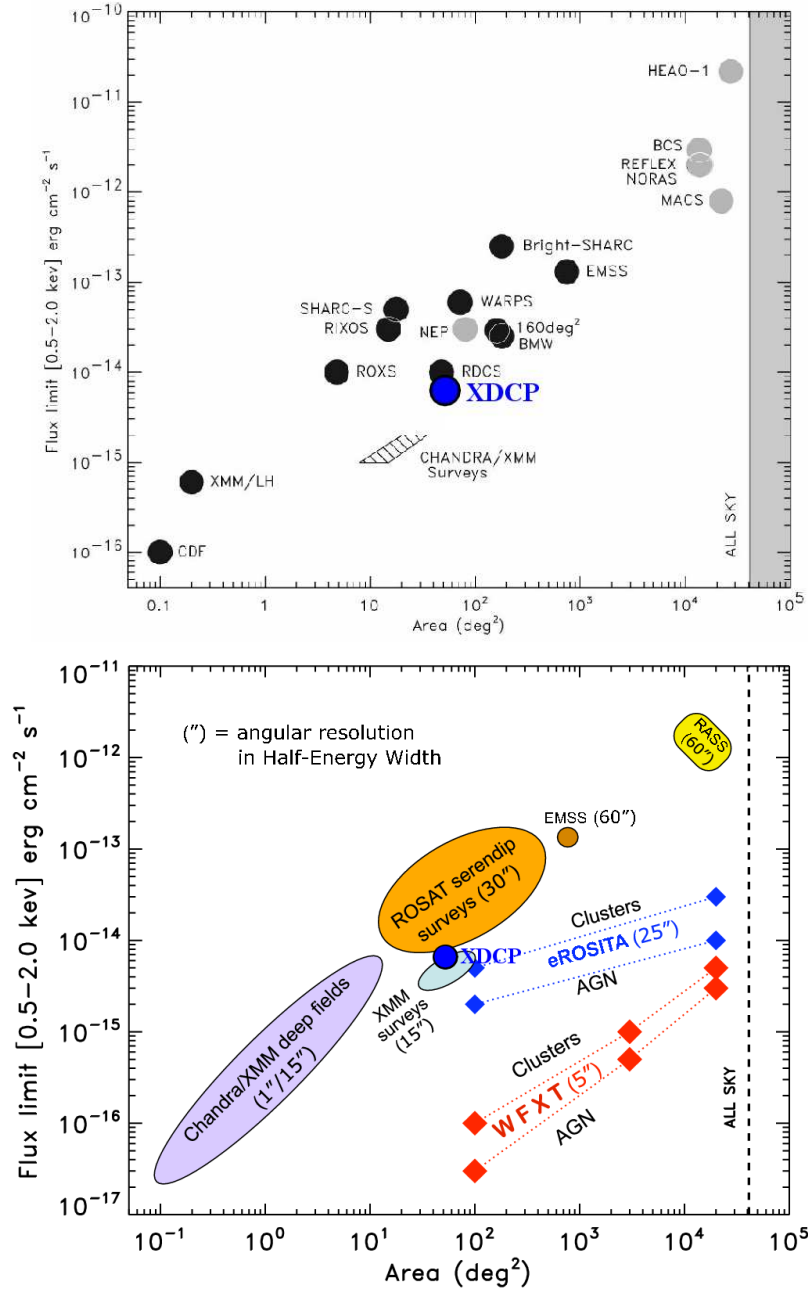


Figure 3.1: Comparison between flux limit and area coverage of XDCP with a set of past (*top*) and new/planned X-ray surveys (*bottom*). Plots adapted from Fassbender (2007) (*top*) and Rosati et al. (2011) (*bottom*).

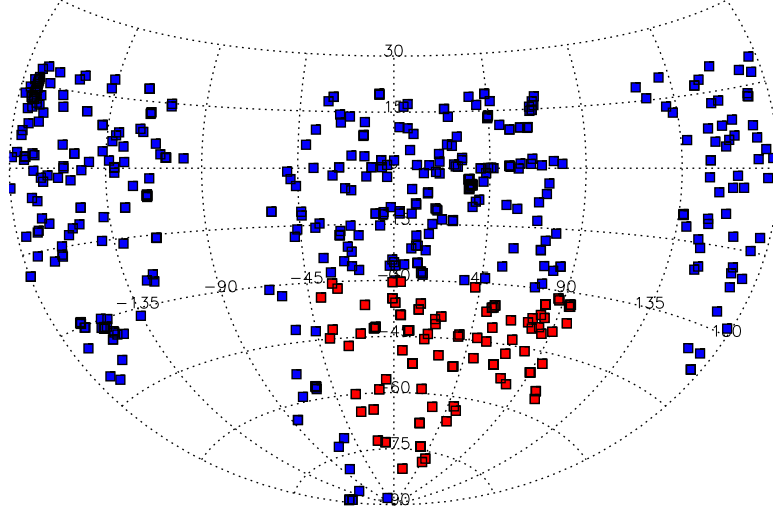


Figure 3.2: Position of the 575 selected XMM-*Newton* archive fields, 469 of which were effectively used as input for the survey. The red ones are fields overlapping with the South Pole Telescope survey. From Fassbender et al. (2011a).

The above data were then reduced with an automated pipeline, based on the XMM Science Analysis Software (SAS), aimed at identifying also the extended X-ray sources possibly associated with distant galaxy clusters. For each source, a ‘significance’ and ‘extent’ value is associated, the latter computed by fitting the surface brightness profile $S(r)$ with an isothermal King law:

$$S(r) = S(0) \cdot \left[1 + \left(\frac{r}{r_c} \right)^2 \right]^{-\frac{3}{2}} \quad (3.1)$$

A source was identified as extended if the core radius $r_c > 0$ and a fit using Eq. 3.1 with a fixed $\beta = 2/3$ (holding for clusters) returned a significantly improved likelihood. A visual inspection of the candidate extended X-ray sources was finally carried out in order to remove false detections due to artifacts or blends of three or more point sources.

As already mentioned in Sec. 2.4.4, one of the main strengths of X-ray surveys is the possibility of characterizing them *exactly*, in terms of *purity* and *completeness*, by means of numerical simulations. Such an analysis has been carried out for XDCP, as well as by implementing a pipeline which mimicked all the identification steps described above on a set of simulated fields similar to those 469 ones selected as input.

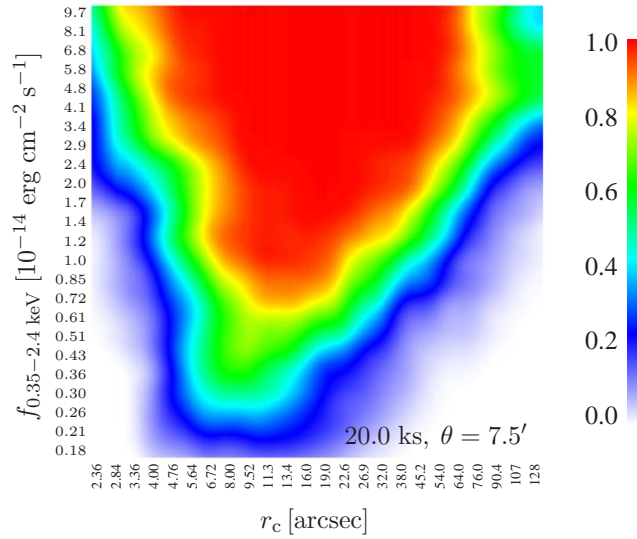


Figure 3.3: Probability (in color scale) of detecting an X-ray cluster in XDCP for different values of X-ray flux and core radius r_c , here presented for an off-axis angle $\Theta = 7.5'$ and a net exposure time of 20 ksec. Plot from Mühlegger (2010).

An example of such a characterization is shown in Fig. 3.3, where the probability of identifying an X-ray cluster located at an off-axis angle¹ $\Theta = 7.5'$ in a field with a net exposure time of 20 ksec is given as a function of its X-ray flux in the 0.35 – 2.4 keV band and its core radius r_c . For a given off-axis angle and exposure time, the “shark tooth” shape of the detection probability function is due to three reasons:

- the *sensitivity* limit: objects with a too low flux are not detected, independently of their core radius;
- the *resolution* limit: objects too compact (small r_c) are missed because all sources with angular size well below the angular resolution of XMM-Newton ($\sim 5\text{--}10''$) are flagged as point sources and, hence, discarded by the selection procedure described above.
- the *background* limit: sources that are extended (high r_c), but not bright enough, exhibit a low contrast w.r.t. the background, and so are confused with it.

¹The off-axis angle is the angular distance between the position of an observed object and the optical axis of the telescope.

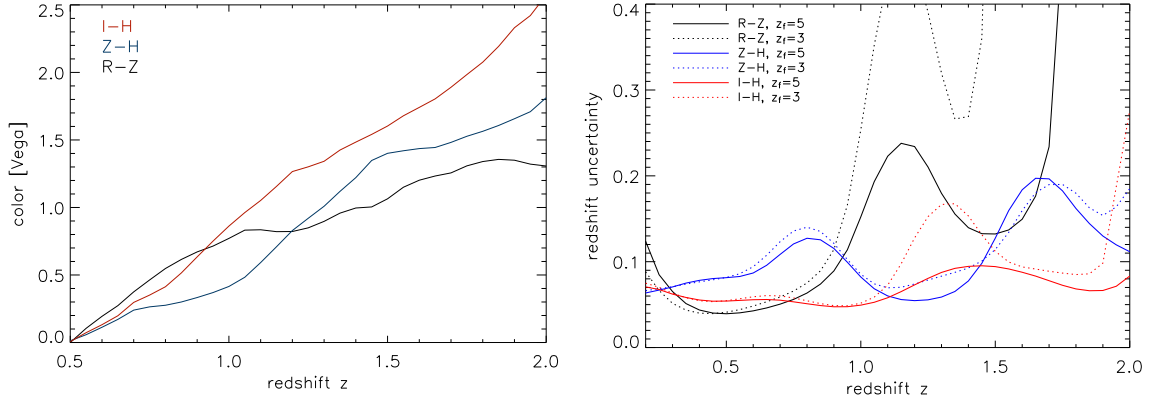


Figure 3.4: *Left:* Comparison of the redshift evolution of different colors for a simple stellar population with solar metallicity and formation redshift $z_f = 5$. *Right:* Uncertainties on the estimated redshift for the same colors, but assuming two different z_f for each. Although the I–H color yields a better accuracy in redshift estimate w.r.t. z–H, the limitation of having to use different instruments made it not optimum for the XDCP requirements. Plot from Fassbender et al. (2011a).

3.1.2 Photometric follow-up

Once the sample of X-ray extended sources was compiled, it was cross-checked with the online all-sky data base of the Second Digitized Sky Survey² (DSS 2) in order to exclude clusters already known at low redshift. Objects with an X-ray extended emission and not identified in the red and near-infrared bands of DSS2 were flagged as potential galaxy clusters at redshift $z > 0.5$.

In the second phase of the distant galaxy clusters identification, the selected sources were observed in optical and infrared bands in order to enable the *color selection* technique described in Sec.2.4.2. The bands were selected in order to produce, with reasonable short exposure times, a color measure usable as a reliable distance indicator for $z > 0.5$ clusters. Among the several sets of tested filters, the combination that best fulfilled the requirement of time efficiency and accuracy in redshift estimate comprised the z ($\lambda_c = 0.9\mu\text{m}$) and H ($\lambda_c = 1.65\mu\text{m}$) broadband filters of the NIR Omega2000 camera (Bailer-Jones et al. 2000) mounted at the Calar Alto 3.5m telescope. The advantage of the above set is that both bands can be observed with a single NIR instrument, thereby significantly reducing the set up overhead. In

²<http://archive.eso.org/dss>

addition, a further high efficiency in time is guaranteed by the fact that a limiting magnitude of $H_{lim} \sim 21$ mag (Vega) can be reached in less than 1 hour with the NIR cameras mounted on 4m-class telescopes. By considering the passive evolution of a simple stellar population³, it is found that its $z-H$ color exhibits a steep variation in the redshift range $1 \leq z \leq 1.5$, thus resulting in a redshift accuracy of $\sigma_z \leq 0.1$ in that redshift range, and $\sigma_z \leq 0.2$ for $0.8 \leq z \leq 2$. The described behaviour of the $z-H$ color is shown in Fig. 3.4 (*left* and *right* panels), in comparison with two other filter sets, namely $I-H$ and $R-z$.

When the $z-H$ photometric follow-up confirmed the presence of an overdensity of galaxies in correspondence with the extended X-ray emission and the existence of a red locus populated by, at least, three members with similar colors $z-H \geq 2$ mag (Vega), the system was flagged as ‘likely distant’ and selected for the final step, the optical *spectroscopic follow-up*. Currently, all the X-ray selected sources identified in the first phase of the process from the 469 XMM-*Newton* fields have been photometrically followed-up.

3.1.3 Spectroscopic follow-up

The final stage of the distant cluster confirmation process is the spectroscopic follow-up, aimed at confirming both the real nature of gravitationally bound *and* high redshift clusters in the selected systems.

The instrument chosen by XDCP for this purpose is the FOcal Reduced Spectrograph 2 (FORS2) mounted at the Very Large Telescope (VLT) in Chile. The main advantages of this instrument are the high red sensitivity of its sensors and the capability of multi-slit spectroscopic observations. These two aspects allow an efficient spectroscopic confirmation of several cluster members with exposure times of ~ 3 hours for clusters at $z \leq 1.5$. Throughout the survey, the spectrograph was used in the technical configuration adopting the GRISM 300I+11, which allows a wavelength coverage of $5500 \leq \lambda/\text{\AA} \leq 11000$ and a resolution $\lambda/\Delta\lambda \equiv R = 660$. The above wavelength window range is, in fact, particularly suitable for safely assessing the redshift of red galaxies at $0.5 \leq z \leq 1.5$, as it brackets their redshifted continuum break at 4000 \AA (D4000), a prominent spectral feature ubiquitously found in passive galaxies.

The criterion adopted within XDCP for assessing the actual existence of a distant cluster is the existence of a group of at least 3 members with concordant redshifts

³A simple stellar population is an approximation of the galaxy stellar population which consists of stars born at the same time and having the same initial metallicity. Stars of different masses follow different evolutionary tracks.

($\Delta z / (1 + z_{med}) < 0.01$) and within $1'$ of the X-ray centroid.

The spectroscopic reduction of distant cluster members in XDCP is a challenging task as it requires an efficient method of managing a large amount of spectroscopic data and, also, of efficiently extracting the spectra of even faint objects, whose emission is often overshadowed by the sky features (see Sec. 4.3.5). In addition, objects with redshift $z \geq 1.5$ have their D4000 redshifted to observed wavelengths $\lambda_{obs} \geq 10000 \text{ \AA}$, i.e. beyond the sensitivity limits of the currently most used optical spectrographs and in a region where the sky-feature contamination is particularly heavy (see Fig. 4.3, *left*). These technical challenges gave rise to the term “redshift desert” for the range $1.5 \leq z \leq 2.5$ (Cimatti et al. 2004; Steidel et al. 2004) because of the sparse sample of spectroscopically confirmed galaxies known at those cosmic epochs about 8 years ago. However, the above, critical redshift range is also thought to be the epoch when most of the stellar mass formation and mass assembly took place (e.g., Dickinson et al. 2003; Hopkins & Beacom 2006), hence representing a crucial epoch for investigation.

The above reasons motivated my work within XDCP, mainly devoted to developing a new pipeline able to fulfill the above requirements. To this aim, I adapted a version of the *VIMOS Interactive Pipeline and Graphical Interface* (VIPGI, Scodreggio et al. 2005) so that it can also be used with FORS2 data. The name of the new software is *F-VIPGI*, and its performance and properties are extensively discussed in Chapter 4.

3.2 Results

The usage of *F-VIPGI* significantly improved the *efficiency* of the spectroscopic reduction within XDCP, enabling a safe redshift assessment even for the faintest and most distant cluster members. In addition, thanks to the shortening of the spectroscopic data reduction time by a factor of ~ 10 w.r.t. the standard *IRAF* procedures, *F-VIPGI* also increased the final *confirmation rate* of the XDCP clusters. Both these aspects significantly contributed to the accelerated compilation of the XDCP sample of 22 clusters at $0.9 < z < 1.6$, the largest sample of spectroscopically confirmed, X-ray selected distant galaxy clusters to date and publicly released in the XDCP overview paper of Fassbender et al. (2011a). As shown in Fig. 3.5, the XDCP compiled sample comprises clusters in the mass range $M_{200} \simeq 0.7 - 7 \cdot 10^{14} M_{\odot}$ and redshift range $0.9 \leq z \leq 1.6$, with three systems residing in the aforementioned “redshift desert” at $z \geq 1.5$. Only the availability of *F-VIPGI* allowed these three most distant clusters to be spectroscopically confirmed.

The high scientific value of the compiled XDCP sample also concerns the physical

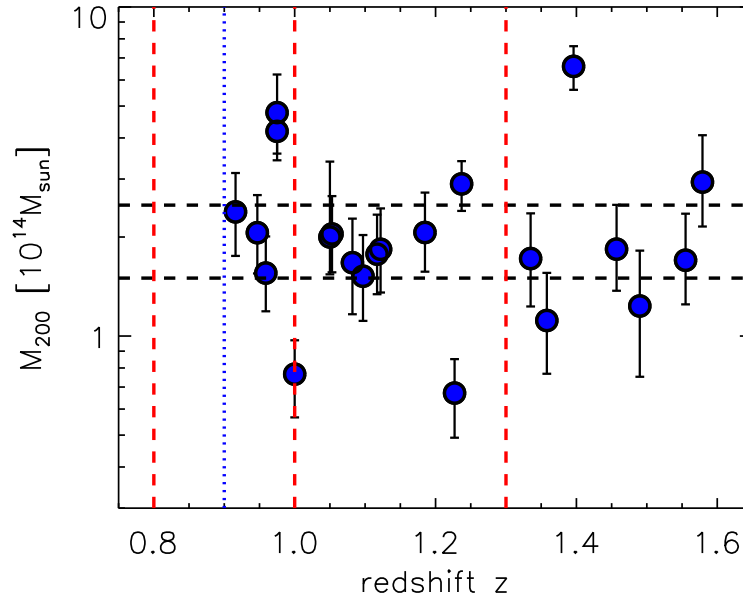


Figure 3.5: Distribution of the compiled sample of 22 XDCP clusters in the M_{200} - redshift plane. The red (black) dashed lines define the three redshift (mass) bins to be used for future studies of cluster properties. The dotted vertical line marks the lower redshift limit $z = 0.9$ of the released sample. It can be appreciated as XDCP has pushed the limit of the spectroscopically confirmed clusters beyond the “redshift desert” limit ($z \geq 1.5$) with three systems at $1.5 \leq z \leq 1.6$ and residing in the three (low, medium and high) mass bins. Plot from Fassbender et al. (2011a).

properties of the distant galaxy cluster population that were investigated in Fassbender et al. (2011a). The findings reported in that paper, in fact, confirm that at $z \geq 0.9$ galaxy clusters start to deviate from the standard picture typical of the clusters at $z \sim 0$. Namely, Fassbender et al. (2011a) found that:

- the brightest cluster galaxies (BCGs) in distant clusters exhibit a statistically *higher* offset from the X-ray centroid (~ 50 kpc, with tail far beyond 100 kpc) compared to the local clusters (~ 20 kpc).
- BCGs in $z > 0.9$ clusters are *less dominant* than in the local universe. This property was quantified via the luminosity gap between the first- and the second-ranked galaxy Δm_{12} . For the distant systems a median of $\Delta m_{12,med} = 0.3$ mag, compared to $\Delta m_{12,med} = 0.7$ mag for $z = 0$, was found. In addition, the fraction of dominant BCGs ($\Delta m_{12} > 1$ mag) is $\leq 5\%$ for $z > 0.9$ clusters,

unlike the local universe where it reaches $\sim 37\%$.

The first two findings suggest that BCGs in distant clusters have generally not yet migrated to the center and are still actively accreting their stellar mass. This claim is further confirmed by the fact that distant clusters often do not show a clear BCG but instead *two or more* galaxies that are likely going to form the final BCG via one or more merging events.

An example of a *still forming* BCG has been found in the first of the three most distant XDCP clusters: XMMU J0338.8+0021 at $z = 1.49$. This system contains a central galaxy actually composed of two merging galaxies and exhibiting an offset from the X-ray emission of 175 kpc. The characteristics of XMMU J0338.8+0021 are discussed in detail in Chapter 5.

Chapter 4

F-VIPGI: a new pipeline for FORS2 spectroscopy

Abstract. This chapter refers to the work reported by Nastasi et al. (2013). The goal of this part of the thesis is twofold. Firstly, we present *F*-VIPGI, a new version of the VIMOS Interactive Pipeline and Graphical Interface (VIPGI) adapted to handle FORS2 spectroscopic data taken with the standard instrument configuration. Secondly, we investigate the spectro-photometric properties of a sample of galaxies residing in distant X-ray selected galaxy clusters, the optical spectra of which were reduced with this new pipeline. We provide basic technical information about the innovations of the new software and refer the reader to the original VIPGI paper for a detailed description of the core functions and performances. As a demonstration of the capabilities of the new pipeline, we then show results obtained for 16 distant ($0.65 \leq z \leq 1.25$) X-ray luminous galaxy clusters selected within the XMM-*Newton* Distant Cluster Project. We performed a spectral indices analysis of the extracted optical spectra of their members, based on which we created a library of composite high signal-to-noise ratio spectra. We then compared the average spectra of the passive galaxies of our sample with those computed for the same class of objects that reside in the field at similar high redshift and in groups in the local Universe. Finally, We computed the “photometric” properties of our templates and compared them with those of the Coma Cluster galaxies, which we took as representative of the local cluster population. We demonstrate the capabilities of *F*-VIPGI, whose strength is an increased efficiency and a simultaneous shortening of FORS2 spectroscopic data reduction time by a factor of ~ 10 w.r.t. the standard IRAF procedures. We then discuss the quality of the final stacked optical spectra and provide them in electronic form as high-quality spectral templates, representative of passive and

star-forming galaxies residing in distant galaxy clusters. By comparing the spectrophotometric properties of our templates with the local and distant galaxy population residing in different environments, we find that passive galaxies in clusters appear to be well evolved already at $z \sim 0.8$ and even more so than the field galaxies at similar redshift. Even though these findings would point toward a significant acceleration of galaxy evolution in densest environments, we cannot exclude the importance of the *mass* as the main evolutionary driving element either. The latter effect may indeed be justified by the similarity of our composite passive spectrum with the luminous red galaxies template at intermediate redshift.

4.1 Introduction

Galaxy clusters are the signature of the primordial density fluctuations that have grown via hierarchical accretion since the epoch of recombination. Because their abundance at different epochs is extremely sensitive to the matter content and acceleration of the universe, clusters are sensitive probes for testing different cosmological models. In addition, they are cosmic laboratories in which complex processes that shape galaxy evolution can be studied in great detail. Nowadays many efforts are invested into the observational challenge of providing sizable samples of galaxy clusters at high redshift ($z > 0.8$) to trace the evolution of the cluster population and its matter components back to the first half of the universe lifetime, corresponding to lookback times of $7 - 10$ Gyr. Many surveys have been designed to efficiently detect distant clusters by means of their red galaxy population (e.g., *SpARCS*, Wilson et al. 2006), their Sunyaev–Zel’dovich (SZ) effect signature (e.g., *SPT*, Williamson et al. (2011); *ACT*, Menanteau et al. (2010)) or the diffuse X-ray emission originating from the hot intracluster medium. The last approach, in particular, has proved very powerful to the above aim as shown e.g. by the *XMM*-Newton Distant Cluster Project (*XDCP*, Böhringer et al. 2005; Fassbender et al. 2011a). This is a serendipitous X-ray survey specifically designed for finding and studying distant X-ray luminous galaxy clusters at $z \geq 0.8$ and it has compiled the largest sample of such systems to date. For a comprehensive overview of the survey and an extensive discussion on its strategy and results we refer the reader to Fassbender et al. (2011a).

Irrespective of the initial approach used to detect distant clusters, the final mandatory step of the confirmation process is the redshift assessment of the system by means of spectroscopic observations of its galaxy population. To maximize the number of galaxies at $z > 0.8$ whose redshift can be successfully measured, one has to design spectroscopic campaigns to observe the spectral features with the highest signal-to-noise ratio (S/N). Because galaxy populations in clusters are dominated

by red, passive galaxies, the most suitable feature to this aim is the continuum break at 4000\AA (D4000) and the associated absorption calcium lines (CaH/K). For $z \sim 0.8 - 1$ this spectral region is redshifted to $\lambda \approx 7200 - 8000\text{\AA}$, a wavelength window readily accessible for many ground-based telescopes. In particular, one of the currently most efficient spectrographs able to cover this wavelength range and to simultaneously guarantee a very high and stable efficiency of its CCD up to $\lambda \sim 11000\text{\AA}$ is the FOcal Reducer and low dispersion Spectrograph (*FORS2*, Sec. 4.3.1) mounted on the UT1 of VLT. Because of its performances at longer wavelengths, this instrument is widely used for imaging and spectroscopy of distant cluster galaxies and is hence the instrument of choice for the spectroscopic follow-up of the distant candidate systems in XDCP.

At the time of writing XDCP provides the largest sample of X-ray selected distant galaxy clusters, with 30 confirmed clusters at $z > 0.9$ and a final aim of more than 50 clusters at $z > 0.8$ (30 at $z > 1$) to allow statistically meaningful evolution studies of the cluster population in at least three mass- and redshift bins. One of the main disadvantages connected to these expectations is the significant work related to reducing the large amount of data produced by the spectroscopic follow-up campaigns. Each XDCP target is observed with the *FORS2* multi-object spectroscopy (MOS) mode, enabling an average of 50 slits per mask. According to the survey expectations quoted above, the spectroscopic campaigns should finally yield several thousand slits, resulting in a similar amount of spectra to be reduced and extracted (see Fig. 4.2, left). This process is very time-consuming if carried out with the traditional IRAF packages, and the pipelines provided by ESO for automating the procedures would not provide the necessary accuracy for an efficient extraction of the spectra of such distant galaxies, which are mostly faint ($I > 20$)¹. These reasons motivated us to develop a new dedicated pipeline for a quick and efficient reduction of spectroscopic *FORS2* data. Because of the many similarities between *FORS2* and *VIMOS* data, we chose to build the new pipeline on *VIPGI* (Scodeggio et al. 2005) and named it *F-VIPGI*.

This chapter is structured as follows: in Sec. 4.2 the main characteristics of *VIPGI* are briefly described to introduce the innovations of *F-VIPGI*, which are extensively discussed in Sec. 4.3. We then show an application of the new pipeline to a sample of distant clusters (Sec. 4.4) that results in a new library of spectroscopic templates, while technical details and properties are discussed in Sec. 4.5 and a conclusive summary is given in Sec. 4.6. Throughout this chapter we assume a concordance Λ CDM cosmology, with $H_0 = 70 \text{ km s}^{-1} \text{ Mpc}^{-1}$, $\Omega_\Lambda = 0.7$, $\Omega_m = 0.3$ and $w = -1$.

¹Apparent Vega I-band magnitude of a $z > 0.5$ L* passively evolving galaxy with formation redshift $z_{\text{form}}=5$ and solar metallicity.

4.2 The VIMOS Interactive Pipeline and Graphical Interface

VIPGI is a semi-automatic data reduction pipeline released in 2005 (Scodeggio et al. 2005) written to process and archive the data obtained with the *VI*isible *Multi*Object *Spectrograph* (VIMOS) mounted at the Melipal Unit Telescope (UT3) of the VLT in a quick and efficient fashion. It is able to handle the data taken with all the three available VIMOS modes: MOS, imaging, and integral field unit (IFU) spectroscopy. The creation of such a new, VIMOS-dedicated, reduction pipeline was motivated by the need to process the huge amount of spectroscopic data expected from surveys such as the VIMOS-VLT Deep Survey (VVDS, Le Fèvre et al. 2004) or zCOSMOS (Lilly et al. 2007), each of which produced a total of $\sim 50,000$ spectra of galaxies in a very wide redshift range ($0 \leq z \leq 5$).

The core of VIPGI is a library of C-written routines, the VIMOS Data Reduction Software (DRS, Scodeggio et al. 2001), currently used by ESO for the VIMOS online reduction. All these fundamental functions can interact with each other and with the user thanks to the adopted standard Python Tkinter graphical interface. This choice allows one to obtain a pipeline where the power and efficiency of the C code computation and the possibility of a continuous quality check by the user on the intermediate reduction results are both present. Namely, the user can constantly monitor the quality of the ongoing reduction step by step with VIPGI, repeating an intermediate reduction step if necessary without restarting the entire procedure.

VIPGI was also designed to optimize the storage of a large amount of reduced data, with a clear and easily understandable filing strategy. More technical details on VIPGI are provided in the original paper of Scodeggio et al. (2005)

4.3 The FORS2-VIMOS Interactive Pipeline and Graphical Interface

Although VIPGI was specifically designed for the VIMOS instrument, its capabilities are general enough to make it potentially usable with any other MOS spectrograph. This motivated us to consider VIPGI as a potentially useful tool for XDCP, whose cluster candidates have been (or are planned to be) spectroscopically followed-up to safely confirm their nature of gravitationally bound, distant systems. The instrument used for this purpose is the *FO*cal *Red*ucer and *low dispersion Spectrograph* (FORS2) mounted on VLT. The XDCP spectroscopic campaigns have targeted ~ 70 cluster candidates since 2005, producing a total of $\sim 3,500$ single spectra to be extracted

and reduced. With the same original spirit of VIPGI we therefore adapted the power and efficiency of VIPGI to FORS2 data as well. The result is *F*-VIPGI, a new pipeline that allows us to shorten the time for reducing FORS2 spectroscopic data by a factor of ~ 10 w.r.t. the standard IRAF procedures.

4.3.1 The FORS2 instrument

FORS2 is the visual and near-UV FOcal Reducer and low-dispersion Spectrograph mounted on the UT1 unit (Antu) of the Very Large Telescope (VLT) (Appenzeller et al. 1998). The instrument covers the wavelength range from 330 nm to 1100 nm with an image scale of $0.25''/\text{pixel}$ (or $0.125''/\text{pixel}$ if the high-resolution collimator is used) in the standard readout mode (2x2 binning) and a field of view (FoV) of $6.83' \times 6.83'$. The detector consists of two MIT/LL CCID-20 chips, with 4096×2048 $15\mu\text{m}$ pixels, each characterized by an excellent sensitivity toward the red part of the spectrum (up to $\lambda \sim 11000\text{\AA}$) and the almost total absence of fringing pattern contamination. FORS2 can be used in many modes, including multi-object spectroscopy with exchangeable masks, long-slit spectroscopy, imaging, spectro-polarimetry and high-time resolution imaging and spectroscopy.

F-VIPGI was designed to work with all FORS2 data taken with the standard spectroscopic instrument configuration and straight slits, defined as those slits where the pixel-to-wavelength relation is “constant” along the slit length, and therefore the sky lines are perfectly aligned along the CCD rows (or columns, depending on the original orientation of the data). A summary of the properties of the FORS2 standard grisms equipment is provided in Tab. 4.3.1.

4.3.2 Conversion of FORS2 files into the VIMOS format

The functionalities of *F*-VIPGI were enabled not by creating new routines specifically coded for the FORS2 data format but instead by *manipulating* the FORS2 data themselves to convert them into the VIMOS format. Despite the differences between FORS2 and VIMOS CCDs architectures (with four squared sensors for the former and two rectangular ones for the latter), our idea was to make the software able to identify chips 1 and 2 (hereafter Q1 and Q2, respectively) of FORS2 as the first two individual quadrants of VIMOS. In this way one can use the standard VIPGI recipes with the “adapted” FORS2 fits files without affecting the quality and reliability of the data reduction results. The parts of FORS2 data that are manipulated by *F*-VIPGI are the *image* and the *header*:

- *image*: the original FORS2 matrix of 4096×2048 pixels is *transposed* to obtain

Table 4.1: Properties of the grism forming the FORS2 standard instrument configuration for which *F*-VIPGI is usable. In parenthesis are the wavelength ranges actually used by *F*-VIPGI to provide the best-quality results. The listed values of resolution $\lambda/\Delta\lambda$ are computed at the central wavelength and for a 1'' slit.

Grism name	Central wavelength [nm]	Wavelength range [nm]	Dispersion		Resolution $\lambda/\Delta\lambda$	Order separation filter
			[Å/mm]	[Å/pixel]		
GRIS_600B+22	465	330 - 621	50	1.50	780	none
GRIS_300V+10	590	330 (350) - 660 (925)	112	3.36	440	none
GRIS_300V+10	590	445 (450) - 865 (850)	112	3.36	440	GG435+81
GRIS_300I+11	860	580 (600) - 1100 (1050)	108	3.24	660	none
GRIS_300I+11	860	600 - 1100 (1050)	108	3.24	660	OG590+32
GRIS_150I+27	720	330 (370) - 650 (980)	230	6.90	260	none
GRIS_150I+27	720	445 (430) - 880 (990)	230	6.90	260	GG435+81
GRIS_150I+27	720	600 (590) - 1100 (1050)	230	6.90	260	OG590+32

the same vertical orientation of the VIMOS frames. The wavelength dispersion orientation from lower (blue) to upper (red) side of the image is recovered in the same way. We also stress that this process does not affect the quality of the data because only the positions of the pixels are rearranged, whereas their information (counts) are left untouched.

- *header*: the header structure of FORS2 files differs significantly from those of VIMOS. In particular, while in each VIMOS file the header contains only the information on the slits of the chip to which the file belongs, in FORS2 each file has the information of all the slits of the mask on its header that are associated with Q1 and Q2. During the conversion process *F*-VIPGI therefore changes these settings and removes all the information about the slits that do not belong to the chip of the frame itself. Only the six reference slits, common to both chips, are preserved along this process. We highlight that these changes are made for all FORS2 frames except the BIAS, as they do not contain any slit information in their headers.

A specific and slightly different treatment is reserved to standard-star frames (STD), as discussed in Sec. 4.3.7.

4.3.3 *F*-VIPGI calibration files

As for VIPGI, the user has to initially provide specific calibration files also for *F*-VIPGI. These are then used by the pipeline to locate the position and length of the slits on the CCD, to compute the coefficient of the interpolating polynomial for the wavelength dispersion, to correct for bad CCD pixels, and to finally extract the single 1-D spectra. The calibration files are the following:

- *grism table*: it contains all the main spectroscopic information of the grism, i.e. central wavelength, wavelength range, and resolution. The emission sky lines usable for an additional refinement of the wavelength calibration (see 4.3.4) are defined here, too. It is defined for each grism configuration.
- *CCD table*: it maps all bad pixels/columns of the CCD that have to be corrected for by the pipeline. Two different files are needed for Q1 and Q2, but these remain the same for any FORS2 observation.
- *line catalog*: it contains the list of all arc lines used for the wavelength calibration (Sec. 4.3.4). For FORS2 only three files are needed, depending on the kind of lamp used (HeAr, HgCdHeAr or HgCdHeNeAr).

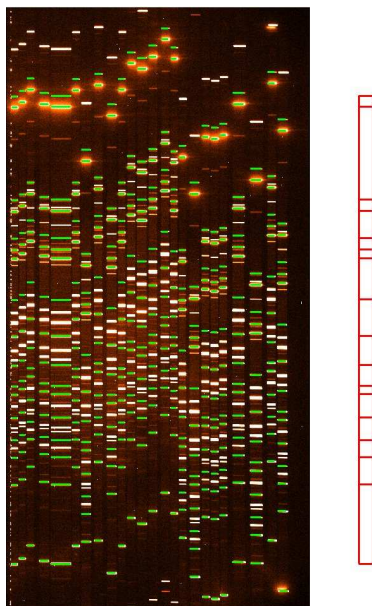


Figure 4.1: An example of a HeAr arc line catalog displayed on a raw lamp frame (in background) within *F*-VIPGI. The green regions mark the expected positions of the arc lines according to the information extracted from the fits header while the red ones on the right represent the line catalog used for the calibration. The red part of the spectrum is in the upper part of the image.

- *grism PAF file*: it is a parameter file in the standard ESO data interface control terminology. Basically, it is just a text file where information can be collected in a format that is very similar to the FITS keywords format and is then used to update FITS keywords in the header of FITS files. Specifically, this file contains all information related to the wavelength dispersion, optical distortion, and curvature of each CCD and each grism.
- *SPHOT table*: it is a fits table containing magnitude vs. wavelength of the standard star that is used for the spectrophotometric calibration of the data. It has to be named exactly as the target name reported in the header keyword “ESO OBS TARG NAME”.

All the above calibration files except for the SPHOT table are provided together with the installation package and should not be modified by the user.

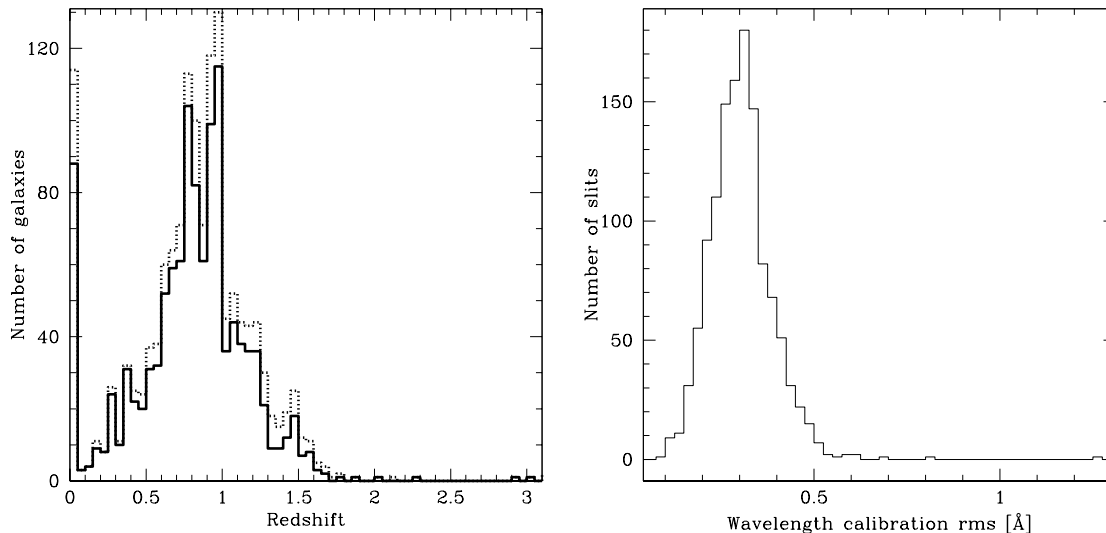


Figure 4.2: *Left*: Redshift distribution of 1543 FORS2 spectra produced by XDCP and extracted with *F*-VIPGI. The solid line marks the secure assigned redshifts ($\geq 75\%$ confidence on the assigned value) while the dotted line refers to unsafe ones (confidence $\leq 50\%$). The secure assessments represent $\sim 72\%$ of the entire sample at $0 < z \leq 3$ and increases to $\sim 78\%$ including also stars. *Right*: Distribution of rms wavelength calibrations computed for the corresponding 1230 reduced slits observed with the grism 300I+11. The median value is $\langle \text{rms} \rangle_\lambda = (0.30 \pm 0.05) \text{ \AA}$.

4.3.4 Wavelength calibration

One of the most powerful aspects of VIPGI, and hence of *F*-VIPGI, is that the user can perform sensitive calibration steps via visual tools that facilitate executing and constantly checking all the procedures. An example of this interactivity within the reduction process is shown in Fig. 4.1. Here the pipeline shows the expected positions of the arc lines of each slit (green regions overlaid on the raw lamp frame) together with the line catalog used for the calibration (red regions on the right side). The user can iteratively refine the wavelength calibration across the entire chip by shifting each green line until the region line patterns perfectly match the underlying lamp frame. The positions of the line centroids are then computed automatically by the pipeline by applying a 2.5 sigma iterative rejection to remove lines that deviate too far from the fit. This method produces a very accurate calibration with a median uncertainty on the wavelength calibration that roughly corresponds to one fifth of a pixel. As an example, for grism 300I+11, whose spectra have a linear dispersion of

3.24Å/pixel, the typical uncertainty on the wavelength calibration has an $\langle \text{rms} \rangle_\lambda = (0.30 \pm 0.05)\text{Å}$, as shown in the right panel of Fig. 4.2.

Another refinement of the calibration can also be obtained by using the position of some bright relatively isolated sky emission lines whose wavelengths are known and defined in the *grism table* (see Sec. 4.3.3). For data taken with grism 300I+11 we used eight sky lines between $\lambda = 6300\text{Å}$ and $\lambda = 10120\text{Å}$, which produced a final refined wavelength calibration with a typical $\langle \text{rms} \rangle_\lambda < 1\text{Å}$. This quantity can be converted into a corresponding redshift uncertainty of $\delta z_\lambda \sim 1 - 2 \cdot 10^{-4}$ by referring to $\lambda_c = 8600\text{Å}$. After the calibration process, all data are preliminarily reduced in the standard way by subtracting the bias frames, correcting for the CCD bad pixels and, finally, applying the flat-fielding correction.

4.3.5 Sky line subtraction and atmospheric absorption corrections

A significant source of noise along the spectroscopic reduction process is introduced by the strong absorption (telluric) and emission sky features produced by the O_2 and H_2O molecules and the OH^- radical at $\lambda > 6000\text{Å}$ (see Fig. 4.3, top). *F*-VIPGI is able to remove the two undesired sky contributions in a very efficient way, as shown in Fig. 4.4.

The sky emission spectrum is computed for each slit in the *free regions*² on the sides of the science spectrum. If this area is large enough (at least $2''$ left between the spectrum and the slit edges, on both sides), the sky lines can be accurately modeled and efficiently subtracted from the final spectrum, as shown in the bottom panels of Fig. 4.3 and 4.4. After sky subtraction, we need to correct all the spectra also for the prominent sky absorption features (telluric lines) that could otherwise be interpreted as absorption lines in the object spectra. These spurious features can be removed provided that a sufficient number of well exposed flux calibrated spectra are available. Even if the best results are obtained when the spectra selected for the correction span a wide redshift range (because the intrinsic features are efficiently removed in this way and only the sky ones are enhanced), a good telluric line absorption correction can also be gained by using cluster galaxies, whose redshift values are relatively close

²These regions are identified automatically by the pipeline with the following procedure: first a “slit profile” is traced by collapsing the data along the wavelength axis. The mean signal level and rms (sigma) of this slit profile are then computed with a robust iterative procedure by using the biweight estimator described by Beers et al. (1990). Finally, all groups of at least three pixels that are N sigma above the mean level are considered as object spectra while everything else is considered free sky region. In the above process the sigma threshold (N) can be set by the user.

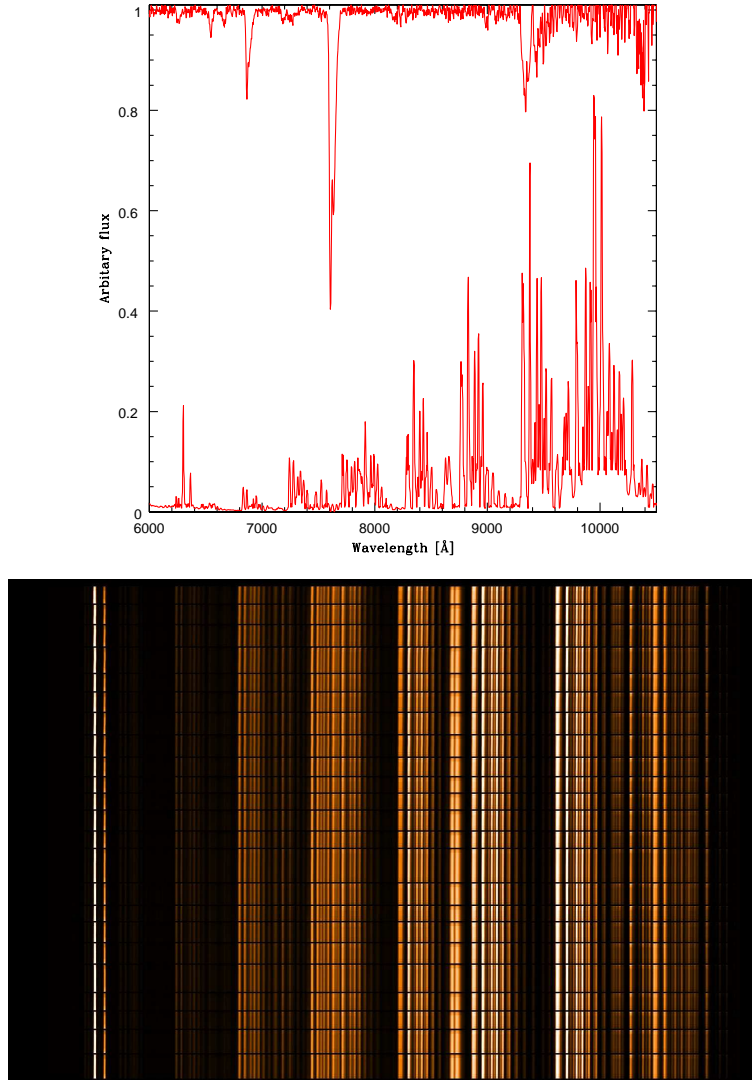


Figure 4.3: *Top*: Spectral absorption (top side) and emission (bottom side) features introduced by the night sky in the $\lambda > 6000\text{\AA}$ spectral region. *Bottom*: 2D emission spectra of the sky extracted for all slits of a FORS2 mask. The vertical alignment of the sky lines is indicative of a very good wavelength calibration over the entire mask.

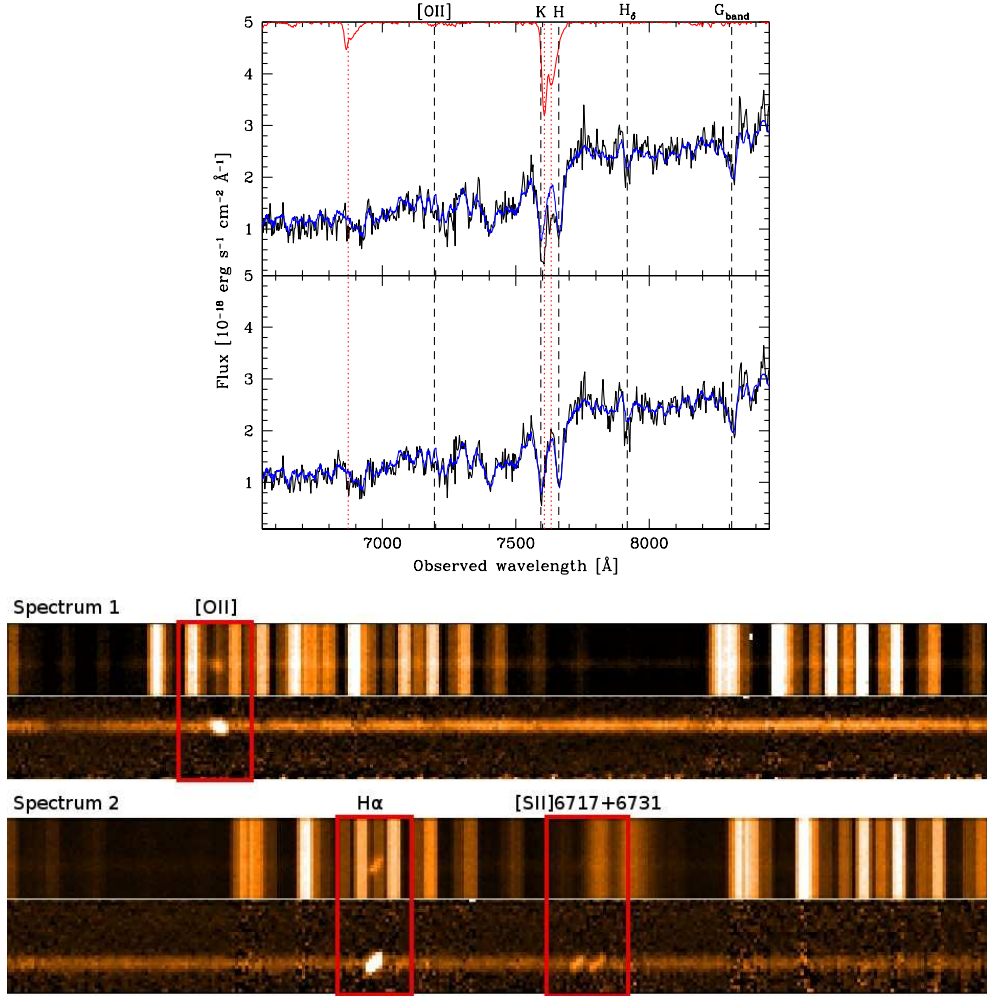


Figure 4.4: Example of the good quality achievable through the removal of absorption (top) and emission (bottom) sky features with *F*-VIPGI. **Top panel:** Atmospheric correction for a spectrum of a passive galaxy at $z \sim 0.9$ observed with grism 300I. *Top:* Flux-calibrated spectrum (in black) without the atmospheric correction applied. It is evident that the telluric lines at $\lambda \sim 7600 \text{\AA}$ strongly affect the S/N of the 4000-\AA break and the CaII (H, K) lines. *Bottom:* The same spectrum after applying the atmospheric absorption correction. Now the CaII lines are completely recovered. In red (solid and dotted curves) the positions of the most prominent telluric lines are shown. The black dashed lines mark the position of the most important spectral features in the displayed wavelength range. The best-fitting template of both spectra (an LRG one at $z = 0.930$) is overlaid in blue in both panels for reference. **Bottom panel:** Subtraction of the emission sky lines from two spectra with different redshift (*spectrum1* at $z = 1.086$, *spectrum2* at $z = 0.282$). For each object the same part of the spectrum before and after the sky subtraction is shown at the top and bottom, respectively. In addition, the strongest spectroscopic features of each object are marked by the red boxes and are labeled on the top side. Although some residuals of the sky removal are visible in the bottom panels, the pipeline efficiently subtracts the undesired sky features and recovers the science features, which are sometimes completely outshone by the atmospheric emission.

to each other. If so, the pipeline finds the atmospheric correction by combining the spectra whose telluric lines are more evident and isolated and finally applies such a correction to *all* slits of the mask. An example of the good quality achievable for telluric line absorption correction is shown in the top panel of Fig. 4.4.

4.3.6 The final product

Once the preliminary reduction and the wavelength calibration are applied to each frame, these are calibrated in flux (see Sec. 4.3.7) and finally combined to obtain a stack of 2D sky-subtracted spectra. Single spectra are then extracted from the 2D stacked frame, using a Horne optimal extraction (Horne 1986), and are saved in local folders in fits format. For each spectrum *F*-VIPGI also produces the associated noise vector generated by the extraction residual.

4.3.7 Spectrophotometric calibration

An important difference of the FORS2 observations to those of VIMOS concerns the methods used by the two instruments to acquire the spectra of spectro-photometric standard stars (STD). This step is mandatory to calibrate each spectrum in flux and to correct its continuum shape for the CCD sensitivity function. Standard stars in VIMOS are observed in all four quadrants and with a specifically designed mask composed of eight slits per chip, with fixed position and length (10''). In FORS2, instead, the STD frame is acquired only on Q1 and by means of a single *long-slit* with 5'' width. To overcome this discrepancy and enable the use of the standard VIPGI routines for spectrophotometric calibration also for FORS2 data, *F*-VIPGI writes some keywords into the header of the standard star frames (and into the correlated calibration files) that *mimic* the presence of 11 slits in total (6 in Q1 and 5 in Q2)³ with 30'' length and 1'' width. It is important to note that in FORS2 observations the standard star spectra are always centered on Q1 at the position given by the header keywords CRPIX1 and CRPIX2. The virtual slits are therefore created in the way to have the first slit (#1 of Fig. 4.5) always centered on (CRPIX1, CRPIX2) and, so, always contain the star spectrum. An example of the part of the *virtual* mask relative to Q1 is shown in Fig. 4.5. Once the standard-star spectrum is reduced and extracted, the pipeline computes the sensitivity function by comparing the observed stellar spectrum with the expected one contained in the SPHOT table (Sec. 4.3.3) as shown in Fig. 4.6. The extracted curve is finally saved in a calibration table that can

³This is the maximum number of 30'' length slits that can be uniformly placed on the area of the two chips.

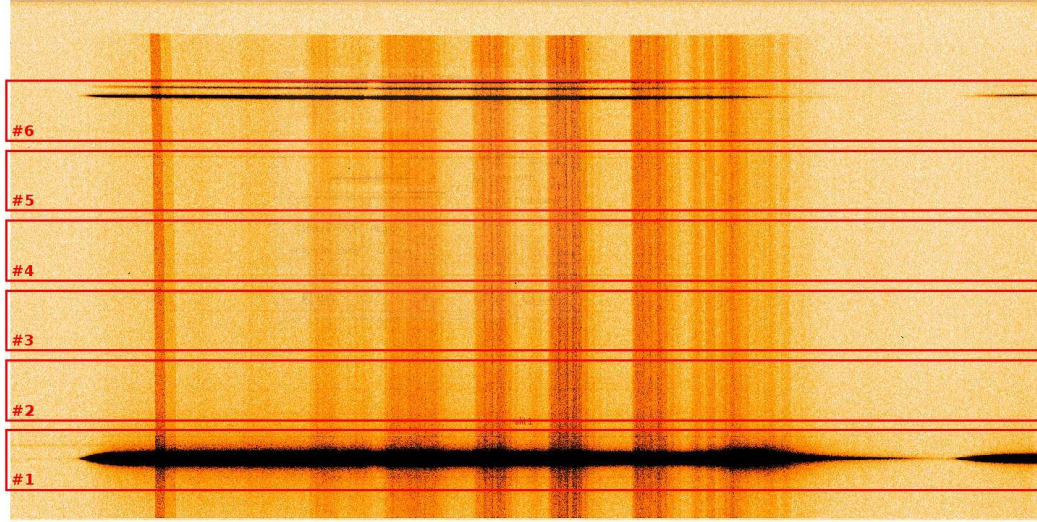


Figure 4.5: Image of the spectrum of a standard star taken with the FORS2 300I instrument setup in the first chip (Q1). In red are shown the *virtual* slits of 30'' length that *F*-VIPGI creates in the header of the scientific and calibration frames of the standard stars to mimic the VIMOS setting. In FORS2 observations the standard star spectra are always imaged in Q1 and are always enclosed in the first (#1) virtual slit.

be applied to the 1-D spectra for their flux calibration and for the correction of the CCD response function. Since standard stars in FORS2 are observed only on Q1, for Q2 data the same calibration table as computed for the first chip has to be used. An example of how the sensitivity function is computed for a standard star observed with the 300I grism is shown in Fig. 4.6.

4.3.8 Redshift accuracy test

The XDCP massive cluster XMMUJ1230.3+1339 at $z = 0.975$ (Fassbender et al. 2011b; Lerchster et al. 2011) has been targeted by four different FORS2 spectroscopic observations in order to fully characterize its extended and dynamically unrelaxed galaxy population. This resulted in 65 confirmed spectroscopic members, 15 of which had multiple (double) observations. This enabled us to use these targets for a self-consistency test on the *F*-VIPGI redshift measurements, based on different independent spectroscopic observations of the same object.

To this aim we selected 14 out of the 15 duplicated observations, considering

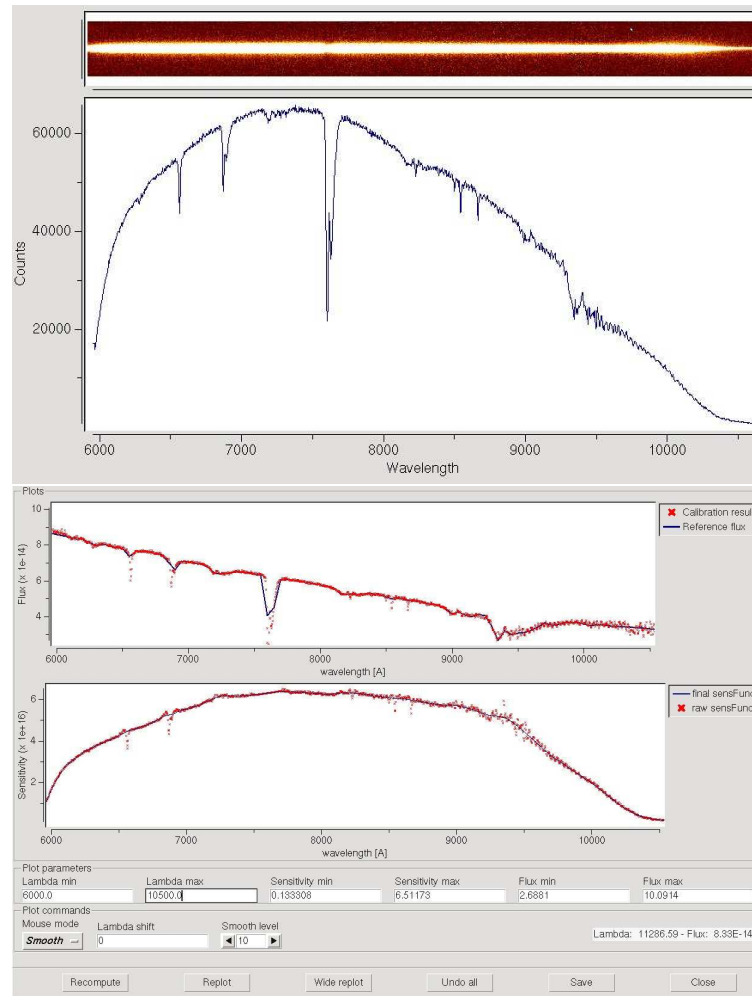


Figure 4.6: Example of the spectrophotometric calibration for a FORS2 observation with grism 300I and sorting filter OG590. **Top panel:** Extracted 1-D spectrum of the standard star, not yet corrected for the CCD response function. **Bottom panel, top:** The expected spectrum of the standard star provided by the SPHOT table (continuous line) and the fitted one (red points) according to the spectral resolution of the observation. The sensitivity function (**bottom panel**) is then computed as the ratio between the extracted 1-D spectrum and the fitted standard star spectrum converted into $\text{erg cm}^{-2} \text{s}^{-1} \text{\AA}^{-1}$. The user can edit the originally computed sensitivity function (red points) and choose the final one (continuous line) to apply to the single spectra for calibrating them into flux.

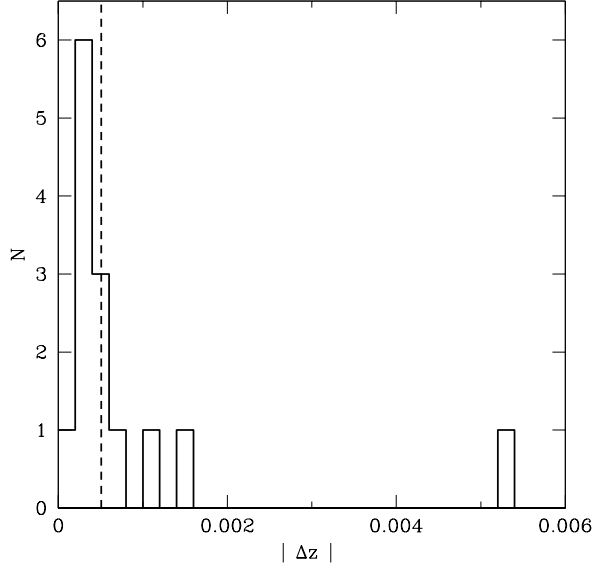


Figure 4.7: Distribution of the absolute values of the differences between the redshift measurements $|\Delta z|$ for 14 members of XMMUJ1230.3+1339 at $z = 0.975$ from multiple, independent, spectroscopic observations. The median value of $\langle |\Delta z| \rangle = 5.1 \cdot 10^{-4}$ is marked by the vertical dashed line.

only those couples where the final extracted data were good enough to provide a safe redshift assessment for both cases. The median of the differences (in absolute value) between the redshift measurements is $\langle |\Delta z| \rangle = 5.1 \cdot 10^{-4}$, with a spread given by the semi-interquartile range (SIQ) of $\langle |\Delta z| \rangle_{SIQ} = 2.5 \cdot 10^{-4}$. This value can be translated into a corresponding *rest-frame* velocity uncertainty of $\delta_{v,rest} \approx 77 \text{ km s}^{-1}$ for a galaxy at $z = 0.975$.

The distribution of $|\Delta z|$ is shown in the histogram of Fig. 4.7.

4.4 An application to a sample of distant galaxy clusters

In this section we show an application of *F*-VIPGI to the analysis of spectroscopic data for a sample of 16 distant XDCP galaxy clusters in the redshift range ($0.65 \leq z \leq 1.25$) observed with the grism 300I+11 (Tab. 4.3.1). The main goal of this section is to provide the community with a new set of spectroscopic templates that

are intended to represent the galaxy population residing in distant galaxy clusters. For this reason, as shown in Sec. 4.5.1, the present library is completely different from the existing ones (e.g., the ones constructed from SDSS, zCOSMOS or K20 surveys), which contain templates representative of the population of field galaxies at different redshifts up to $z \sim 1.5$. In addition to identifying redshifts of distant galaxies, the provided templates can also significantly improve the efficiency and the reliability of the *photometric* redshift assessment of distant clusters with complex star formation histories (see, e.g., Guennou et al. (2010) and Pierini et al. (2012) for a discussion) and they can be used to predict rest-frame $U - B$ colors of cluster galaxies at high redshifts.

4.4.1 The spectroscopic sample

For our study we selected all the XDCP clusters with at least three spectroscopically confirmed members with an $S/N > 2$ in the rest frame wavelength range of 4000 - 4300 Å in their reduced spectra. Each spectrum was also visually inspected to verify that no contaminations from cosmic rays or bad sky subtraction were present. For the cluster member selection, we firstly estimated the redshift cluster (z_{cl}) as the median of the redshift peak found in the proximity of the X-ray emission center. After that, we selected the cluster members as those galaxies with a rest-frame velocity offset $< 3000 \text{ km s}^{-1}$ from z_{cl} , corresponding to a redshift window cut of $\Delta z < 0.01 \times (1 + z_{cl})$.

The list of the final targets selected for the next spectroscopic analysis is reported in Tab. 4.2. For each target a sequential ID, the spectroscopic redshifts, the number of confirmed members used in the subsequent analysis, and the literature reference (if existing) are reported. A total of 187 cluster members have been identified in this way, with a redshift distribution in the range $0.65 \leq z \leq 1.25$ as shown in Fig. 4.8.

4.4.2 Spectral indices analysis results

We grouped the above galaxies into five different spectral classes according to the measured⁴ values of the equivalent widths (EW) of their [OII] and H δ lines, as summarized in Tab. 4.3. These two spectral features are, in fact, reliable indicators of ongoing and recent star formation activities within timescales of $\sim 10^7$ yr and $\sim 10^9$ yr for [OII] and H δ , respectively. The amplitude of their 4000-Å break (D4000) and the equivalent widths of $H\beta$, [OIII] λ 4959 and [OIII] λ 5007 were also computed

⁴All spectral indices were measured in an automated way by means of a Python script developed by our group that uses the trapezoidal rule to perform the integration. The code functioning was tested on some spectra by comparing its results with those provided by the standard IRAF packages.

Table 4.2: List of the 16 XDCP clusters selected for our spectroscopic analysis.

ID	z_{spec}	$N_{members}$	References
cl1	0.7690	13	(1)
cl2	1.2310	8	(1)
cl3	0.9410	16	(1)
cl4	0.9590	6	C20 in (2)
cl5	0.8290	8	(1)
cl6	0.7850	5	(1)
cl7	0.6770	12	(1)
cl8	0.8830	4	(1)
cl9	0.8940	19	(1)
cl10	0.7890	13	(1)
cl11	1.1220	7	C11 in (2)
cl12	1.0740	3	(1)
cl13	0.8270	9	(1)
cl14	0.7460	7	(1)
cl15	0.9750	52	XMMU J1230.3+1339 in (3) and (4)
cl16	1.2030	7	(1)

References: (1) To be published; (2) Fassbender et al. (2011a); (3) Fassbender et al. (2011b); (4) Lerchster et al. (2011)

Table 4.3: Classification criteria taken from Poggianti et al. (2009) used in this study for grouping the cluster galaxies into five spectral types according to the equivalent widths values of their [OII] λ 3727 and H δ lines. The following convention is used: $EW < 0$ for *emission* lines, $EW > 0$ for *absorption* lines. The number of galaxies found in each class is given in the last column.

Spectroscopic class	EW([OII]) value [Å]	EW(H δ_A) value [Å]	Number of galaxies
passive	>-5	<3	108
post-starburst	>-5	≥ 3	21
quiescent star-forming	$]-25, -5]$	<4	23
dusty starburst	$]-25, -5]$	≥ 4	14
starburst	≤ -25	any	21

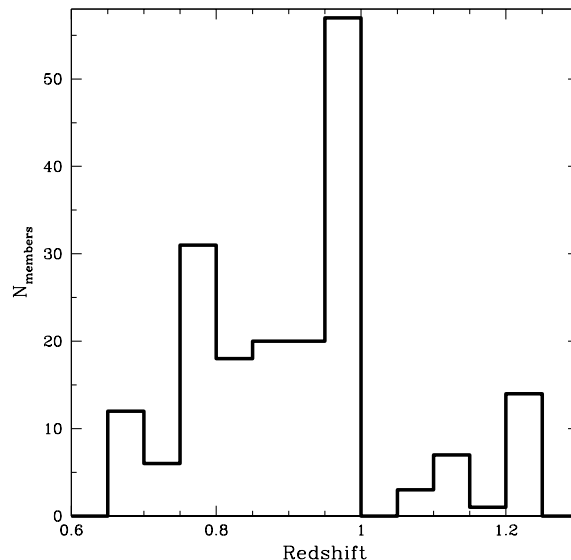


Figure 4.8: Redshift distribution of the selected 187 galaxies, members of the 16 XDCP clusters reported in Tab. 4.2.

but were not used for the spectral classification. The errors on the indices were estimated by means of the noise vector provided by *F*-VIPGI for each extracted spectrum at the end of the reduction process (see Sec. 4.3.6). Specifically, for each spectrum 1000 Monte-Carlo realizations were generated using the related noise vector as variance. The uncertainties on the indices were then computed as the rms of the results obtained by repeating the spectral indices analysis on the series of simulated spectra.

We stress that the relative fraction of galaxies in the different spectral types is substantially biased by the method used in XDCP to select the targets for the spectroscopic follow-up. As discussed in Fassbender et al. (2011a), to maximize the probability of targeting actual cluster members, FORS2 masks are created in a fashion that the slits are preferentially placed on color-selected galaxies close to the expected red-sequence color and within the detected X-ray emission. This implies that the *majority* of the observed targets is actually expected to be passive and, hence, that no statistically significant conclusions about the relative number of galaxies in the different classes can be inferred from the last column of Tab. 4.3. We adopted the bandpasses defined in Balogh et al. (1999) for $EW([OII])$ and $D4000$ (hereafter D_n4000) while for $EW(H\delta)$ we used the definition of $H\delta_A$ given by Worthey

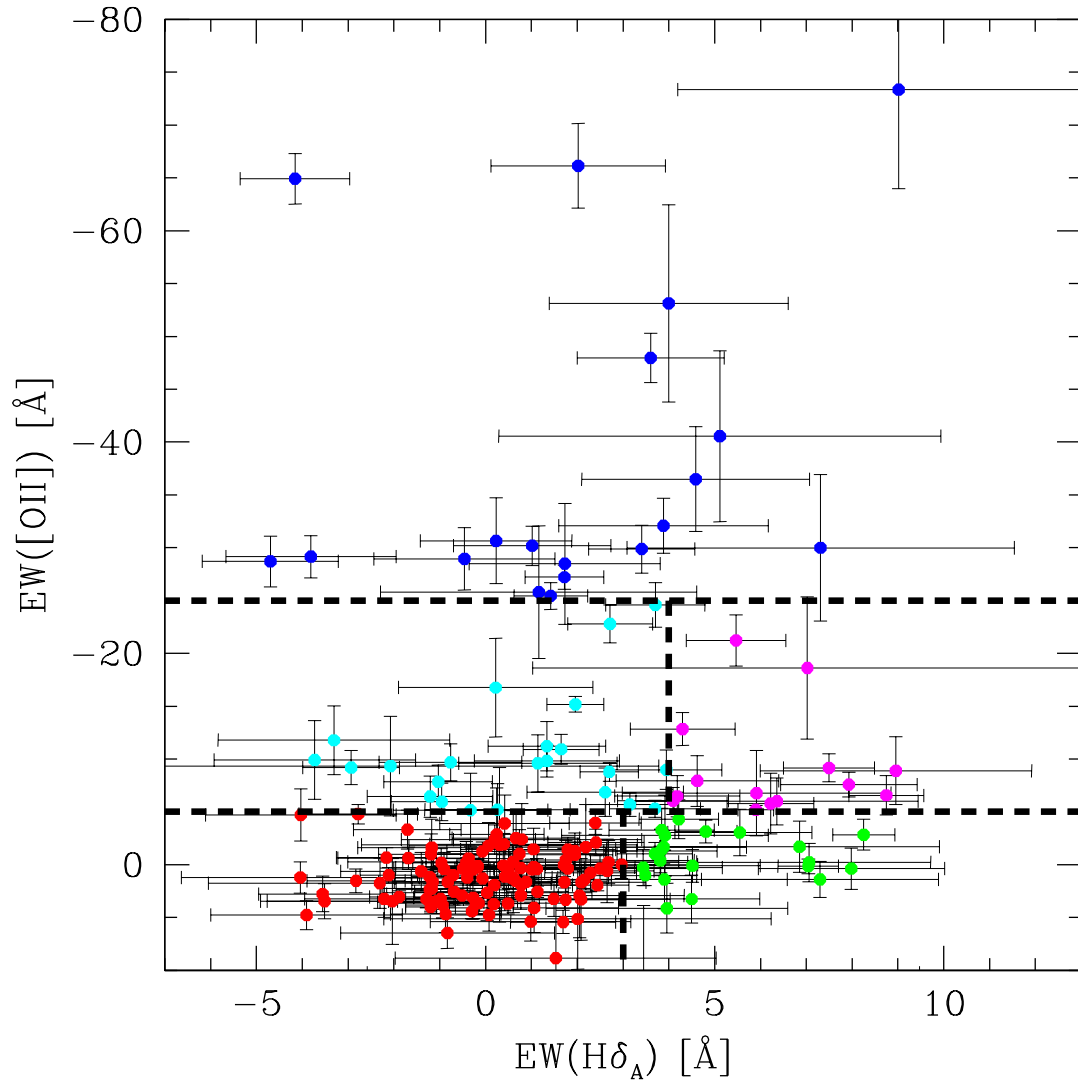


Figure 4.9: Distribution of the 187 galaxies in $EW([OII])$ - $EW(H\delta_A)$ plane. The dashed lines and the different colors mark the positions of the five spectral classes, with the same criteria as in Poggianti et al. (2009). The color code is the following: *blue*: starburst galaxies; *cyan*: quiescent star-forming; *magenta*: dusty-starburst; *red*: passive; *green*: post-starburst.

& Ottaviani (1997). The galaxies were classified into five spectral classes following the same method as described in Poggianti et al. (2009), which is based only on the strength of [OII] and $H\delta_A$ lines, as summarized in Tab. 4.3.

Fig. 4.9 shows the distribution of the 187 galaxies in the $EW([OII])$ - $EW(H\delta_A)$ plane. The adopted loci for the five spectral classes are marked by the dashed lines and a color coding was used for a better visualization of the groups.

The D_n4000 index was then used to qualitatively test the validity of our classification. The top panel of Fig. 4.10 shows the distribution of our galaxy sample in the $EW(H\delta_A)$ vs D_n4000 space with the color code adopted in Fig. 4.10 for identifying the different spectral classes. The distribution we find is remarkably similar to that reported in Fig. 1 of Gallazzi & Bell (2009) for a set of model galaxies. Namely, we observe that consistently with the results of these authors, the starburst (dusty and not) galaxies tend to be concentrated on the upper left side of the plot, indicating a relatively young (and still forming) stellar population. The passive and quiescent star-forming galaxies instead reside mostly in the center and on the lower right side, suggesting that they experienced the last episode of major star-formation activity more than 3 Gyr earlier. Finally, the *post-starbursts* are all located above the sequence drawn by the passive and quiescent star-forming galaxies, a sign that their starburst activity ended within the previous 2 Gyr. In the bottom panel of Fig. 4.10 the distribution in the D_n4000 - $EW([OII])$ diagram is shown. It is evident also here that for the adopted classification method the different spectral classes are confined to specific regions of the plots. In particular if we consider the relation adopted by Franzetti et al. (2007),

$$D_n4000 + EW([OII])/15 > 0.7$$

(marked by the dotted line in the plot) to divide passively evolving (*early-type*) galaxies from star-forming (*late-type*) objects for a spectroscopic sample of VVDS galaxies at $0.45 \leq z \leq 1.2$, all passive and post-starburst galaxies appear to be efficiently separated from the starburst ones. However, the plot also shows that the majority of quiescent star-forming and dusty-starburst galaxies are classified as early-type in this way. This effect was already predicted by the same authors, who claimed that some contamination in the early-type region was expected due to early spirals and that this is a general feature observed for color- or spectroscopic classification schemes.

To identify possible active galactic nuclei (AGNs, e.g. Seyfert 2) erroneously identified as starburst galaxies, we used the diagnostic diagram of Bongiorno et al. (2010), that was originally defined in Lamareille et al. (2004) (and references therein), where the ratios between the EW of [OII] λ 3727, $H\beta$, and [OIII] λ 5007 lines are used to

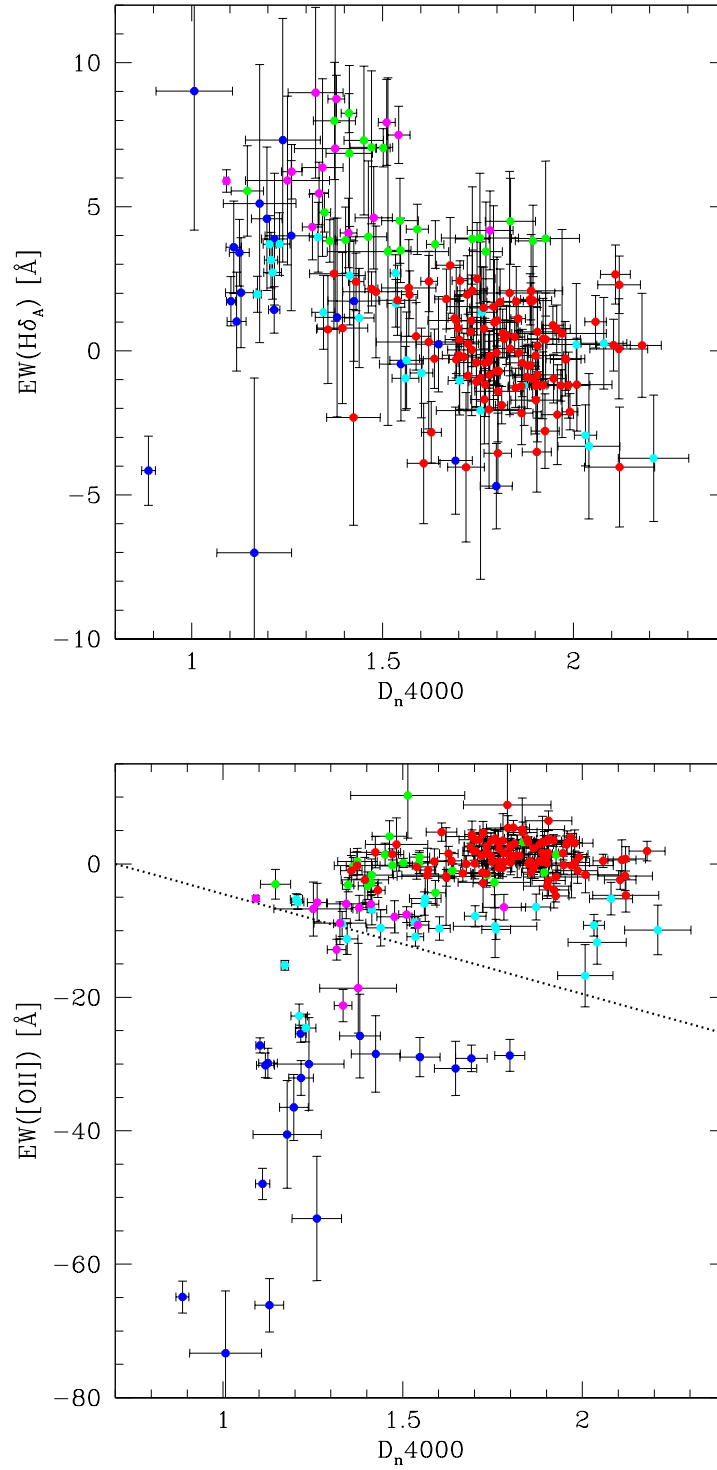


Figure 4.10: D_n4000 versus $EW([OII])$ (*top* panel) and $EW(H\delta_A)$ (*bottom* panel) for the selected targets. The dotted line in the right panel represents the division between early-type / late-type galaxies adopted in Franzetti et al. (2007). The color code is the same as in Fig. 4.9.

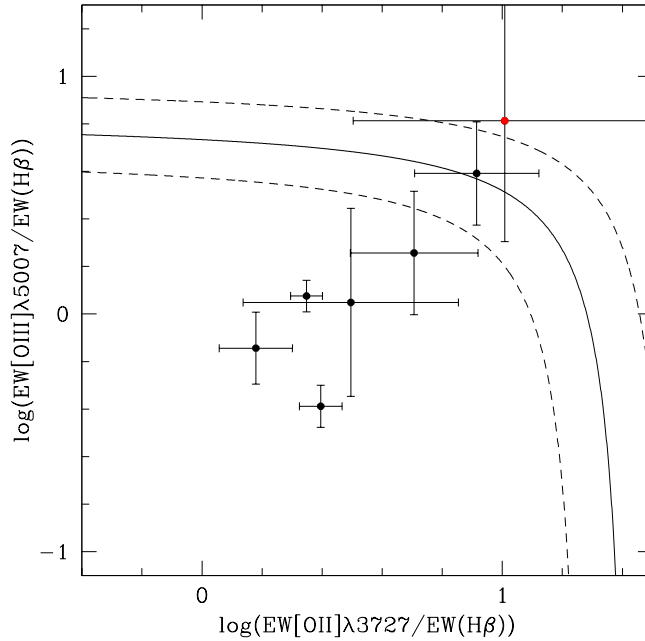


Figure 4.11: Diagnostic diagram used by Bongiorno et al. (2010) to distinguish between pure star-forming and AGN-contaminated galaxies applied to those galaxies of our sample classified as starburst (see Tab. 4.3) and lying at redshift $0.6 < z < 0.95$ to have their [OIII] $\lambda 5007$ line falling within the observed wavelength range. The solid and dashed curves show the demarcation and its $\pm 0.15dex$ uncertainty, respectively, between pure star-forming galaxies (bottom region) and AGN (top region), as defined in Lamareille et al. (2004). The red point marks the starburst object possibly hosting an AGN that was therefore excluded from the final stacking procedure.

separate star-forming from AGN-photoionized spectra. The constraint of having the [OIII] $\lambda 5007$ line within the observed wavelength range $6000\text{\AA} < \lambda_{obs} < 9800\text{\AA}$ makes this analysis feasible only for seven starburst galaxies lying at redshift $z < 0.95$. In Fig. 4.11 the distribution of these objects in the $\log(EW[\text{OII}]\lambda 3727/EW(\text{H}\beta))$ vs $\log(EW[\text{OIII}]\lambda 5007/EW(\text{H}\beta))$ plane is shown. Only one object (marked in red) appears to lie in the “AGN region” of the plot and was consequently excluded from the final stacking of the starburst spectra.

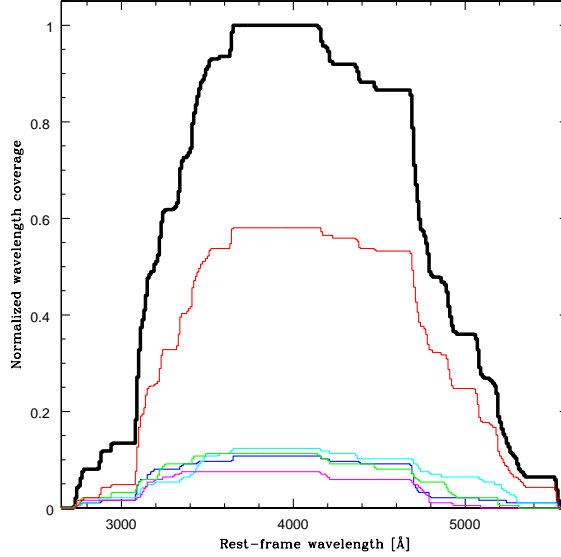


Figure 4.12: Normalized rest-frame wavelength coverage for the 186 galaxies used in the stacking procedure. The general result for all galaxies is represented by the thick solid curve, while the thinner lines indicate the different contributions from the five spectral classes defined in Sec. 4.4.2. The same color code as in Fig. 4.9 is used.

4.5 A new library of spectroscopic templates

Before proceeding with the final stacking procedure, we restricted the usable portion of each spectrum to the observed wavelength range of 6100 - 9280 Å. This cut was made to avoid the highly sky-contaminated region at $\lambda \geq 9300$ Å (Fig. 4.3, top) while simultaneously preserving the observability of spectral features like $H\beta$ and [OIII] for galaxies up to $z \sim 0.85$.

The total rest-frame wavelength range covered by the composite spectra is 2700 - 5300 Å, with a normalized *wavelength coverage* for all 186 considered galaxies shown in Fig. 4.12. In the same figure we also show the different contributions from the five spectral classes defined in Sec. 4.4.2. We recall that here the possible AGN-contaminated starburst object of Fig. 4.11 was excluded from our analysis.

For the final stacking process each spectrum was rescaled to the mean flux computed in the wavelength range $4000\text{Å} < \lambda < 4300\text{Å}$ and then combined with the other objects of the same spectral class using the median as operator.

The resulting five composite spectra are shown in Fig. 4.13. For each spectrum

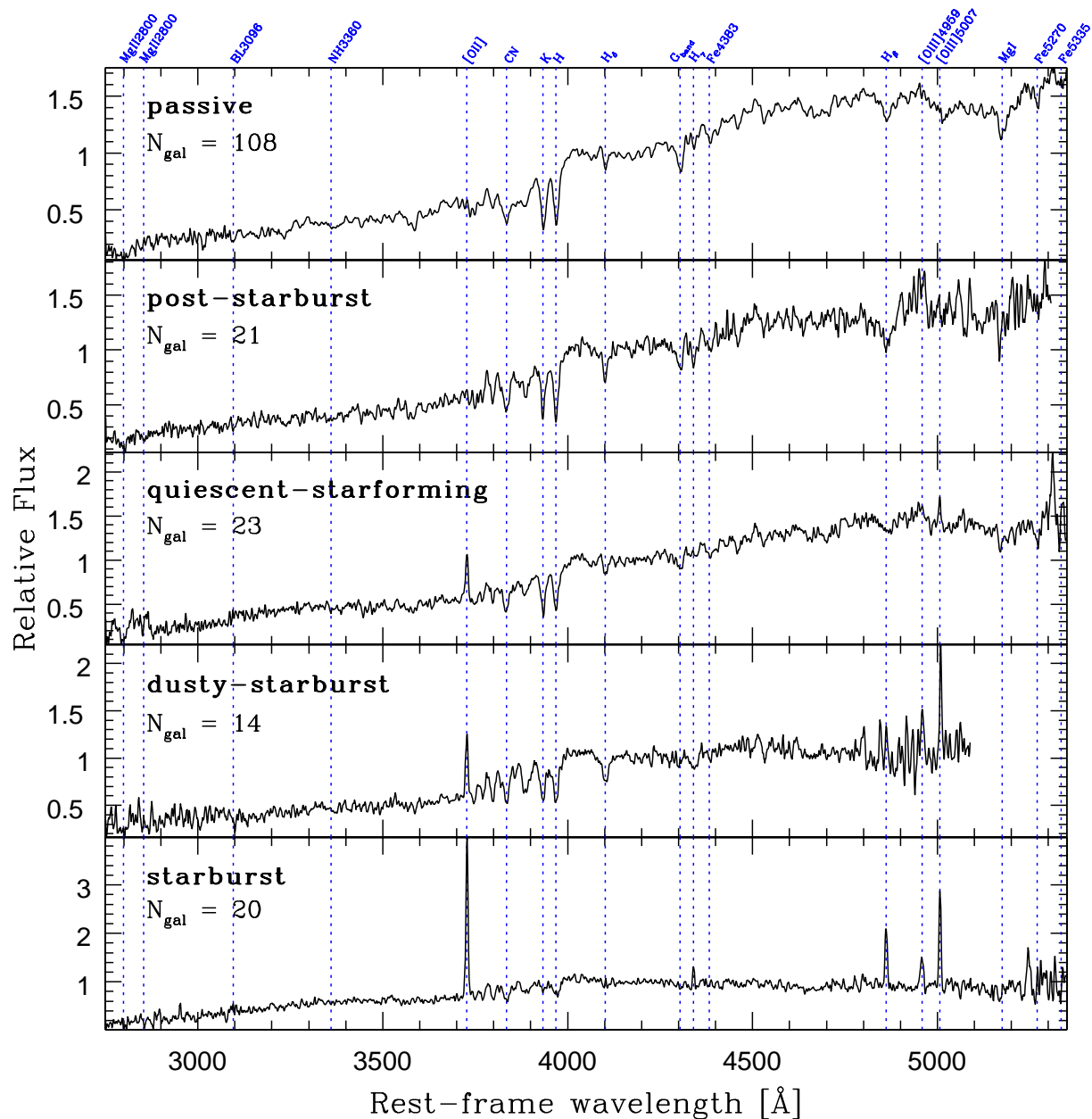


Figure 4.13: Final composite spectra, representative of the five considered spectral classes, created from a total of 186 galaxy spectra. The spectral classes and the number of stacked spectra are reported in the top left corner of each panel together with the expected position of the main spectral features marked by the blue vertical lines. A Gaussian smoothing filter of three pixels was applied.

Table 4.4: Spectral properties of the five averaged spectra of Fig. 4.13. The quoted five S/N refer to the wavelength range $4000\text{\AA} < \lambda < 4300\text{\AA}$.

Spectroscopic class	S/N	EW([OII]) [\AA]	EW(H δ_A) [\AA]	D _n 4000	EW(H β) [\AA]	EW([OIII] λ 5007) [\AA]
passive	9	1.431 \pm 1.191	0.148 \pm 0.981	1.810 \pm 0.030	1.829 \pm 0.606	0.958 \pm 0.611
post-starburst	6	-0.178 \pm 1.739	4.910 \pm 1.395	1.543 \pm 0.034	2.753 \pm 1.164	0.540 \pm 1.448
quiescent star-forming	7	-7.946 \pm 1.791	0.593 \pm 1.231	1.550 \pm 0.031	1.664 \pm 0.887	-1.184 \pm 0.985
dusty starburst	7.5	-7.719 \pm 1.605	5.827 \pm 1.123	1.412 \pm 0.030	-2.357 \pm 1.849	-5.842 \pm 0.693
starburst	5	-34.943 \pm 2.929	1.368 \pm 1.887	1.254 \pm 0.036	-8.816 \pm 1.797	-13.516 \pm 2.256

the relative spectral class and the number of galaxies used in the stacking process are reported in the top left corner. The most important spectral features recognizable in the rest-frame wavelength range $\Delta\lambda = 2700 - 5300 \text{ \AA}$ are labeled on the top side of the plot, and their expected positions are marked by dashed vertical lines. The spectral properties of the average spectra are quantified in Tab. 4.4 together with their S/N computed in the wavelength range $4000\text{\AA} < \lambda < 4300\text{\AA}$.

We note that the values of $\text{EW}(\text{H}\delta_A)$ and, especially, D_n4000 obtained for the “passive” template are similar to those observed for the most massive and passive galaxies in the local universe by SDSS-DR4 ($D4000_n|_{z=0} \approx 1.9$; $\text{EW}(\text{H}\delta_A)|_{z=0} \approx -1.5$) that were reported e.g. by Gallazzi et al. (2005).

In the next two sections (4.5.1 and 4.5.2) we compare the spectro-photometric properties of our composite spectra with those of galaxies residing in different redshift ranges and environments.

4.5.1 Comparison of the resulting passive template with previous library spectra

To highlight the original aspects of the spectroscopic library provided in this chapter and, hence, its uniqueness w.r.t. other previous similar works, we considered as an example the composite spectrum of our passive galaxies and qualitatively compared it with others representative of the same class of objects that reside in the local and distant universe and in different environments. Namely, we considered the distant sample of *early-type* galaxies in the field studied within the K20 survey, the composite spectrum of which has been provided by Mignoli et al. (2005). We highlight that the number of passive (stacked) spectra (93), their typical redshift values ($< z > \sim 1.0$, extended up to $z \sim 1.25$) and the spectro-photometric method used by the authors to identify their passive galaxies are very close to the numbers and criteria adopted in our work (see Sec. 4.4). As a second reference sample we considered the nearby passive template provided by Kinney et al. (1996), produced from a total of four morphologically selected bright ($M_B < -21$) elliptical galaxies residing in groups with $\langle z \rangle \sim 0.008$. Finally, we adopted the composite spectrum produced by Eisenstein et al. (2003) by using more than 1000 SDSS luminous red galaxies (LRG), selected in magnitude ($M_g < -21.8$) and in the redshift range $0.3 < z < 0.55$, as a third element of comparison.

All the above composite spectra, normalized in the wavelength range $3950\text{\AA} < \lambda < 4050\text{\AA}$ and smoothed with a three pixel boxcar filter, are plotted in the two panels of Fig. 4.14.

From this figure it appears that differences as well as similarities are present in

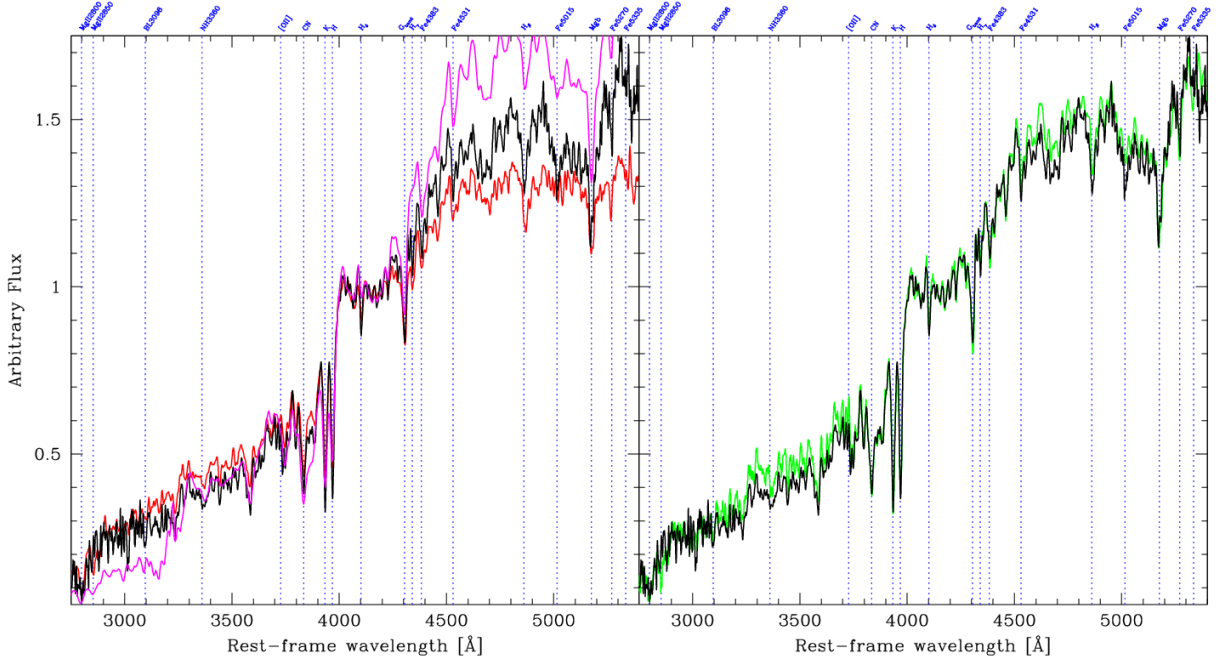


Figure 4.14: Qualitative comparison of our composite passive spectrum (black line) with the empirical templates quoted in the text that is representative of passive galaxies residing in different environments and redshift ranges. All spectra are normalized in the wavelength range $3950\text{\AA} < \lambda < 4050\text{\AA}$ and smoothed with a three pixel boxcar filter. *Left:* The K20 composite spectrum of distant early-type galaxies in the field is shown in red while the template computed by Kinney et al. (1996) for elliptical galaxies in groups at $z \sim 0.008$ is shown in magenta. It is evident that the passive galaxies of our sample are *redder* w.r.t. the K20 ones at similar redshift, but bluer than the ellipticals in groups in the local universe. *Right:* Comparison between the average spectrum of our passive galaxies and the LRG template provided by Eisenstein et al. (2003) (in green) that was computed for $z \sim 0.4$, $M_g < -21.8$ galaxies. Although the two spectra were obtained by using different galaxy selection criteria and redshift ranges, they appear to be remarkably similar overall (except for a slightly higher flux in U band for the LRG spectrum).

our composite spectrum of passive galaxies residing in high- z dense environments and the other empirical templates considered here. In particular, we observe the following:

1. The passive galaxies in the densest environments at $z \sim 1$ exhibit a mean rest-frame $U-V$ color that is redder than that of the coeval passive galaxies in K20, but bluer than that in groups at $z \sim 0$. Assuming that passive galaxies of the two distant samples span the same metallicity range, those in clusters seem to have evolved faster than their counterparts in the field. However, because passive galaxies in the XDCP are more luminous (massive) than those in K20, the difference in their mean rest-frame $U-V$ colors could be driven entirely by mass and not (also) by the density environment (cf. Thomas et al. 2005, 2010). A more detailed spectroscopic analysis of our entire galaxy sample, aimed to characterize its star formation history, is in progress, however, and will be extensively discussed in a forthcoming paper.
2. The spectroscopic similarities between LRG and our passive galaxies would analogously suggest for the former sample an evolutionary path strongly driven by their *mass* and likely characterized by different assembly histories.

In summary, we find significant differences of our passive composite spectrum compared to similar ones in dense low- z environments as well as high- z field environments. The closest resemblance of our passive spectrum is found to the LRG template, obtained at intermediate redshift for very massive elliptical and bulge-dominated galaxies. All these findings seem to point toward a scenario where the evolutionary path of the passive galaxies, also residing in clusters, is mainly driven by their mass rather than environment.

4.5.2 $U - B$ color of the templates

In this section we compute the $(U - B)$ rest-frame colors of the average spectra shown in Fig. 4.13 and compare them to those typical of nearby galaxy clusters. Specifically, we refer to the values observed for the Coma Cluster ($z = 0.024$) that were reported in the $(U - B)$ vs H color-magnitude relation (CMR) of Fig. 3 in Eisenhardt et al. (2007).

Firstly, we obtained the $(U - B)$ rest-frame color $[(U - B)_{rest}]$ for each spectroscopic class by convolving the corresponding rest-frame spectrum with the response curves of the U and B filters of the KPNO 0.9m telescope. We also computed the quoted *observed* color by redshifting the average spectra to $z = 0.024$ $[(U - B)_{z=0.02}]$

Table 4.5: $(U - B)$ colors of the five spectral templates at rest-frame and $z = 0.024$ (second and third column, respectively). For each class the differences between its $(U - B)_{rest}$ color and the corresponding value of a passive galaxy is reported in the fourth column.

Spectroscopic Class	$(U - B)_{rest}$	$(U - B)_{z=0.02}$	$\Delta(U - B)_{rest passive}$
passive	0.553	0.566	0.000
post-starburst	0.409	0.455	-0.144
quiescent star-forming	0.413	0.432	-0.140
dusty starburst	0.229	0.301	-0.324
starburst	-0.027	0.041	-0.580

to obtain quantities comparable with Coma. These values are reported in the second and third column of Tab. 4.5, together with the differences between each rest-frame color and that typical of the passive class, taken as reference [$\Delta(U - B)_{rest|passive}$, fourth column].

After computing the five $(U - B)_{z=0.02}$ colors, we associated a median observed Vega H-magnitude ($\langle H_{obs} \rangle$) to each spectroscopic class to then plot these values in a color-magnitude diagram. We defined $\langle H_{obs} \rangle$ for each class as the median value of the apparent H-mag of the galaxies belonging to the class itself. However, only 13 out of the 16 XDCP clusters listed in Tab. 4.2 were observed in H-band, providing a total of 133 galaxies usable to this aim. The number of the galaxies with H-band data for each class, their median redshift and H_{obs} are provided in Tab. 4.6. Finally, to compare the computed values with those of Coma galaxies in a consistent way, we rescaled all observed H magnitudes to a characteristic $m_H^*(z)$. It is defined as the apparent H magnitude of a galaxy at redshift z that has $L = L^*$ at $z = 0$, passively evolving since $z_{form} = 5$. We adopted a suite of spectral energy distribution models⁵, corresponding to the evolution of a simple stellar population, computed within the framework of PEGASE 2 (Fioc & Rocca-Volmerange 1997). The stellar mass-scale

⁵In particular, these models assume a Salpeter (1955) stellar initial mass function with lower and upper mass cut-offs equal to 0.1 and 120 M_\odot , fixed solar metallicity and a range of 130 epochs with a time step of 0.1 Gyr since the instantaneous burst of formation. This choice provides a suitable representation of the optical/near-infrared colors of observed, red, and dead galaxies associated with old, passively evolving stellar populations and an elliptical morphology in different density environments up to $z \sim 2$ (e.g., Pierini et al. 2004; Wilman et al. 2008; Fassbender et al. 2011a).

Table 4.6: The median apparent Vega H-magnitude (column 4) together with the number of used galaxies and their median redshift (column 2 and 3, respectively) for each spectral class. In column 5 the median of the difference between H_{obs} and the apparent H magnitude of a L^* galaxy (at $z = 0$) passively evolving since $z_{form} = 5$ is reported. The error refer to the semi-interquartile range.

Spectroscopic Class	N_{gal}	$\langle z \rangle$	$\langle H_{obs} \rangle$	$\langle H_{obs} - m_H^* \rangle$
passive	80	0.94 ± 0.07	18.49 ± 0.46	-0.30 ± 0.47
post-starburst	11	1.07 ± 0.12	19.19 ± 0.26	-0.10 ± 0.35
quiescent star-forming	14	0.96 ± 0.02	19.52 ± 0.39	0.18 ± 0.44
dusty starburst	18	0.83 ± 0.11	18.71 ± 0.61	0.14 ± 0.39
starburst	10	0.97 ± 0.14	19.48 ± 0.55	0.63 ± 0.89

is matched to the observed magnitude of an L^* galaxy in clusters at $z \sim 0$ in the Ks-band (Strazzullo et al. 2006). The association between age of the model and redshift of the observed galaxy is set by the adopted cosmological model.

Since m_H^* is a function of redshift, the appropriate value was computed and subtracted from H_{obs} for each galaxy according to its redshift. The median $\langle H_{obs} - m_H^* \rangle$ was finally obtained for each spectral class and is quoted in the fourth column of Tab. 4.6. The apparent H magnitudes of Coma galaxies were equivalently rescaled by referring to $m_{H,Coma}^* = 11.13$ as quoted by Eisenhardt et al. (2007) and found by de Propris et al. (1998).

The final $(U - B)_{z=0.02}$ vs $H_{obs} - m_H^*$ CMR for Coma and the average spectra of distant cluster members is shown in Fig. 4.15.

From Fig. 4.15 it is clear how the $(U - B)$ colors of the Coma early-type galaxies are fully consistent with the typical $(U - B)$ colors of the $0.6 \leq z \leq 1.2$ cluster members classified as passive, post-starburst, and quiescent star-forming from our analysis. This result may indicate that the stellar mass formation of the local passive cluster galaxies was almost completed already at $z > 0.8$, so that they did not experience any additional subsequent significant star formation process that could have made them bluer at $z \sim 0$. This appears to be confirmed because the values of $EW(H\delta_A)$ and D_n4000 (reported in Tab. 4.4) of the composite spectrum of distant passive galaxies are similar to those found for the passive and most massive galaxies in the local universe. These findings suggest that these galaxies have created the bulk of their stellar mass already at $z > 0.8$ and, according to the results discussed in Sec. 4.5.1, possibly even faster than the coeval galaxies in the field. As mentioned

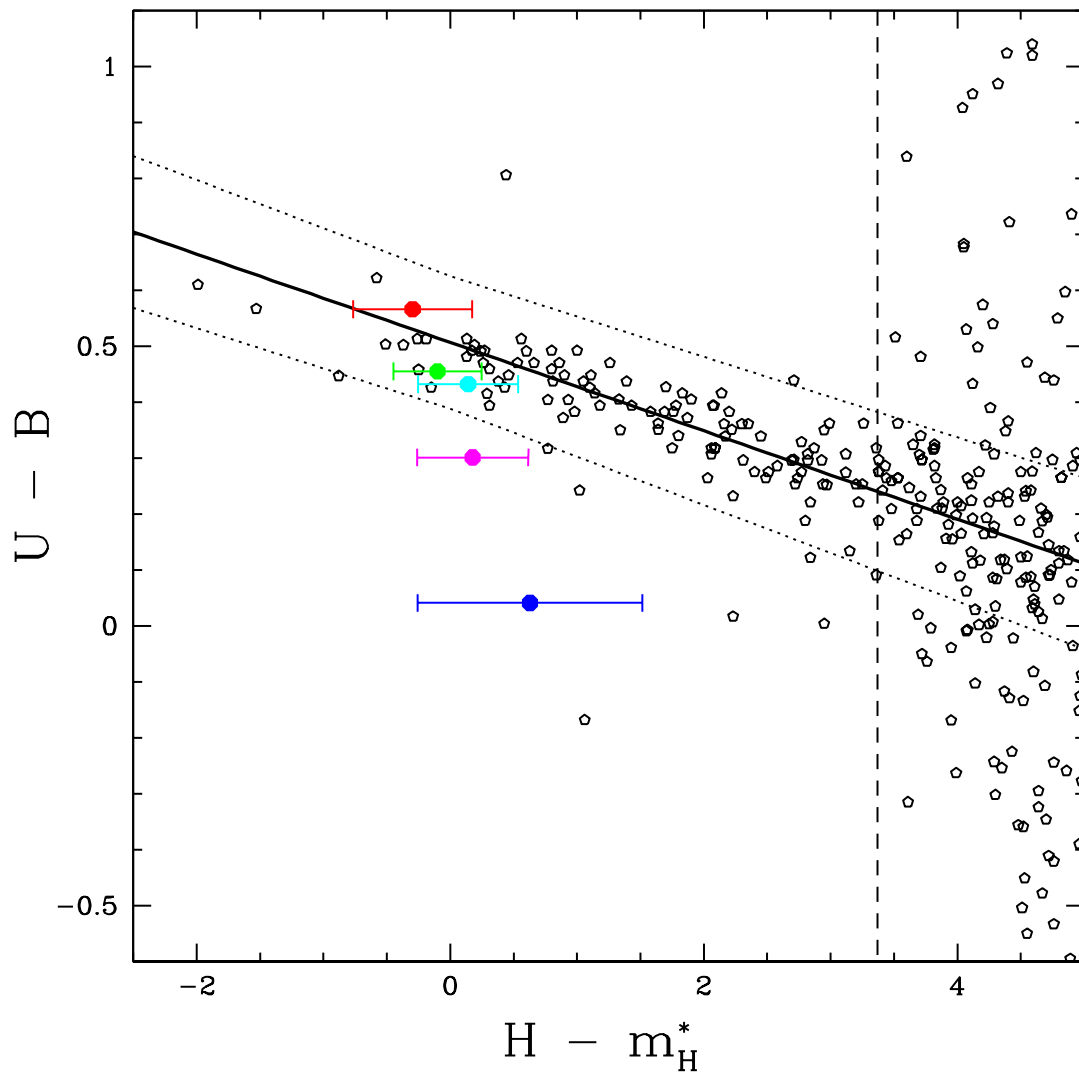


Figure 4.15: CMR of Coma Cluster galaxies (black pentagons) and the red sequence best fit, computed only for the early-type galaxies defined as brighter than $H = 14.5$ (at the left of the dashed vertical line), with relative scatter (black dotted lines) as provided by Eisenhardt et al. (2007). The overplotted colored points mark the values obtained for the average spectra representative of the high- z cluster members, with the same color code as defined in Fig. 4.9. Note that for a consistent comparison all the observed H-band magnitudes were rescaled to the corresponding m_H^* values, as explained in the text. For Coma galaxies a value of $m_{H,Coma}^* = 11.13$ was used.

in Sec. 4.5.1, another study on the age-metallicity relation of the passive galaxies contained in our sample is currently underway and will be extensively discussed in a forthcoming paper.

Finally, Fig. 4.15 also shows that the starburst galaxies at $z \leq 0.6$ appear to be more luminous (in H-band) than the Coma galaxies with the same color. Even though a large part of this effect may be due to the expected selection bias toward the brightest objects in the distant universe, that in Coma very few star-forming objects appear to have $H \sim m_{H,Coma}^*$ is a consequence of the *downsizing* scenario according to which the most vigorous star-formation activity at high redshift was actually located in the most massive galaxies (e.g., Cowie et al. 1996; Gavazzi & Scodeggio 1996; Gavazzi et al. 1996; Juneau et al. 2005; Pannella et al. 2009). This effect is also believed to have played a fundamental role in building-up the red sequence in galaxy clusters starting from the more massive galaxies (see e.g., Romeo et al. 2008).

4.6 Summary and conclusion

We presented *F*-VIPGI, a new adapted version of VIPGI for reducing FORS2 spectroscopic data in a semi-automated and efficient way. We discussed the major improvements and technical aspects of the new software, which is now available to the scientific community, in the first part of the chapter. Additional information on the presented software are provided in Appendix A.

In the second part we showed an application of the above pipeline to a sample of distant ($0.65 \leq z \leq 1.25$) X-ray selected galaxy clusters as part of the XDCP sample. We classified all galaxies according to their spectral indices $EW([OII])$ and $EW(H\delta)$ and stacked their spectra to create a new library of templates, which is particularly suited for a better redshift (spectroscopic and photometric) measurements of galaxies residing in dense high- z environments.

In the last part of the chapter we compared the composite passive spectrum with others representative of the passive galaxy populations residing in different environments and cosmic epochs, finding some remarkable differences and similarities among them. Namely, we found that passive galaxies in clusters appear to be more evolved already at $z \sim 0.8$ w.r.t. the field galaxies at similar redshift, supporting the idea that galaxy evolution is significantly accelerated in the densest environments. However, because our sample is significantly biased toward higher masses, we cannot exclude the importance of the *mass* as another driving element of evolution either. We finally studied the $(U - B)$ colors of the entire sample of composite spectra and compared them to those observed in the Coma Cluster. The results of this work show that the colors of the passive galaxies in local clusters are fully consistent

with those observed for distant cluster members classified as passive, post-starburst, and quiescent star-forming according to our criteria. This suggests that the stellar mass formation in local cluster galaxies was almost completed already at $z \sim 0.8$. In addition, comparing the mean H-band luminosities of the bluest galaxies of our sample with those in Coma, we found that at $z \geq 0.65$ the star-forming galaxies are much more luminous. Beyond the expected selection bias, the observed effect may be partly explained by assuming a *downsizing* scenario, where the most vigorous star-forming galaxies in the far universe were also the most massive ones.

Chapter 5

The galaxy cluster XMMU J0338.8+0021 at $z = 1.49$

Abstract. This chapter refers to the work of Nastasi et al. (2011), *A&A*, **532**, L6. We report the discovery of a galaxy cluster at $z = 1.490$, originally selected as an extended X-ray source in the XMM-*Newton* Distant Cluster Project. Further observations carried out with the VLT-FORS2 spectrograph allowed the spectroscopic confirmation of seven secure cluster members, providing a median system redshift of $z = 1.490 \pm 0.009$. The color-magnitude diagram of XMMU J0338.8+0021 reveals the presence of a well-populated red sequence with $z-H \approx 3$, albeit with an apparent significant scatter in color. Since we do not detect indications of any strong star formation activity in these objects, the color spread could represent the different stellar ages of the member galaxies. In addition, we found the brightest cluster galaxy in a very active dynamical state, with an interacting, merging companion located at a physical projected distance of $d \approx 20\text{kpc}$. From the X-ray luminosity, we estimate a cluster mass of $M_{200} \sim 1.2 \times 10^{14} M_{\odot}$. The data appear to be consistent with a scenario in which XMMU J0338.8+0021 is a young system, possibly caught in a moment of active ongoing mass assembly.

5.1 Introduction

The search for distant ($z > 0.8$) galaxy clusters has received a remarkable boost recently. By means of various selection methods, several clusters have been found in the *redshift desert*, at $z \geq 1.5$. Papovich et al. (2010) and Tanaka et al. (2010) independently reported the detection of a new IRAC selected cluster at $z = 1.62$, characterized by a well-populated and tight red sequence. An additional multi-band

analysis has revealed that the star formation activity in this cluster increases with the environment density, with star forming galaxies being mainly located at the center of the system (Tran et al. 2010). A similar trend has been observed in three other X-ray selected galaxy clusters, two newly confirmed at $z = 1.56$ (Fassbender et al. 2011c) and $z = 1.58$ (Santos et al. 2011) and one at $z = 1.46$ (Hilton et al. 2009, 2010). However, the galaxy red-sequence of these systems has not yet been fully established yet, indicating that the members are still building their stellar mass via star formation activity. The situation is different in clusters found so far at $z < 1.4$, where active star-forming galaxies preferentially reside in the cluster outskirts (e.g. Balogh et al. 2004; Lidman et al. 2008; Patel et al. 2009). However, it is expected that more distant galaxy clusters contain a larger number of star-forming galaxies in their central regions (e.g. Hopkins et al. 2008; Rettura et al. 2010). In addition, early-type galaxies (ETGs) in clusters are known to have completed the formation of their stellar populations much more rapidly than ETGs in the field, and the red sequence is expected to start to disappear at $z \approx 2$ toward higher redshift (Gobat et al. 2008). This last prediction is consistent with the results of Gobat et al. (2011), where the discovery of the most distant cluster known to date, at $z = 2.07$, is reported. In this system, the population of passive galaxies displays a very large intrinsic scatter in the $Y - K_s$ color, with an apparent absence of an established red sequence. This suggests that as we acquire observations of increasingly high redshift, we are approaching the early stages of galaxy formation in the densest environments. All these new findings highlight the importance of detecting new distant galaxy clusters for a systematic investigation of the processes that drive galaxy evolution in different environments.

In this chapter, we report the discovery of an X-ray selected, spectroscopically confirmed galaxy cluster at $z=1.490$, found within the XMM-*Newton* Distant Cluster Project. We first present the X-ray data (Sect. 5.2.1) followed by a discussion of the near-infrared (NIR) imaging observations (Sect. 5.2.2) and the optical spectroscopy results (Sect. 5.3). In Sect. 5.4, we discuss the dynamical state of the system and its galaxy population. Summary and conclusions are given in Sect. 5.5. For this section, we assume a concordance Λ CDM cosmology, with $(H_0, \Omega_\Lambda, \Omega_m, w) = (70 \text{ km s}^{-1} \text{ Mpc}^{-1}, 0.7, 0.3, -1)$. For the given cluster redshift, the angular scale is $8.46 \text{ kpc}''$. Magnitudes are in the Vega system.

5.2 Observations, data analysis, and results

The cluster XMMU J0338.8+0021 (hereafter X0338) was discovered within the XMM-*Newton* Distant Cluster Project (XDCP), a serendipitous archival X-ray survey focussed on the identification of X-ray luminous systems at $z > 0.8$ (e.g. Mullis et al.

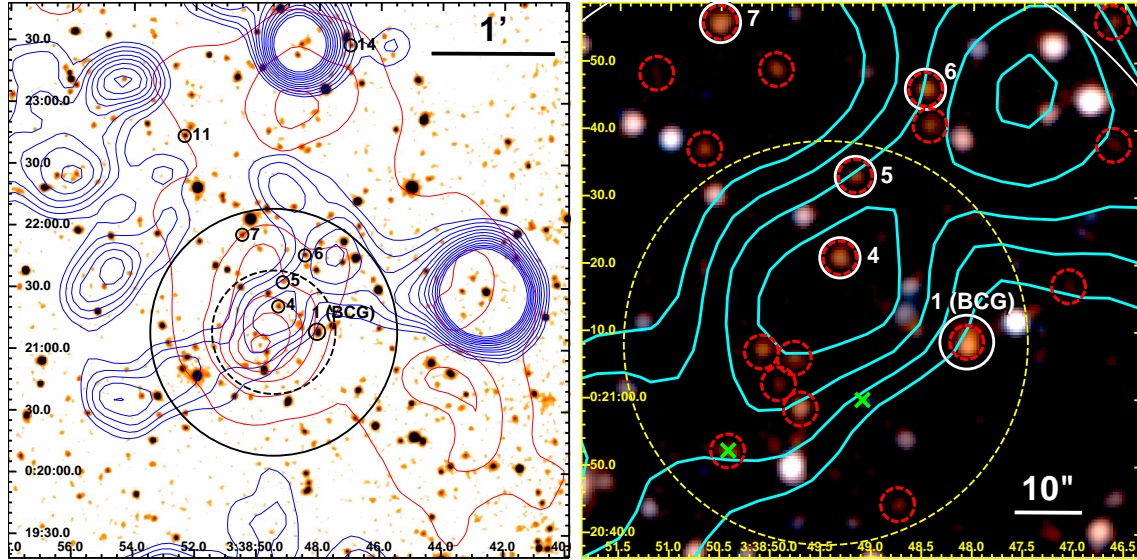


Figure 5.1: *Left:* H-band image ($4.5'$ side length) of the environment of XMMU J0338.8+0021 at $z = 1.490$. The XMM-Newton detected X-ray emission is shown by the log-spaced blue contours, with the four lowest ones corresponding to significance levels of 2, 2.7, 3.6, 4.6σ above the mean background. The associated overdensity of color-selected red galaxies is displayed by the red contours, showing linearly spaced significance levels of $2\text{--}20\sigma$. The large, black circles indicate the $0.5'/1'$ radii around the X-ray center; the small black ones mark the spectroscopically confirmed cluster members, with the corresponding IDs. The image was smoothed with a 3 pixel ($1.3''$) Gaussian kernel. *Right:* z +H-band color composite image of the core region of the cluster. X-ray contours are displayed in cyan, red galaxies with $2.6 \leq z-H \leq 3.5$ are marked by red dashed circles, spectroscopic members by white circles and interlopers (i.e. spectroscopically confirmed non-members) by green crosses. The $30''$ radius from the X-ray center is indicated by the yellow circle. The white ruler represents the beam size (FWHM) of XMM-Newton at the observed off-axis angle of $\sim 5.6'$.

2005; Böhringer et al. 2005; Fassbender 2007; Fassbender et al. 2011a).

5.2.1 X-ray selection with XMM-*Newton*

The X-ray source associated with the cluster X0338 was initially observed in 2002, in the XMM-*Newton* field with observation identification number (OBSID) 0036540101 and a nominal exposure time of 22.9 ksec. It was detected as a weak source with SAS v6.5 at an off-axis angle of $5.6'$, with a source significance of about 5σ and an extent significance of about 2.5σ . We reprocessed the field with SAS CMDv10.0 and, after applying a strict two-step flare-cleaning process, a clean net exposure time of 16.4/15.9 ksec remained for the two EMOS cameras and 7.8 ksec for the PN instrument. Figure 5.1 shows log-spaced X-ray contours (blue/cyan) of the cluster environment with significance levels of $2\text{--}16\sigma$. For the flux measurement, we applied the growth curve analysis (GCA) method of Böhringer et al. (2000) in the soft 0.5–2 keV band and measured $f_{X,500} \simeq (3.0 \pm 1.8) \times 10^{-15} \text{ erg s}^{-1} \text{ cm}^{-2}$ in a $40''$ ($\simeq R_{500}$) aperture. At the cluster redshift, this translates into a 0.5–2 keV X-ray luminosity of $L_{X,500} \simeq (4.1 \pm 2.4) \times 10^{43} \text{ erg/s}$. Owing to the faintness of the source at the limit of detectability, with ~ 33 net counts within an aperture of $24''$, the determination of additional structural or spectral parameters is currently unfeasible and the extended nature of the source is tentative. However, based on the $M\text{--}L_X$ scaling relation in Pratt et al. (2009), with a modified redshift evolution (Fassbender et al. (2011c); Reichert et al. (2011)), a first rough estimate of the expected temperature (T_X^{est}) and mass (M_{500}) can be obtained, with $T_X^{est} \sim 2.5 \text{ keV}$ and $M_{500} \sim 0.8 \times 10^{14} M_\odot$, corresponding to a total mass estimate of $M_{200} \sim 1.2 \times 10^{14} M_\odot$ under the assumption of a NFW profile. According to the above T_X^{est} value, a bolometric luminosity $L_{X,500}^{bol} \simeq (1.1 \pm 0.6) \times 10^{44} \text{ erg/s}$ is finally estimated. We cannot rule out that part of the X-ray flux is due to contaminating point sources and, thus, the reported luminosities have to be taken as upper limits. All the estimated X-ray quantities are reported in Table 5.1.

5.2.2 Near-infrared follow-up imaging

X0338 was photometrically confirmed as a significant overdensity of very red galaxies coinciding with its X-ray detection position, using the wide-field ($15.4' \times 15.4'$) near-infrared (NIR) camera OMEGA2000 at the Calar Alto 3.5m telescope. We obtained medium-deep H-band (50 min) and z-band (53 min) images of the X0338 field in 2006 under good, but non-photometric, conditions with a seeing of $1.2''$. Re-observations with the z-filter were performed (5 min) in photometric conditions for the target and

Table 5.1: Main properties of XMMU J0338.8+0021

RA	03:38:49.5
DEC	+00:21:08.1
z	1.490 ± 0.009
$f_X(0.5 - 2keV)$	$(3.0 \pm 1.8) \times 10^{-14} \text{ erg s}^{-1} \text{ cm}^{-2}$
$L_X(0.5 - 2keV)$	$(4.1 \pm 2.4) \times 10^{43} \text{ erg s}^{-1}$
L_X^{bol}	$(1.1 \pm 0.6) \times 10^{44} \text{ erg s}^{-1}$
$M_{X,200}$	$\sim 1.2 \times 10^{14} M_\odot$
R_{200}	$\sim 590 \text{ kpc}$
T_X^{est}	$\sim 2.5 \text{ keV}$

designated SDSS standard stars (Smith et al. 2002) for photometric calibration. The data were reduced with a designated OMEGA2000 NIR pipeline (Fassbender 2007). The **SExtractor** (Bertin & Arnouts 1996) photometry was calibrated to the Vega system using 2MASS point sources (Cutri et al. 2003) in H and SDSS standard stars in z. The limiting (Vega) magnitudes (50% completeness) were determined to be $H_{\text{lim}} \sim 21.2$ and $z_{\text{lim}} \sim 23.1$, corresponding to absolute magnitudes of $M^* + 1.3$ in H and M^* in z for passively evolving galaxies at $z \sim 1.5$. Figure 5.1 (left) shows an H-band image of the cluster field with overlaid X-ray contours (blue), density contours of color selected galaxies with $2.6 \leq z - H \leq 3.5$ (red), and marked spectroscopic cluster members as black circles. A zoom onto the core region is shown in Fig. 5.1, right. The z-H versus H color-magnitude diagram (CMD) of the field is shown in Fig. 5.2.

5.3 Spectroscopic analysis

5.3.1 Data reduction

X0338 was observed with FORS2-VLT on December 2009 (program ID:84.A-0844) with seeing conditions between $0.7''$ and $1.1''$. A single MXU slit-mask (field of view $6.8' \times 6.8'$) with a total of 42 $1''$ width slits was used. The chosen instrument setup (300I grism without blocking filter) provides a wavelength coverage of $5800 - 10500 \text{ \AA}$, with a resolution of $R = 660$. The total net integration time was 8.4ks. Raw data were

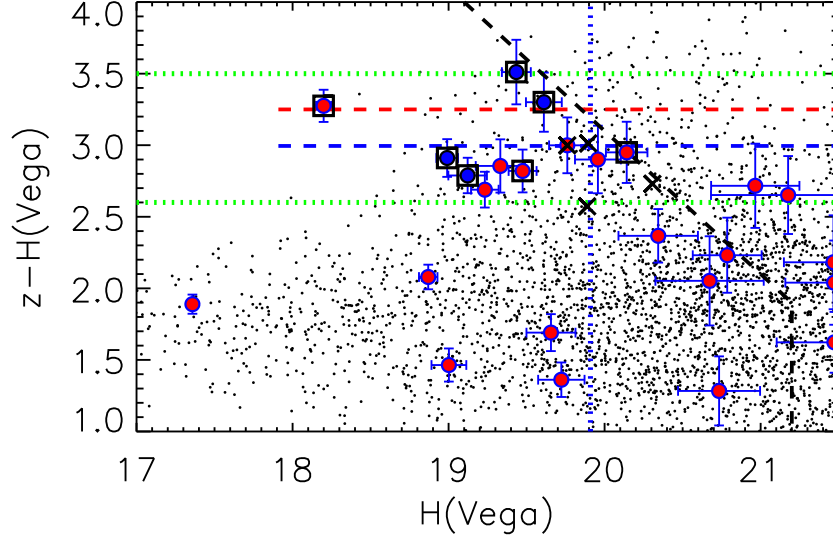


Figure 5.2: Color-magnitude diagram of the cluster field. All galaxies with $D_{proj} \leq 30''$ are displayed in red. The seven secure spectroscopic cluster members are marked by black squares (with blue dots for $D_{proj} > 30''$) and are all located within a color range $2.6 \leq z-H \leq 3.5$ (green dotted lines), with an average color of $z-H \sim 3$. The interlopers found in the above color cut are marked by black crosses. Two simple stellar population (SSP) models for the cluster redshift are overplotted at $z-H \sim 3$, with solar metallicity and formation redshift of $z_f = 5$ (red dashed line) or $z_f = 3$ (blue dashed). The vertical dotted blue line indicates the apparent magnitude of an L^* galaxy at $z = 1.49$, black dashed lines show the 50%-completeness limit.

reduced with a new FORS2 adaption of the *VIMOS Interactive Pipeline Graphical Interface* (VIPGI, Scodreggio et al. (2005)), which includes all the standard reduction and wavelength calibration steps (Nastasi et al., in prep.). A total of 45 spectra were extracted, with a final calibration uncertainty of $\sim 1\text{\AA}$.

5.3.2 Redshift measurements

For the redshifts assessment, we firstly used the graphical VIPGI tools for a quick visual inspection and, then, the EZ software (Garilli et al. 2010) with a set of different galaxy spectra templates. The analysis confirmed the existence of seven galaxies in the redshift range $1.473 \leq z \leq 1.503$ (Fig. 5.3), six of which have a projected distance from the X-ray emission peak of $D_{proj} < 2'$ and rest-frame velocity offsets of $|\Delta v| < 2000$ km/s with respect to the median redshift. This allows us to confirm

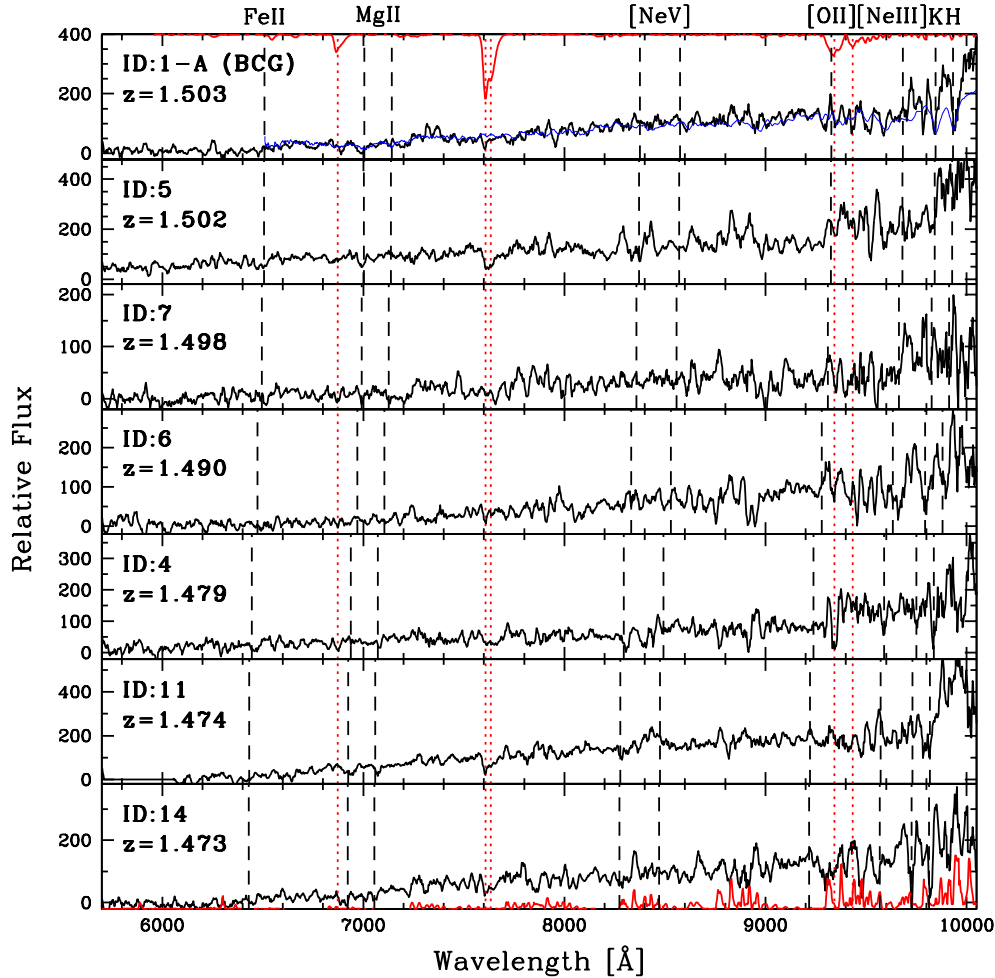


Figure 5.3: One-dimensional spectra of the seven confirmed members of XMMU J0338.8+0021, smoothed with a 7 pixel boxcar filter. For each spectrum, an identification label (ID) and the measured redshift is reported. For the brightest component of the BCG (ID:1-A), the same LRG spectrum template used in Fig.5.4 is overlaid in blue for comparison. In red, the sky features in absorption (top) and emission (bottom) are shown. The position of the main spectral features, shifted according to the corresponding redshift values, are marked by the vertical dashed lines.

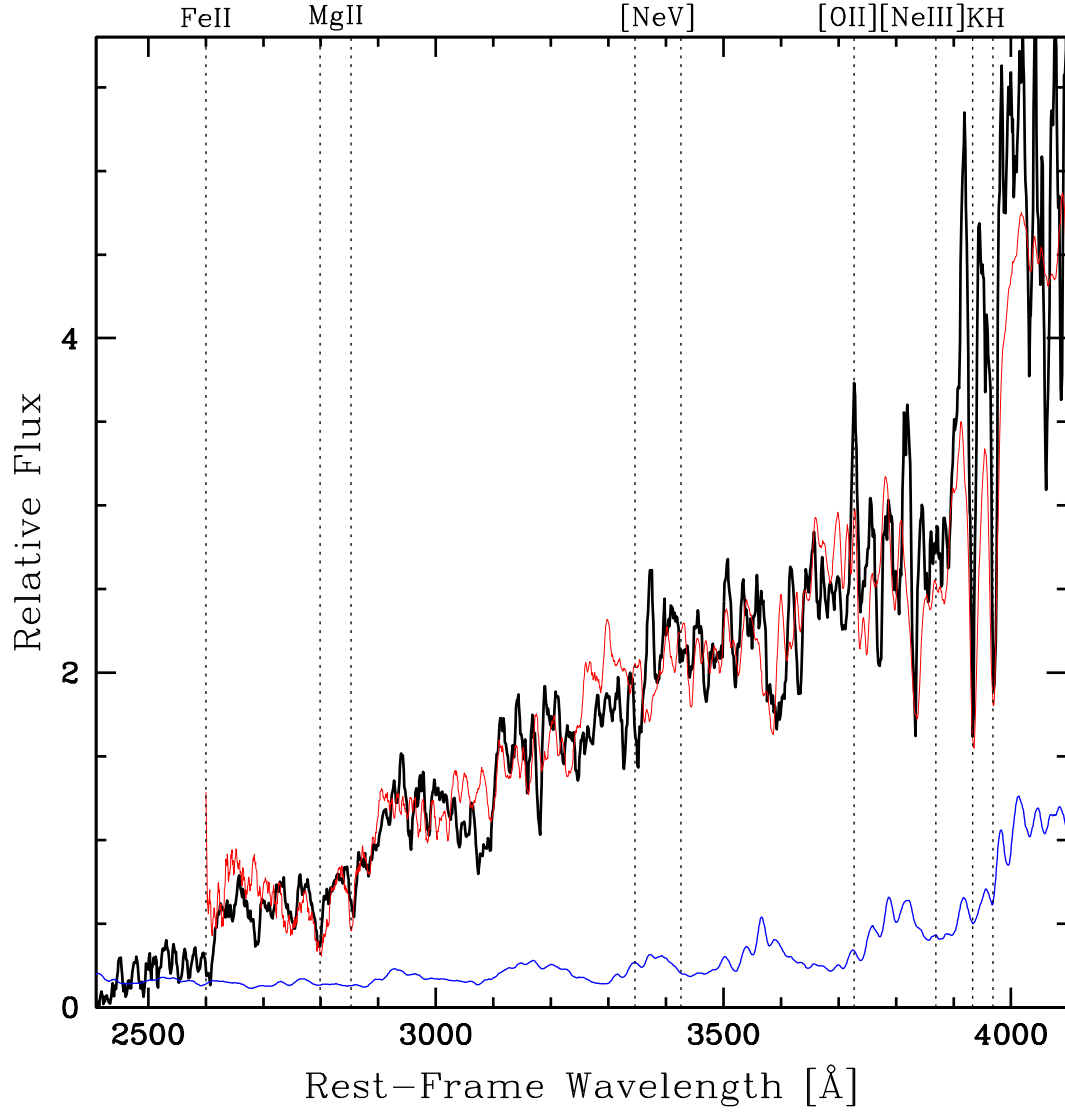


Figure 5.4: Composite rest-frame spectrum of the seven member galaxies. The main features are marked by dotted lines and the total noise spectrum is shown in blue. An LRG template based on $z \sim 0.5$ luminous red galaxies (Eisenstein et al. 2003) is overplotted in red to show the good match with the low- z template. The spectrum is smoothed with a 7-pixel boxcar filter.

the presence of a bound system of, at least, 7 galaxies with a median redshift of $z = 1.490 \pm 0.009$. Using the biweight estimator (Beers et al. 1990), we obtain a crude velocity dispersion estimate of $\sigma_v \approx 670$ km/s in the cluster rest frame, albeit with an associated large uncertainty owing to the poor quality of the statistics. The extracted spectra and the main properties of the confirmed members are shown in Fig. 5.3 and reported in Table 5.5, respectively. Several spectral features are identifiable, despite strong emission and absorption sky lines affecting the quality of the individual spectra. For the BCG, we extracted the spectra of both components ID:1-A and ID:1-B (Fig. 5.5, *right*), which are distinguishable in the $0.86''$ seeing z -band preimage of the left panel of Fig. 5.5. For ID:1-B, only a tentative redshift measurement of $z = 1.5001$ can be obtained owing to its low signal-to-noise ratio.

To enhance the faintest features, an average, noise-weighted, spectrum of the seven members was created. The result is shown in Fig. 5.4 and compared with an LRG template spectrum (in red) typical of $z \sim 0.5$ luminous red galaxies (Eisenstein et al. 2003).

5.4 A young cluster in formation?

From the CMD in Fig. 5.2, we note that the red sequence of X0338 appears well populated. The eleven red galaxies, with colors $2.6 \leq z-H \leq 3.5$ and brighter than the completeness limit, have a median (average) color of $z-H = 2.9$ mag (3.0 mag), which is consistent with the model prediction of $z-H \simeq 3.0$ mag for a stellar formation redshift of $z_f = 3$, which represents an evolved red-sequence population, as seen in other distant clusters (XMMUJ1229, Santos et al. (2009); XMMUJ2235, Strazzullo et al. (2010)). From the observed color spread of $\delta_{z-H}^{obs} \approx 0.25$ mag, with an assumed flat slope and a Monte Carlo estimated contribution of the photometric errors of (0.16 ± 0.04) mag, we obtain a first order estimate of the intrinsic red-sequence scatter of $\delta_{z-H}^{int} \sim (0.19 \pm 0.04)$ mag. This is significantly larger than in the above cases, e.g. 0.08 for XMMUJ2235, but consistent with the findings of Hilton et al. (2009) for their $z = 1.46$ cluster. The estimated intrinsic scatter does not change if a non-flat slope (e.g. the one of XMMUJ2235 given by Strazzullo et al. (2010)) for the fit is used. This larger scatter can be explained by stellar formation-age differences of the bright end of the red galaxy population of the order of 0.5-1 Gyr, as discussed in Hilton et al. (2009). The seven spectroscopic members show weak or no signs of ongoing star formation activity, with a measured equivalent width of the [OII] line in their spectra of $|EW_{[OII]}| \leq 5 \text{ \AA}$. Assuming that the above spectral features

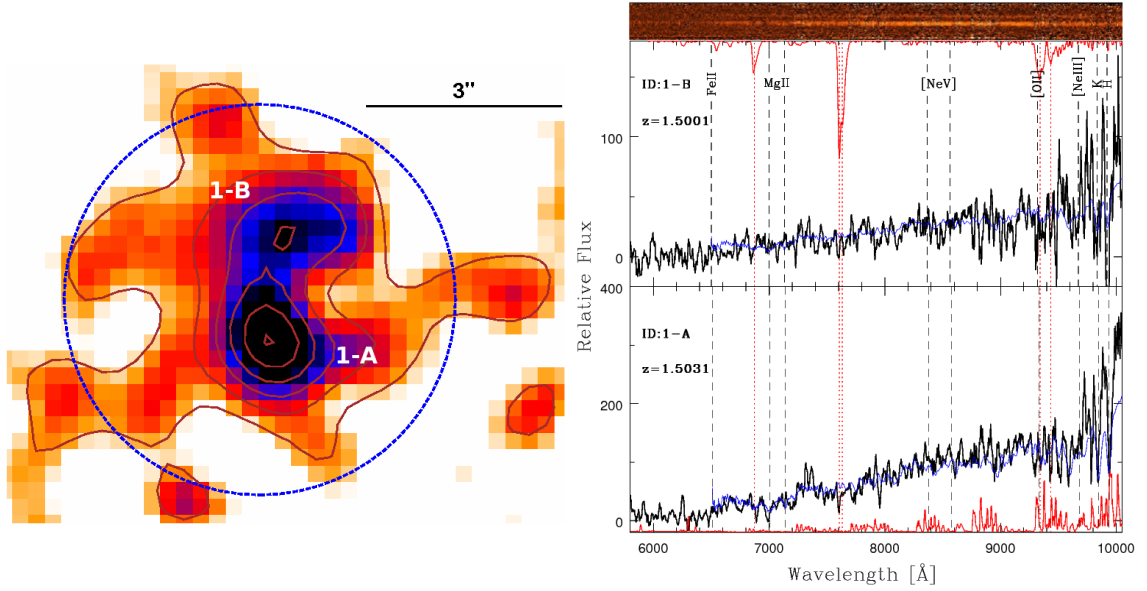


Figure 5.5: **Left:** Close-up z -band image of the BCG of XMMU J0338.8+0021, smoothed with a 0.7 arcsec Gaussian filter. The contours indicate the linearly spaced isophotes of the image cutout and the blue circle refers to an area of 3'' radius. The presence of a double-core system is clearly visible, indicating that the brightest galaxy is experiencing an ongoing assembly process. **Right:** Two-dimensional reduced spectra (*top*) and the one-dimensional extracted ones (*bottom*) for the two BCG components (ID: 1-A, 1-B). In the bottom panel, the ID number and the measured redshift for each spectrum is reported in the top left corner, and the corresponding best-fit LRG template is overlaid in blue. Because of the low signal-to-noise ratio of the data obtained for ID:1-B (whose spectrum is barely distinguishable in the top panel), its redshift value is only tentative. Both spectra have been smoothed with a 7 pixel boxcar filter.

is a proxy of their star formation rate¹, the measured values for $EW_{[OII]}$ indicate a very moderate intensity for such activity. The existence of a real, albeit weak, [OII] emission activity in the X0338 members is confirmed by the presence of such a spectral feature in the composite spectrum of Fig. 5.4. On the red sequence, we find a magnitude gap between the BCG and the second ranked member of $\Delta m_{12} \approx 0.8$ mag. From the study of Smith et al. (2010) in the local universe, this indicates that the cluster is dynamically evolved, while the apparent offset of the BCG from the center of the X-ray emission ($D_{proj}^{BCG} \approx 175$ kpc) is a typical sign of a dynamically young clusters (Haarsma et al. 2010). This is in line with the cluster displaying indications of asymmetric X-ray emission with a low central surface brightness. A close-up study of the BCG, shown in Fig. 5.5 (*left*), reveals a double-object morphology which indicates that the galaxy is actively assembling its mass after a merger event (implying that the aforementioned relatively large magnitude gap is a very recent feature). Because of the lack of detectable emission lines in ID:1-A and 1-B spectra, we conclude that this coalescence is likely to be a dry merger. The overall color and magnitude of the BCG are consistent with the ones found in red, passive, brightest galaxies residing in low-redshift clusters. The case of X0338 seems to suggest that we may be finally witnessing the active mass assembly epoch of BCGs, in contrast to the evolved counterparts observed at $z \lesssim 1.4$ (e.g. Whiley et al. 2008; Collins et al. 2009). Such observations are consistent with a hierarchical assembly scenario for BCGs, albeit at a significantly earlier epoch than predicted from the cosmological simulation results of De Lucia & Blaizot (2007). The large scatter in the red sequence, the X-ray morphology, and the spatial distribution of color-selected red galaxies imply that this cluster is younger than e.g. XMMUJ2235, a scenario that will be critically tested by future deeper observations.

5.5 Summary and conclusion

We summarize the results of this chapter as follows:

- we have reported the study of a newly discovered galaxy cluster XMMU J0338.8+0021 at $z = 1.490$. This system was selected as an extended X-ray source serendipitously detected within the XDCP.
- Spectroscopic follow-up has allowed us to confirm seven cluster members, six

¹The presence of the [NeIII] λ 3870 line for the ID:11 galaxy, however, suggests that it contains an obscured AGN.

of which have $D_{proj} < 1$ Mpc and a rest-frame velocity offset $|\Delta v| < 2000$ km/s from the median redshift.

- The H+z band data reveal the presence of a well-populated, albeit quite broadly spread, red sequence in the CMD, with a median color of $z-H = 2.9$ mag and an intrinsic color scatter of $\delta_{z-H}^{intr} \sim 0.19$. Comparisons with SSP models suggest that the stellar populations of red sequence galaxies span formation epochs in the redshift range $3 \lesssim z_f \lesssim 5$.
- A BCG is clearly identifiable and found to be in an active mass assembly phase, likely via a dry merging process.
- Data overall suggest that X0338 is a young galaxy cluster that has not yet fully evolved, as the faint X-ray emission appears to be morphologically disturbed, and the large area over which its galaxies are found possibly indicates that these reside in infalling structures.

Our present interpretation is that X0338 has both features of an evolved cluster and at the same time of a dynamically young system. More detailed studies are needed to help us perform a more complete characterization of this intriguing system and its components.

Table 5.2: Properties of spectroscopic members of XMMU J0338.8+0021

ID	RA	DEC	z	σ_z	Projected Distance (arcsec)	Distance (kpc)	H (Vega)	$z-H$ (Vega)	Main spectral features
1-A	03:38:48.048	+00:21:08.06	1.5031	0.0006	20.8	175.8	18.25	3.30	MgII, FeII, CaH/K
5	03:38:49.159	+00:21:32.77	1.5024	0.0005	24.9	210.5	20.19	2.97	MgII, FeII, CaK
7	03:38:50.483	+00:21:55.65	1.4976	0.0007	49.8	421.4	19.17	2.81	MgII, FeII (weak), [OII] (weak)
6	03:38:48.449	+00:21:45.78	1.4899	0.0006	40.4	341.9	19.49	3.54	FeII, CaH/K
4	03:38:49.286	+00:21:20.43	1.4788	0.0013	12.6	106.7	19.53	2.84	CaH/K
11	03:38:52.357	+00:22:43.76	1.4736	0.0005	104.9	887.7	19.04	2.94	MgII, [OII] (weak), [NeIII], CaH/K
14	03:38:46.998	+00:23:27.98	1.4730	0.0007	144.5	1222.2	19.66	3.33	MgII, [OII] (weak), CaH/K

Chapter 6

Kinematic analysis of a sample of distant galaxy clusters

Abstract. This chapter reports the work of Nastasi et al. (2013b), close to the submission to A&A. Observations and cosmological simulations show galaxy clusters as a family of nearly *self-similar* objects with properties that can be described by scaling relations as a function of e.g. mass and time. Here we study the scaling relation between the velocity dispersion (σ_v) and the X-ray bolometric luminosity ($L_{X,500}^{Bol}$) in galaxy clusters in the high redshift regime ($0.60 \leq z \leq 1.46$) and compare our results with the analogous study of the local HIFLUGCS sample. For the analysis, we use a set of 15 distant galaxy clusters extracted from the literature and selected via different methods, plus a sample of 10 newly discovered clusters selected in X-rays within the XMM-*Newton* Distant Cluster Project (XDCCP) with more than 10 confirmed spectroscopic members per cluster. For both samples the same method was used to determine σ_v . To compare the high redshift results with conditions in the local Universe (in order to study the evolution of this scaling relation) we use the data from the HIFLUGCS sample, restricting the analysis to the clusters in the common $L_{X,500}^{Bol}$ range. We also investigated the $L_X - T_X$ and the $\sigma_v - T_X$ relations for the 15 clusters in the literature sample. We report the results of the X-ray and kinematic analysis of the 10 newly detected high redshift clusters. For our sample we find a slope fully consistent with the one typical of local clusters, albeit with a large ($\sim 26\%$) associated uncertainty. We repeated the fit, freezing the slope to $B = 3.58$, the one found for the HIFLUGCS systems restricted to the same luminosity range of our sample, in order to consider the evolution of the amplitude alone. We find a positive offset of $\Delta A = +0.34$ if the self-similar evolution is neglected, hence possibly indicating the need for including evolutionary effects. For the $L_X - T_X$ relation,

we find the best agreement with the local relation implying no significant evolution with redshift. Finally, the $\sigma_v - T_X$ relation also appears to be consistent with the theoretical expectation that galaxies and gas particles have a similar specific kinetic energy.

6.1 Introduction

Galaxy clusters are the most massive virialized objects in our Universe and, because of their relatively recent formation process, very sensitive probes to the underlying cosmological framework. In addition, they are excellent laboratories for testing models of galaxy formation and the role of merging, environment and radiative feedback in this context. In a scenario where clusters form only via pure gravitational forces, they should appear, at the end of their formation process, as a family of *self-similar* objects, i.e. the less massive ones should be the scaled down versions of the more massive ones, with the mass being to first order the only parameter for scaling all the other quantities¹. Self-similarity hence predicts that cluster observables such as X-ray temperature (T_X) of the ICM, X-ray bolometric luminosity computed within R_{500} ² ($L_{X,500}^{Bol}$), Sunyaev-Zel'dovich (SZ) Compton parameter and galaxy velocity dispersion (σ_v) should correlate with the *mass* (and among each other) via tight *scaling relations* (e.g., Kaiser 1986). The possibility of defining and efficiently calibrating such correlations is extremely important when assessing the total mass of the systems, a physical quantity that is not directly observable but that has a key role relating clusters to the cosmological framework and, hence, enable their usage as cosmological probes. Several studies on nearby clusters have indeed shown the existence of strong correlations between the X-ray observables of galaxy clusters and the velocity dispersion of their galaxy members (e.g., Mushotzky 1984; Ortiz-Gil et al. 2004), but these relations often exhibit slopes that deviate from the simple self-similar expectations (Wu et al. 1999), hence pointing toward the influence of additional physical effects and a variety of dynamical states of galaxy clusters. In addition, these observed trends also show a considerable scatter because of many effects such as ongoing merging processes (Ricker & Sarazin 2001), the presence of cool-cores (Fabian et al. 1994; Pratt et al. 2009) or an ICM heated by non-gravitational processes, e.g. central AGN feedback (Cavaliere et al. 2002; Puchwein et al. 2008). The study of the scaling relations between cluster observables, and especially their *evolution* with redshift,

¹More elaborate models, such as Navarro-Frenk & White (NFW, Navarro et al. 1997), have formation time as second parameter.

² R_{500} is defined as the radius within which the average mass density is 500 times the critical density of the universe.

can hence provide important information on the physical processes at work throughout the evolutionary path of such complex systems. In this context, it is therefore clear how important it is to push the above studies toward systems at higher redshifts and, possibly, also to consider observables that are related to different physical components of the clusters.

In this chapter we focus on the study of the relation between the bolometric X-ray luminosity, a quantity connected to the physical status of the hot ICM, and the 1D velocity dispersion along the line-of-sight (σ_v) of the member galaxies, for a sample of galaxy clusters selected in the redshift range $0.60 \leq z \leq 1.46$. We compare our results with the self similar expectation ($L_{X,Bol} \propto \sigma_v^4$) and with the empirical relations observed for the local HIFLUGCS sample at $\langle z \rangle = 0.05$ (Zhang et al. 2011). We also investigate how the X-ray temperature of the ICM correlates with galaxy velocity dispersion in order to test the assumption of isothermal and hydrostatic equilibrium between gas particles and galaxies. Finally, the $L_X - T_X$ relation is also investigated and compared with the local one defined in Pratt et al. (2009).

The chapter is structured as follows: in Sec. 6.3 we present the entire sample of our study, composed of 15 clusters extracted from the literature and 10 newly discovered clusters drawn from XMM-*Newton* Distant Cluster Project (XDCP) survey. The X-ray analysis and the spectroscopic reduction of the XDCP sample are then described in Sec. 6.4 and 6.5, respectively. In Sec. 6.6 we discuss the method we used in the kinematic analysis of the XDCP sample to estimate the σ_v values. The results and the comparison with the HIFLUGCS sample are then presented in Sec. 6.7. Sec. 6.8 provides a concluding discussion.

Throughout the entire chapter we assume a standard Λ CDM cosmology, with $\Omega_m = 0.3$, $\Omega_\Lambda = 0.7$ and $H_0 = 70 \text{ km s}^{-1} \text{ Mpc}^{-1}$.

6.2 The HIFLUGCS sample

The Highest X-ray FLUX Galaxy Cluster Sample (HIFLUGCS, Reiprich & Böhringer 2002) is a complete sample comprising 64 galaxy clusters drawn from the *ROSAT* All Sky Survey (RASS, Böhringer et al. 2004) with X-ray flux $f_{0.1-2.4\text{keV}} > 2 \cdot 10^{11} \text{ erg s}^{-1} \text{ cm}^{-2}$ and galactic latitude $|b| \geq 20.0 \text{ deg}$. The sample covers an area of two thirds of the sky and includes objects up to $z \approx 0.2$, with a median redshift of $\bar{z} = 0.05$. XMM-*Newton* archive data are also available for 63 clusters, resulting in ~ 1 Ms clean observations. The X-ray observables of the HIFLUGCS sample have then been accurately measured by combining XMM-*Newton* and ROSAT data.

The optical spectroscopic data used in Zhang et al. (2011) for estimating the galaxy velocity dispersions has been drawn from the literature (e.g., Andernach et al.

2005) and produced a total of 13,439 galaxies for 62 out of 64 clusters, with a number of spectroscopically confirmed members ranging from a minimum of 20 (cluster S1101) to a maximum of 972 (Coma). The X-ray bolometric luminosities of HI-FLUGCS clusters span the range $\sim 10^{42} - 10^{46}$ erg s $^{-1}$, one order of magnitude wider than the one of our distant sample, described in the next section. In Fig. 6.4 we compare the $L_{X,Bol}$ distribution of the two samples.

6.3 The distant cluster sample

In our study we consider a total of 25 galaxy clusters with both X-ray observations and optical spectroscopy for their member galaxies. The majority (19 out of 25) of the systems are X-ray selected, with 14 clusters drawn from the XMM-*Newton* Distant Cluster Project sample (Fassbender et al. 2011a). Five of these are drawn from the literature, whereas the others (6 out of 25) have been selected via their SZ effect or their optical red galaxy overdensity. 10 of the above mentioned 14 XDCP clusters are newly discovered and are labeled as “XDCP sample” throughout the chapter. Their main properties and the redshift list of their members are given in Tab. 6.2 and B.1, respectively. The remaining 15 systems are instead already published and represent the “literature sample” discussed in Sec. 6.3.1 and listed in Tab. 6.3.1.

All the clusters selected for our study have more than 10 spectroscopically confirmed members in order to guarantee a relatively reliable measurement of their σ_v (Biviano et al. 2006). In addition, in our sample we also include clusters with clear signs of ongoing merging because, as shown by Sifon et al. (2012) for a sample of SZ selected systems, we do not expect that their presence would produce a change in the estimated slope of the scaling relations but, instead, only boost their scatter.

6.3.1 The literature sample

We drew a sample of 15 distant ($z > 0.6$) clusters from the literature (updated to July, 2012) without constraining the way in which the systems were selected. We only imposed that the X-ray properties of the systems were also well characterized and that their authors provided an estimate of σ_v , computed with at least 10 members. In this way we obtain a sample of X-ray, IR, optically and SZ selected clusters whose main properties are summarized in Tab. 6.3.1.

For all the above systems (except ACT0102, Cl1604 and X2235) the complete set of redshifts of their member galaxies together with the associated errors are provided by the authors. This allowed us to compute their velocity dispersion (σ_v^{clip})

Table 6.1: Properties of the clusters selected from the literature for our study. The second reference in the *Ref* column contains the values of the X-ray properties ($L_{X,500}^{Bol}$ and kT) we adopt in this study, because these are updated and/or consistent with the used cosmology. σ_v^{lit} and N_{gal}^{lit} are the velocity dispersions and the number of members used to compute it, respectively, quoted in the literature. They generally differ from the σ_v^{clip} and N_{gal}^{clip} values we obtain with the 3- σ clipping procedure described in Sec. 6.6. For those clusters without a public redshift dataset the latter values are not computable (“n.a.”) and the ones quoted in the literature are used in our study.

ID	Ref	z	N_{gal}^{lit}	σ_v^{lit} (km s ⁻¹)	N_{gal}^{clip}	σ_v^{clip} (km s ⁻¹)	$L_{X,500}^{Bol}$ (10 ⁴⁴ erg s ⁻¹)	kT (keV)	Selected via
MS1137	Do99, Et04	0.785	23	884±150	23	1022±111	15.2±0.4	6.9±0.5	X-ray emission
RXJ1716	Gi99, Et04	0.813	37	1522±180	33	1334±132	13.9±1.0	6.8±1.0	X-ray emission
MS1054	Tr99, Et04	0.833	32	1170±160	31	1131±137	28.4±3.0	10.2±1.0	X-ray emission
RXJ1821	Gi04, Re11	0.816	20	775±150	19	854±126	10.4±1.5	4.7±1.2	X-ray emission
ACT0102	Me12	0.870	89	1321±106	n.a.	n.a.	136±6.8	14.5±1.0	SZ effect
Cl1604	Lu04, Re11	0.897	22	1226±200	n.a.	n.a.	2.01±0.4	2.5±1.1	Optical overdensity
X1229	Sa09	0.975	27	683±62	27	675±138	8.8±1.5	6.4±0.7	X-ray emission
X1230	Fa11	0.975	65	658±277	63	807±109	6.5±0.7	5.3±0.7	X-ray emission
SPT0546	An11, Re11	1.067	21	1181±215	20	1041±167	18.5±1.7	7.5±1.7	SZ effect
SPT2106	Fo11, Re11	1.132	18	1230±225	17	868±186	74.2±5.3	8.5±2.6	SZ effect
RDCS1252	Ro04, Et04	1.237	38	747±79	38	752±81	6.6±1.1	5.2±0.7	X-ray emission
SpARCS0035	Wi09, Fa11	1.335	10	1050±230	9	1105±125	1.8±0.5	4.5±3.0	MIR overdensity
X2235	Mu05	1.396	30	802±63	n.a.	n.a.	10±0.8	8.6±1.3	X-ray emission
ISCSJ1438	Br10, Re11	1.410	17	757±223	15	782±170	2.2±0.7	3.3±1.9	MIR overdensity
X2215a	Hi10, Re11	1.457	44	720±110	31	750±100	2.9±0.3	4.1±0.9	X-ray emission

References: Do99: Donahue et al. (1999), Et04: Ettori et al. (2004); Gi99: Gioia et al. (1999); Tr99: Tran et al. (1999); Gi04: Gioia et al. (2004); Re11: Reichert et al. (2011); Me12: cluster “*El Gordo*”, Menanteau et al. (2012); Lu04: Lubin et al. (2004); Sa09: Santos et al. (2009); Fa11: Fassbender et al. (2011b); An11: Andersson et al. (2011); Fo11: Foley et al. (2011); Ro04: Rosati et al. (2004); Wi09: Wilson et al. (2009); Mu05: Mullis et al. (2005); Br10: Brodwin et al. (2010); Hi10: Hilton et al. (2010).

independently in order to be consistent with the same method adopted for the XDCP clusters (Sec. 6.3.2) and described in Sec. 6.6. A comparison of our results with those of the literature are discussed in Sec. 6.6.2 and are shown in Fig. C.1, C.2 and C.3 in Appendix C.

6.3.2 The XDCP sample

In our study we also consider a sample of 10 newly discovered galaxy clusters, drawn from the *XMM*-Newton Distant Cluster Project (Böhringer et al. 2005; Fassbender et al. 2011a), whose main properties are listed in Tab. 6.2. XDCP is a serendipitous X-ray survey designed to find and study distant ($z \geq 0.8$) X-ray luminous galaxy clusters. The detection strategy involves 4 steps: (i) a cluster candidate is first detected as an extended X-ray source in archival *XMM-Newton* observations; (ii) obvious counterparts and nearby groups and clusters are identified by means of digital sky images and then discarded. (iii) Blank fields are then further studied by two-band photometric imaging, and (iv) promising high redshift candidates are finally subjected to spectroscopic redshift measurements, that also provide the final confirmation of a cluster. This approach has been very successful and within the XDCP project the largest sample of X-ray selected, distant clusters has been compiled to date, with 22 confirmed systems at $z > 0.9$ previously published (Fassbender et al. 2011a). This sample is now increased to 23 by including the newly confirmed system XMMU J2356-3441 (cl09) in Tab. 6.2 at $z = 0.939$, whose details are reported in the tables 6.2 and B.1. The selection of the members for each cluster has been done by applying an iterative clipping, as described in Sec. 6.6.

In order to verify that the radial distribution of the galaxies within the XDCP clusters does not show a particular bias toward the inner/outer regions, we show in Fig. 6.1 the *stacked* radial profile computed for the entire sample. For a consistent comparison the radial distances have been rescaled to R_{200} . The resulting distribution is then compared with a projected Navarro, Frenk & White (NFW, Navarro et al. 1997) profile (Bartelmann 1996), shown as a red curve in the plot. The shape of the distribution is indicative of a good radial sampling, apart from a slightly more peaked distribution expected for the central bin and for $R \geq 2 R_{200}$. We thus do not detect a strong bias, that would e.g. indicate a severe under-sampling in the dense central regions. The mild lack of observed galaxies for $R < 0.5 R_{200}$ is essentially due to the geometrical restrictions imposed by the FORS2 spectroscopic follow-up (Sec. 6.5) that force the placement of only a limited number of slits in the central, densest cluster regions (see Sec. 6.6.1). The most external radii ($R \geq 2 R_{200}$), instead, are more affected by the reduced success in spectroscopic member confirmation because

Table 6.2: Properties of the newly discovered XDCP clusters selected for our study. **NOTE:** the system XMMU J2215-1751 (cl10) was first reported in Fassbender et al. (2011a), but without the value of σ_v , which we compute for this work.

ID	z	N_{gal}^{clip}	σ_v^{clip} (km s ⁻¹)	$L_{X,500}^{Bol}$ (10 ⁴⁴ erg s ⁻¹)
XMMU J1450+0904 - cl01	0.642	13	414±136	1.05±0.20
XMMU J1119+1300 - cl02	0.676	13	499±87	0.35±0.09
XMMU J1044-0119 - cl03	0.755	17	795±188	1.70±0.60
XMMU J0002-3556 - cl04	0.770	13	1089±144	2.00±0.25
XMMU J1243+1313 - cl05	0.791	25	840±139	1.70±0.50
XMMU J0954+1738 - cl06	0.828	10	992±175	6.70±0.75
XMMU J0010-1127 - cl07	0.828	15	416±74	10.3±1.60
XMMU J0152-1338 - cl08	0.829	12	483±98	2.50±0.50
XMMU J2356-3441 - cl09	0.939	20	624±146	6.50±1.50
XMMU J2215-1751 - cl10	1.226	12	481±102	0.55±0.07

of the strong interlopers contamination.

In the next sections we present the analysis of X-ray (Sec. 6.4) and optical spectroscopic data (Sec. 6.5) for the XDCP sample.

6.4 X-ray analysis

By definition of the XDCP strategy, all clusters listed in Tab. 6.2 have been detected as extended sources in XMM-*Newton* archive observations. The source extraction was carried out by means of SAS v6.5, applying a strict two-step flare cleaning process for the removal of high background periods. For most of the sources, the clean exposure time is >10 ksec for at least two of the XMM-*Newton* detectors.

For the flux measurements, we applied the growth curve analysis (GCA, Böhringer et al. 2000) method in the soft 0.5 - 2 keV band. In this method, the radial function of the cumulative source counts with background subtraction is determined. The total observed source count rate is determined from the plateau of this curve. In subsequent iterations, we use the X-ray luminosity to estimate the mass and the overdensity radius R_{500} by means of the scaling relations given in Pratt et al. (2009). We then obtain the net source count rate from the growth curve inside an aperture of R_{500} . To determine the flux and 0.5 - 2 keV rest frame X-ray luminosity we estimate

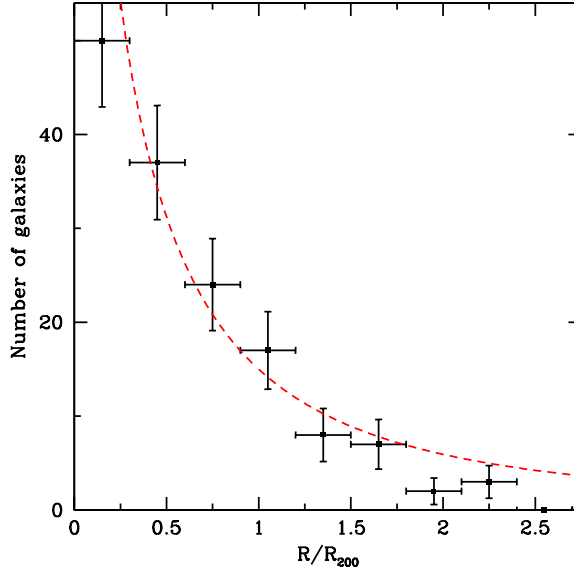


Figure 6.1: Radial distribution of all the galaxy members of the 10 XDCP clusters considered. The distances are rescaled to R_{200} and the red dashed line is the best projected NFW fit. Vertical error bars represent Poisson errors. The shape of the distribution is indicative of a good radial sampling, albeit slightly lower in the innermost and outermost regions.

the cluster ICM temperature using the relations in Pratt et al. (2009) and determine the appropriate conversion factor with the **XSPEC** software assuming a metallicity of 0.3 solar and an interstellar hydrogen column density taken from Kalberla et al. (2005).

The bolometric luminosities $L_{X,500}^{Bol}$ have been finally obtained by means of **XSPEC**, by extrapolating the energy distribution observed in the 0.5 - 2 keV band to 0.01 - 100 keV assuming an ICM metallicity of $Z = 0.3 Z_{\odot}$ for all the clusters. The values of $L_{X,500}^{Bol}$, together with the associated errors, are reported in the 6th and 7th column of Tab. 6.2.

6.5 Spectroscopic reduction

All the XDCP clusters have been followed-up at the VLT-FORS2 spectrograph (Appenzeller et al. 1998) in the multi-object spectroscopy (MOS) configuration, with an average of ~ 50 $1''$ width slits per mask. The observations were made by using

the grism 300I+11, which provides a resolution of $R = 660$ and a wavelength coverage of $6000\text{\AA} \leq \lambda \leq 11000\text{\AA}$. The optical spectroscopic data have been reduced with a new dedicated pipeline: *F*-VIPGI, an adapted version of VIPGI (Scodreggio et al. 2005) for FORS2 data (Chapter 4). The reduction processes included all the standard steps (bias subtraction, flat-fielding, wavelength calibration) and the final redshift values were assessed by cross-correlating each 1D extracted spectrum with a library of different templates using the software package EZ (Garilli et al. 2010).

In Appendix B, we provide a table containing the redshifts of all observed member galaxies of the newly discovered XDCP clusters included in the kinematic analysis, except for clusters XMMU J0010-1127 (cl07) and XMMU J2215-1751 (cl10), as their redshifts list will be provided in a forthcoming paper (de Hoon et al., submitted)

6.6 Kinematic analysis

As already mentioned in the previous sections, for the XDCP sample we considered only those clusters having more than 10 spectroscopically confirmed members. For the member selection and the following velocity dispersion computation we adopted a two-step procedure. Namely, we apply a first member selection as described in Halliday et al. (2004), i.e. by cutting a redshift window of ± 0.015 centered on the redshift of the brightest central galaxy (BCG) or, if such a galaxy was not clearly identifiable, on the median of the redshift peak of the galaxies found within $1'$ from the X-ray emission center and with a relative rest-frame velocity offset of $|\Delta v_{rest}| < 3000 \text{ km s}^{-1}$. On this new galaxy subsample³ ($\bar{z}_{0.015}$) we then compute the velocity dispersion σ_v by applying the method “2₃₀₀” defined and used by Milvang-Jensen et al. (2008) on a sample of 21 EDisCS clusters at redshifts $0.40 \leq z \leq 0.96$ and with $4 \leq N_{gal} \leq 50$. This method consists of a refinement of the member selection via an iterative 3σ clipping on $\bar{z}_{0.015}$ and, after various tests, was found by those authors to be the only method always able to provide the most (visually judged) correct and robust results. The process starts with a first guess on z_{cl} and σ_v given by the biweight location estimator (Beers et al. 1990) of $\bar{z}_{0.015}$ and $\sigma_v^{guess} = 300 \text{ km s}^{-1}$, respectively. Therefore, the procedure is iterated starting by selecting those galaxies with $-3\sigma_v^{guess} < v_{rest} < +3\sigma_v^{guess}$ and then recomputing σ_v^{guess} for this new subsample. After that, the above clipping criterion is applied again by using the last estimate of σ_v^{guess} and allowing the previously clipped galaxies to re-enter in the analysis. The values of the velocity dispersion are computed via the biweight scale

³We highlight that the galaxies discarded as members with this first cut cannot enter the analysis at later stages.

estimator if $N_{gal}^{clip} > 10$, or the gapper scale estimator otherwise. In addition, for each computed σ_v^{guess} we also applied the correction due to the uncertainties on the single redshift values as prescribed by Danese et al. (1980). We found that convergence is usually reached in 3 – 4 steps and the results of our analysis are summarized in Tab. 6.2 and shown in Fig. B.1, B.2 and B.3. The quoted error on each σ_v has been estimated as the rms of 1,000 bootstrapped realizations created from the final clipped redshift set, also subjected to the same iterative-clipping process described above.

We also remind the reader here that Beers et al. (1990) extensively demonstrated the *robustness* and *efficiency* of the biweight estimators, able to provide robust results independently of the assumed nature of the population and the presence of outliers, providing that the studied sample had a size of $N > 10$. This fact has mainly driven our choice of restricting the analysis to those clusters with a final $N_{gal}^{clip} > 10$.

6.6.1 Introduced bias

In XDCP the spectroscopic targets are preferentially selected among the most luminous galaxies, with colors consistent with the observed red-sequence. As explained in Fassbender et al. (2011a), this strategy is in fact able to maximize the number of real cluster members finally recovered from the spectroscopic follow-up. Because of the geometrical restrictions imposed on the slit positions of the FORS2 masks, the number of slits that can be used to sample the innermost regions of a cluster is very small (a maximum of 6 within the central $30''$, for typical $6''$ length slits) and, hence, the densest regions of the systems tend to be slightly *under*-sampled, as shown in Fig. 6.1. This effect can hence introduce a bias in our galaxy sample, with the most central members preferentially being also the most luminous and red. A σ_v estimate entirely based on such a sample could be significantly biased toward lower values because of the dynamical friction effect which only acts effectively on the most massive galaxies (Biviano et al. 2006; Saro et al. 2012). However, an inspection of our data shows that we have a mixture of bright ($H_{Vega} \lesssim 18$) and faint ($H_{Vega} \sim 20$) galaxies also in the center. As shown in Saro et al. (2012), a sample of “randomly selected” galaxies significantly reduces the above bias on σ_v , with a low ($N \leq 30$) number of members.

6.6.2 Test on accuracy of velocity dispersion measurements

We applied the method described in Sec. 6.6 to the redshift sets of the “literature sample”. In Fig. C.1 and C.2 we show the comparison of the σ_v values computed with our method (black gaussian) with the ones provided by the different authors

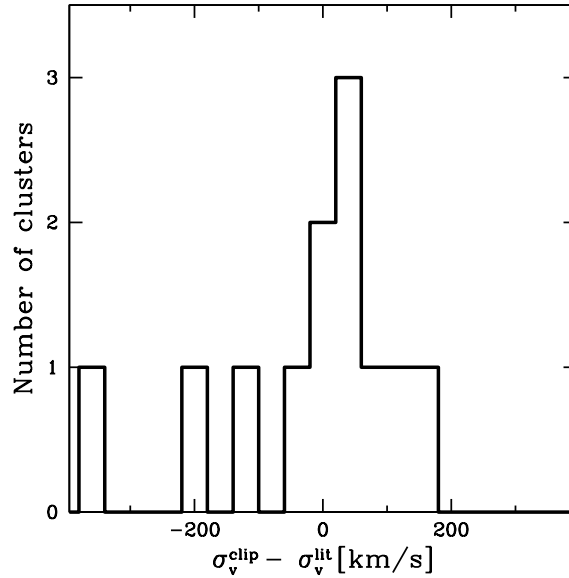


Figure 6.2: The absolute differences between the σ_v estimated by us using the two-step iterative clipping procedure described in Sec. 6.6 and the ones provided by the literature. A median offset of $\Delta\sigma_v = 25 \pm 59 \text{ km s}^{-1}$, corresponding to a relative difference of $\Delta\sigma_v/\sigma_v = 0.03 \pm 0.06$, is found.

(red gaussian). Although we see some discrepancies in the numbers of the finally selected members, the different estimates are in agreement within the errors and, as shown in Fig. 6.2, the relative differences $\Delta\sigma_v/\sigma_v$ are less than $\sim 10\%$.

6.7 Results

In this section we discuss the results of the fitting procedure of the $L_X - \sigma_v$, $L_X - T_X$ and $\sigma_v - T_x$ relations for our sample of 25 distant galaxy clusters, where T_X is the X-ray determined temperature of the ICM. We always use the BCES bisector fitting method which takes into account heteroscedastic errors (i.e. varying randomly and independently from point to point) on both variables (Akritas & Bershady 1996). The X-ray bolometric luminosity and velocity dispersion values are normalized to $10^{44} \text{ erg s}^{-1}$ and 1000 km s^{-1} , respectively, whereas the relations involving T_X assume

this quantity normalized to 5 keV. Therefore, the fitted relations are in the form:

$$\log \left(\frac{L_{X,500}^{Bol}}{E(z)^\alpha \cdot 10^{44} \text{erg/s}} \right) = B \cdot \log \left(\frac{\sigma_v}{1000 \text{km/s}} \right) + A \quad (6.1)$$

$$\log \left(\frac{L_{X,500}^{Bol}}{E(z)^\alpha \cdot 10^{44} \text{erg/s}} \right) = B \cdot \log \left(\frac{T_X}{5 \text{keV}} \right) + A \quad (6.2)$$

$$\log \left(\frac{\sigma_v}{1000 \text{km/s}} \right) = B \cdot \log \left(\frac{T_X}{5 \text{keV}} \right) + A \quad (6.3)$$

where α parametrizes the evolutionary behaviour of the relation. In Sec. 6.7.1 we show the best fit obtained for the 25 distant clusters. We provide two fits, one for a value of the exponent of the evolution parameter $\alpha = 0$ (no evolution of the relation) and one for $\alpha = 1$ (self-similar evolution). The choice of these values comes from the observed relation between L_X and T_X . T_X is analogous to σ^2 and we expect both parameters to behave similarly in relation to L_X .

According to the studies of Reichert et al. (2011), there is no significant evolution of the $L_X - T_X$ relation with redshift, but uncertainties are so large that a significant positive evolution cannot be ruled out. We therefore bracket the range of ignorance by the two different values of α .

In Sec. 6.7.1 we compare our sample with that of HIFLUGCS at $z \sim 0.05$ (Zhang et al. 2011) by fitting the high- z scaling relation with the same slope found for those local clusters residing in the same L_X range. In fact, as shown in Fig. 6.4, the range of $L_{X,500}^{Bol}$ spanned by the distant and nearby sample is quite different, with the latter having objects 2 orders of magnitude less luminous than the faintest cluster at $z > 0.6$. Since comparing objects with too different luminosities may induce a bias in the studied relations, we took into account the HIFLUGCS slope computed in the common luminosity range $L_{X,500}^{Bol} > 10^{43} \text{ erg s}^{-1}$. We also considered cases with $\alpha = 0$ and $\alpha = 1$, although the difference is negligible for the local sample.

Finally, in Sec. 6.6 and 6.7.3 we study how the X-ray temperature of the ICM correlates with L_X and σ_v in the “literature sample” clusters. We limited the analysis to the literature systems because the X-ray data of the “XDCP clusters” were not deep enough to enable a safe measurement of their T_X .

A summary of all the parameters found for the fitting relations of the different cases are given in Tab. 6.3.

6.7.1 The $L_X - \sigma_v$ relation

Distant sample alone

We applied the BCES bisector analysis to the $L_{X,500}^{Bol}$ and σ_v measured for our distant sample of 25 clusters. As mentioned in Sec. 6.7, we consider two cases assuming no evolution ($\alpha = 0$) and self-similar evolution ($\alpha = 1$) for the scaling relations. The results are shown in Fig. 6.3.

As summarized in Tab. 6.3, we find a slope of $B \simeq 4.1$ for both the models, although with a large ($\sim 26\%$) associated uncertainty, fully consistent with the findings of Zhang et al. (2011) and Ortiz-Gil et al. (2004) for clusters in the local universe.

Distant sample with HIFLUGCS slope

In order to investigate the differences in normalization between the $L_X - \sigma_v$ relation for distant and local clusters, we repeated the analysis done in Sec. 6.7.1 but freezing the slope to the one holding for the HIFLUGCS clusters. However, as shown in the histogram in Fig. 6.4, the HIFLUGCS sample reaches an X-ray luminosity limit that is 2 orders of magnitude less luminous than the faintest cluster in our distant sample. In order to alleviate the possible bias introduced by considering objects so different in luminosity, we considered the slope computed only with those HIFLUGCS objects residing in the common luminosity range $L_{X,500}^{Bol} > 10^{43} \text{ erg s}^{-1}$. Our fit on this HIFLUGCS subsample produced a flatter slope ($B = 3.58$) w.r.t. the entire sample, but still in agreement with the original result within the uncertainty limits. The results are shown in Fig. 6.5.

The normalizations in the two cases differ from the local sample by $\Delta A/A \sim 31\%$ and $\Delta A/A \sim 11\%$, for $\alpha = 0$ and $\alpha = 1$, respectively.

6.7.2 The $L_X - T_X$ relation

We also investigated the relation between $L_{X,500}^{Bol}$ and the X-ray temperature (T_X) of the ICM only for the sample of the literature clusters. For these objects the values of T_X were measured directly by the authors and are listed in Tab. 6.3.1. The result of this study is shown in Fig. 6.6 and summarized in Tab. 6.3. In the same plot we also show in red the relation found in Pratt et al. (2009) at $z \sim 0$:

$$h(z)^{-1} L_X = (6.07 \pm 0.58) (T_X / 5 \text{ keV})^{2.70 \pm 0.24} 10^{44} \text{ erg s}^{-1} \quad (6.4)$$

We find quite steep slopes but with large uncertainties ($\sim 25\%$), mainly due to the small number of points. However, as shown in Fig. 6.6, the best agreement between

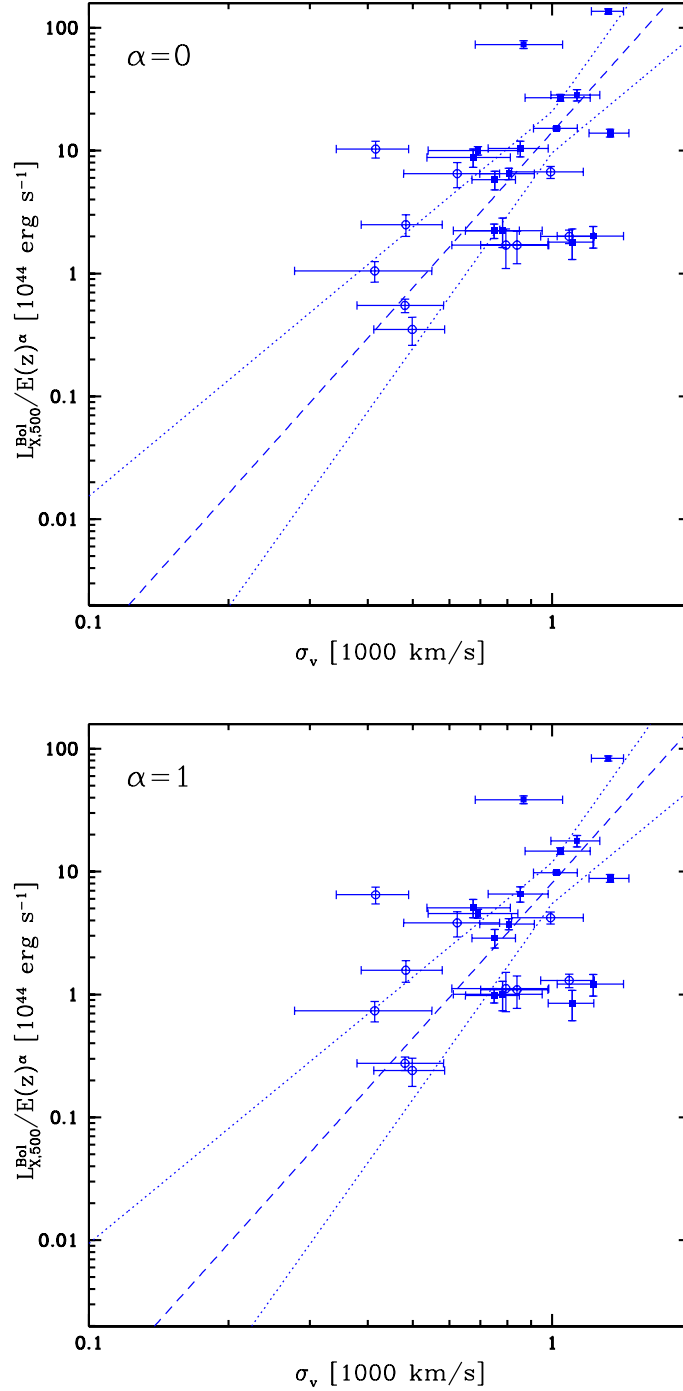


Figure 6.3: $L_{X,500}^{Bol} - \sigma_v$ relation of our distant sample for no evolution ($\alpha = 0$, *top*) and self-similar ($\alpha = 1$, *bottom*) evolution. The filled squares mark the “literature sample” whereas the empty circles represent the “XDCP sample”. The best fits are marked by dashed lines and their 1σ uncertainties by the dotted ones.

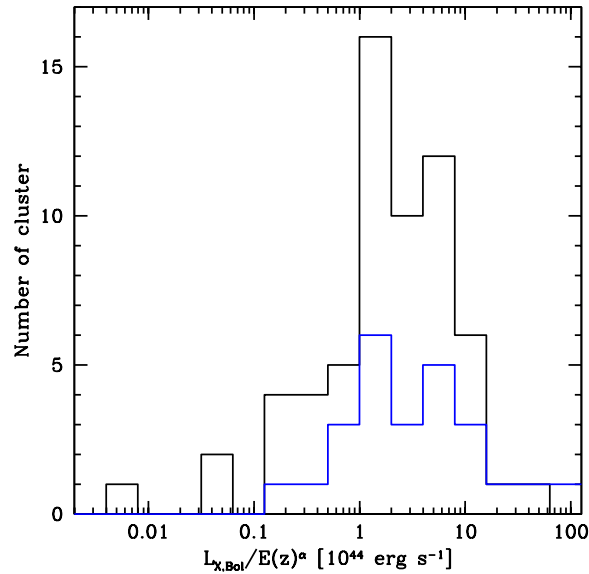


Figure 6.4: Histogram of the $L_{X,500}^{Bol}$ for both the HIFLUGCS sample (black) and our sample of 25 distant clusters (blue). The common luminosity range considered is $L_{X,500}^{Bol} > 10^{43} \text{ erg s}^{-1}$.

the distant and local relation is recovered for $\alpha = 0$, favouring a scenario where no significant evolution with redshift is expected in the $L_X - T_X$ relation.

6.7.3 The $\sigma_v - T_X$ relation

Finally, we investigated the $\sigma_v - T_X$ relation for those 12 literature clusters for which we could compute σ_v . These two quantities are important as both probe the depth of the cluster potential well estimated by using baryons as tracers. Since the gas particles of the ICM and the cluster galaxies feel the same potential, under the assumption that they both have the same specific kinetic energy, it is expected that:

$$\frac{\sigma_v^2 \mu m_p}{k_B T_X} \approx 1 \quad (6.5)$$

where m_p is the proton mass, k_B the Boltzmann constant and μ is the mean molecular weight. If this assumption holds, one would expect that $\sigma_v \propto T_X^{0.5}$. We tested this assumption by comparing the computed best fit of the data with the self-similar relation $\sigma_v \propto T_X^{0.5}$. The result is shown in Fig.6.7. From Fig.6.7 and the value

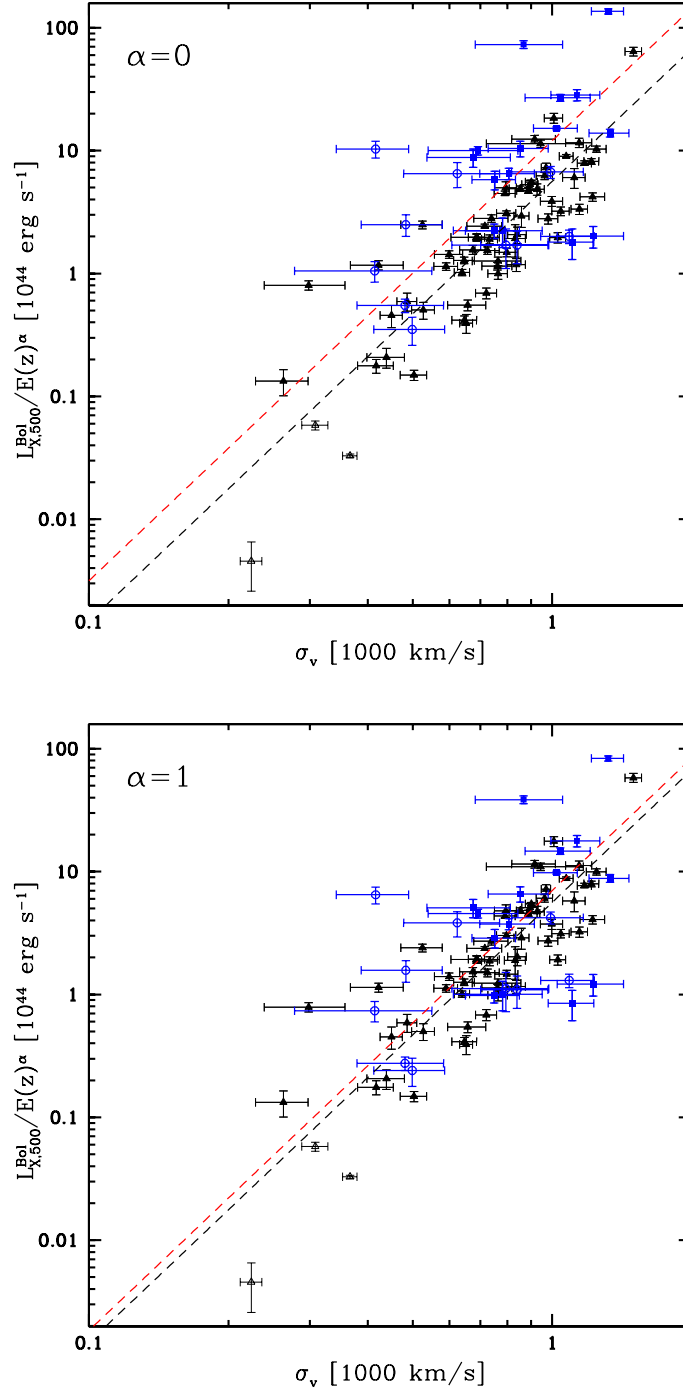


Figure 6.5: $L_{X,500}^{Bol} - \sigma_v$ adopting the same convention of Fig. 6.3. The black triangles represent the HIFLUGCS sample, with filled symbols referring to those objects in the common luminosity range $L_{X,500}^{Bol} > 10^{43} \text{ erg s}^{-1}$ and yielding a best fit relation with a slope of $B = 3.58$ (black, dashed line). The best fit of the distant sample assuming the above slope is represented by the red, dashed line and the 1σ error is not shown for clarity.

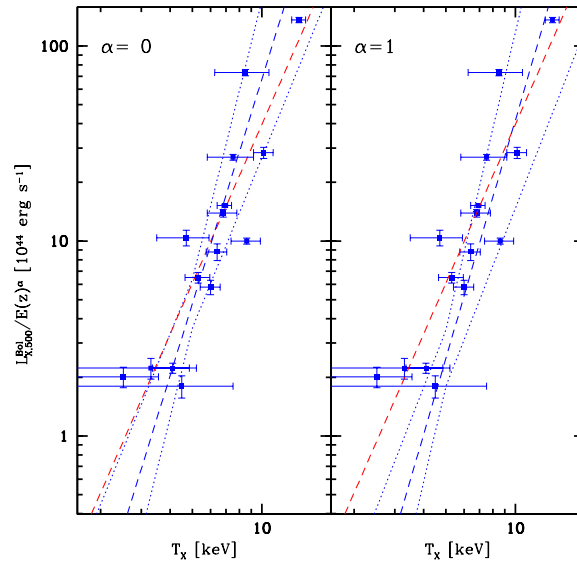


Figure 6.6: The $L_X - T_X$ relation found for the distant sample of literature clusters. In red is shown the empirical relation of Pratt et al. (2009).

reported in Tab. 6.3 it appears that, albeit with a large scatter, the obtained relation is consistent with the self-similar expectation.

All the the parameters of the relations discussed in Sec. 6.7.1 are summarized in Tab. 6.3.

6.8 Summary and conclusion

In this chapter we provided the kinematical and X-ray properties of a sample of 10 newly discovered, X-ray selected galaxy clusters drawn from the XMM-*Newton* Distant Cluster Project survey. These new systems reside in the redshift range $0.65 \leq z \leq 0.94$, with X-ray luminosities $0.35 \leq L_{X,500}^{Bol}/(10^{44} \text{erg s}^{-1}) \leq 10.3$ and complement the XDCP sample reported by Fassbender et al. (2011a), increasing it to **31** spectroscopically confirmed clusters in the redshift range $0.6 < z < 1.6$.

We analyzed the correlations existing between the X-ray properties and the galaxy velocity dispersion of the 10 new XDCP systems together with a sample of 15 distant clusters drawn from the literature. We also compared the $L_X - \sigma_v$ results with the trend typically observed in the local Universe, taking as reference the findings of Zhang et al. (2011) for the HIFLUGCS sample at $\langle z \rangle = 0.05$. In summary, we

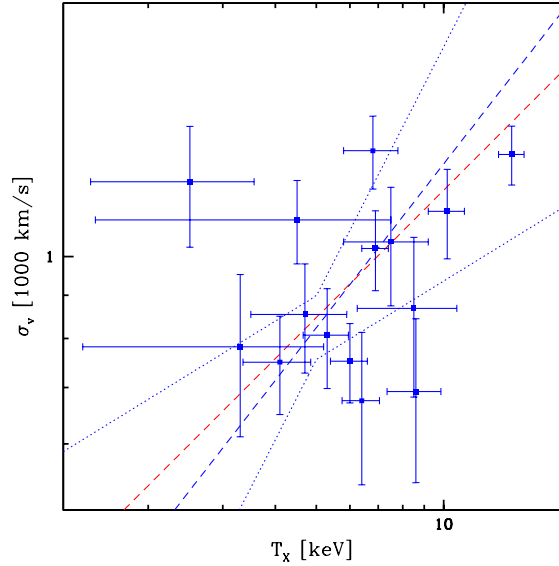


Figure 6.7: The $\sigma - T_X$ relation found for 12 clusters of the literature sample. In red is shown the theoretical expectation of $\sigma_v \propto T_X^{0.5}$.

found that:

- the slope of the $L_X - \sigma_v$ relation appears fully consistent with the trend observed in the local Universe, with a slope of $B \simeq 4.1$ both assuming no evolution or a self-similar evolution ($\alpha = 0$ and $\alpha = 1$, respectively);
- we measure an offset of the normalization between the distant and the HI-FLUGCS sample clusters in the same luminosity range of $\Delta A/A \sim 11\%$ and 31% assuming $\alpha = 1$ and $\alpha = 0$, respectively. This finding seems to favour a scenario where self-similar evolution of the scaling relations is indeed relevant. However, part of the offset found in the $\alpha = 0$ case may be due to *bias* effects introduced by the flux limited nature of the cluster selection. As shown by Reichert et al. (2011), in fact, at redshift $z \geq 0.7$ the correction factor on the luminosities could amount to a maximum of $\sim 25\%$.
- The $L_X - T_X$ relation appears *steeper* than the local one but this may be an effect of the small number of points. A direct comparison of the data distribution of the distant sample with the fit to the nearby clusters in Fig. 6.6 suggests a fair agreement. In this case the better match is found with the $z \sim 0$ trend for $\alpha = 0$, pointing toward an absence of evolution.

Table 6.3: Summary of the fitting parameters for the $L_X - \sigma_v$, $L_X - T_X$ and $\sigma_v - T_X$ relations, assuming the form: $\log(Y) = B \cdot \log(X) + A$.

$L_X - \sigma_v$							
B	Err(B)	A	Err(A)	Sample	α	$L_{X,500}^{Bol}$ range	Figure
4.210	1.080	1.150	0.168	Distant	0	$> 10^{43}$ erg s $^{-1}$	6.3 – <i>left</i>
4.200	1.100	0.907	0.167	Distant	1	$> 10^{43}$ erg s $^{-1}$	6.3 – <i>right</i>
4.010	0.334	0.782	0.048	HIFLUGCS	1	All	6.5
3.580	0.357	0.749	0.048	HIFLUGCS	1	$> 10^{43}$ erg s $^{-1}$	6.5
3.580	0.974	1.080	0.158	Distant - fixed slope	0	$> 10^{43}$ erg s $^{-1}$	6.5 – <i>left</i>
3.580	0.964	0.845	0.156	Distant - fixed slope	1	$> 10^{43}$ erg s $^{-1}$	6.5 – <i>right</i>
$L_X - T_X$							
3.820	0.923	0.679	0.125	Literature	1	$> 10^{43}$ erg s $^{-1}$	6.6 – <i>left</i>
4.050	1.020	0.399	0.144	Literature	0	$> 10^{43}$ erg s $^{-1}$	6.6 – <i>right</i>
$\sigma_v - T_X$							
0.643	0.335	-0.084	0.038	Literature	–	$> 10^{43}$ erg s $^{-1}$	6.7

- The $\sigma_v - T_X$ relation appears fully consistent with self-similar expectations, with $\sigma_v \propto T_X^{0.643 \pm 0.335}$.

The results reported here demonstrate that the galaxy velocity dispersion can be established as a useful mass proxy for distant clusters on a similar level as e.g. X-ray luminosity. Much better data statistics are, however, required to obtain a reliable calibration of the relations studied. These data will be delivered by the increasing efforts in deeper X-ray, SZ and optical/infrared surveys.

Chapter 7

Summary and Conclusions

In this thesis I discussed the importance of galaxy clusters both as cosmological probes and astrophysical laboratories. In this context, *distant* clusters play a key role as their abundance is particularly sensitive to the dark energy and dark matter content of the universe and also represent the stages where the process of galaxy formation in densest environments can be studied since at an early phase. However, while the local cluster population is already well characterized since the beginning of the 90s, the study of the high redshift systems is a relatively young field and until 10 years ago only few systems at $z > 0.8$ were known. A breakthrough in this scenario took place in the same years with the arrival of new, high performance X-ray imaging telescopes like XMM-*Newton* and Chandra.

I then highlighted the uniqueness of the XMM-Newton Distant Cluster Project, the first survey specifically designed to exploit the high quality data of XMM-*Newton* in order to unveil and characterize, with multi-wavelength follow-up, the most distant X-ray luminous galaxy clusters of the universe. Finally, I extensively illustrated the work I have carried out within XDCP and how it has actively contributed to the success of the project. Namely, my results can be summarized as follow:

- I improved the efficiency of the reduction and extraction of the optical spectra for distant cluster members by developing a new, semi-automated pipeline for FORS2 spectroscopic data: *F-VIPGI*. The extensive use of this new software during the last two years significantly accelerated the confirmation rate of new distant systems in XDCP. This contributed to the construction of the largest sample of 22 X-ray selected, spectroscopically confirmed clusters at $z > 0.9$, comprising also three systems in the so-called “redshift desert”, at $z \geq 1.5$. This sample has been publicly released by Fassbender et al. (2011c).

- I studied the spectrophotometric properties of stacked spectra of a sample of 186 cluster galaxies at $0.6 < z < 1.2$. By measuring the spectral indices of their optical spectra, I classified them in five spectral classes. Then, I stacked all the spectra in each group, in order to create a *new library of empirical, spectroscopic templates* representative of the galaxy population in distant clusters. This library is now publicly available (see Appendix A) and is specifically suited for better redshift (spectroscopic and photometric) measurements of galaxies residing in the densest high- z environments.
- By comparing my averaged spectra with the ones provided by other surveys, I found that passive galaxies in distant clusters appear to be more evolved than the coeval ones residing in the field. This finding supports the idea that galaxy evolution is significantly accelerated in the densest environments. However, because of the similarities found between our passive template and the one of the most luminous, red galaxies at lower redshift, a significant role of the *mass* in this process cannot be ruled out as well.
- I also studied the rest-frame $U - B$ colors of the averaged spectra and compared them with the ones observed in the Coma Cluster at $z \sim 0$. I found that the high- z passive and quiescent star-forming galaxies exhibit rest-frame colors that are fully in agreement with the ones of the early type galaxies in local clusters, hence suggesting that the bulk of their stellar mass was already formed at $z \sim 0.8$.
- I discussed the characteristics of XMMU J0338.8+0021 at $z = 1.49$: one of the three most distant XDCP clusters I confirmed. This system exhibits peculiar aspects that make it remarkably different from the typical clusters in the local universe. Specifically, the large offset between the X-ray centroid and the BCG position, together with the evidence of an actively merging BCG and a non negligible spread of the galaxy red sequence, suggests that this cluster is actually observed in a young phase of its mass assembly process.
- Finally, I studied the correlations between the X-ray properties and the galaxy velocity dispersion for a sample of 25 distant, X-ray luminous galaxy clusters. 10 newly confirmed XDCP clusters at $0.65 < z < 0.95$ have been included in my sample. My results for the $L_X - \sigma_v$ relation are fully in agreement with the one observed in the local universe, albeit large uncertainties mainly due to the relatively low number of galaxies usable for computing σ_v in each system. By comparing the normalization of the above relation with the one of a local cluster sample (HIFLUGCS) I found some evidence for a *self-similar* evolution,

i.e., an evolution driven only by gravitational processes. This conclusion is further supported by the found slope for the $\sigma_v - T_X$ relation, which suggests (albeit with large uncertainty) the existence of a thermodynamical equilibrium between galaxies and ICM particles. For the $L_X - T_X$ relation the self-similar model does not provide such a good description of the observations. In this case, in fact, a model which predicts no evolution at all for the involved ICM quantities seems to give a better account of the observational data.

Appendix A

Additional information on *F*-VIPGI

In the following appendix I provide some additional information useful to readers who consider using the software discussed in Chapter 4.

A.1 Compatibility with the current operating systems

F-VIPGI is fully compatible with those architecture softwares where the old version of VIPGI can be installed and run. Since a few years, however, the plotting library Pmw.BLT is not updated anymore and hence started to become obsolete and incompatible with some recent operating systems and with all current 64-bit machines.

In the following I list all operating systems that fully support the current version of *F*-VIPGI with their version numbers reported in parenthesis:

- Linux SuSE (9.X, 10.X, 11.0 and 11.1)
- Linux Fedora (from 8 to 14)
- Linux Ubuntu (from 8.xx to 10.xx)
- Solaris (2.5)
- Mac OSX (10.5 and 10.6)

Another improved version of VIPGI is already being developed and is expected to be completed by the mid of 2013. It will use a completely renewed graphical interface, fully usable also with the most recent architecture softwares, and it will also include reduction recipes suitable for LUCIFER data, the spectrograph mounted at the LBT.

I finally stress that *F*-VIPGI is publicly released to the community as it is and without any guarantee of technical support due to the lack of funds to support such assistance.

A.2 How to obtain *F*-VIPGI

The add-ons and the binary files of *F*-VIPGI can be downloaded from the following link:

<http://www.mpe.mpg.de/cosmology/cluster/FVIPGI>

In the package, the cookbook of the new pipeline is also included.

A.3 Link for spectroscopic templates

The new library of spectra described in Chapter 4, as well as some related technical information, are available in electronic format as ASCII and Flexible Image Transport System (*fits*) files at the CDS via anonymous ftp to `cdsarc.u-strasbg.fr` 130.79.128.5 or via <http://cdsarc.u-strasbg.fr/viz-bin/qcat?J/A+A/vol/page> and at the following link:

<http://www.mpe.mpg.de/cosmology/cluster/FVIPGI/specLib>

Appendix B

Redshifts list of “XDCP sample” clusters

In this Appendix I provide the detailed redshifts list of the “XDCP sample” clusters listed in Tab.6.2. However, here I do not include XMMU J0010-1127 (cl07) and XMMU J2215-1751 (cl10) as their spectroscopic details will be provided in another forthcoming paper (de Hoon et al., submitted).

At the end of the Appendix I also show the rest-frame velocity histograms of the 10 newly discovered clusters, overplotted with the best gaussian fit whose variance σ_v^{clip} is computed via the method described in Sec.6.6.2.

Table B.1: Spectroscopic details of the galaxies of the XDCP clusters listed in Tab.6.2. The two systems XMMU J0010-1127 (cl07) and XMMU J2215-1751 (cl10) are not included. The “QF” column report the quality flag associated to each spectroscopic redshift, with QF = 2, 3 and 4 corresponding to a confidence level for the estimated z value of $>75\%$, $>90\%$ and 100% , respectively, whereas QF = 1 is for tentative estimates. A check mark symbol in the last column indicates that the object has been rejected as cluster member by the σ -clipping procedure described in Sec. 6.6.2. All objects with QF = 1 are excluded from the analysis.

R ₂₀₀ (kpc)	RA (J2000)	DEC (J2000)	z	z _{err}	QF	Distance from X-ray centroid ($''$) (kpc)	(r/R ₂₀₀)	Clipped out
XMMU J1450+0904 - cl01								
844	14:50:09.20	+09:04:39.10	0.6417					
	14:50:09.25	+09:04:39.22	0.6419	0.0002	3	1	6	0.007
	14:50:09.22	+09:04:45.12	0.6425	0.0002	3	6	42	0.050
	14:50:10.36	+09:04:23.46	0.6418	0.0002	2	23	160	0.189
	14:50:09.50	+09:04:15.87	0.6430	0.0002	3	24	163	0.193
	14:50:07.45	+09:04:28.72	0.6429	0.0002	3	28	192	0.227
	14:50:09.33	+09:04:06.54	0.6377	0.0002	3	33	225	0.266
	14:50:10.42	+09:03:53.25	0.6462	0.0003	2	49	339	0.401
	14:50:10.61	+09:05:32.41	0.6379	0.0002	3	57	394	0.466
	14:50:13.75	+09:03:21.85	0.6407	0.0002	3	103	707	0.837

Table B.1: Continued.

R_{200} (kpc)	RA (J2000)	DEC (J2000)	z	z_{err}	QF	Distance from X-ray centroid ($''$) (kpc) (r/R_{200})			Clipped out
	14:50:15.97	+09:02:57.48	0.6420	0.0002	2	143	984	1.165	
	14:50:04.95	+09:06:55.00	0.6405	0.0002	3	150	1032	1.221	
XMMU J1119+1300 - cl02									
737	11:19:07.70	+13:00:23.79	0.6764						
	11:19:08.47	+13:00:22.62	0.6725	0.0002	3	11	80	0.108	
	11:19:07.67	+13:00:03.03	0.6721	0.0002	2	21	146	0.198	
	11:19:05.68	+13:00:03.78	0.6764	0.0002	3	36	251	0.340	
	11:19:06.48	+12:59:50.72	0.6773	0.0002	3	38	265	0.359	
	11:19:04.45	+13:00:08.97	0.6762	0.0002	3	50	351	0.476	
	11:19:03.95	+13:00:09.34	0.6764	0.0002	3	57	399	0.541	
	11:19:02.74	+13:00:29.95	0.6732	0.0002	4	73	513	0.696	
	11:19:02.06	+13:00:05.85	0.6790	0.0002	3	84	594	0.806	
	11:19:00.03	+13:00:05.23	0.6742	0.0002	3	114	800	1.085	
	11:18:59.54	+12:59:53.31	0.6784	0.0002	3	123	867	1.176	
	11:19:00.47	+13:01:40.94	0.6921	0.0003	2	131	922	1.250	✓
	11:18:58.13	+13:00:01.33	0.6810	0.0003	3	142	998	1.353	
	11:18:55.50	+12:59:28.71	0.6803	0.0006	2	187	1315	1.783	
	11:18:52.70	+13:00:51.52	0.6763	0.0002	3	221	1557	2.112	
XMMU J1044-0119 - cl03									
768	10:44:43.70	-01:19:54.30	0.7545						
	10:44:43.86	-01:19:53.09	0.7548	0.0002	3	3	20	0.026	
	10:44:43.68	-01:19:59.99	0.7508	0.0002	2	6	42	0.055	

Table B.1: Continued.

R_{200} (kpc)	RA (J2000)	DEC (J2000)	z	z_{err}	QF	Distance from X-ray centroid (") (kpc) (r/ R_{200})			Clipped out
	10:44:43.03	-01:19:39.70	0.7490	0.0002	3	18	130	0.169	
	10:44:43.94	-01:20:27.07	0.7686	0.0002	1	33	242	0.315	✓
	10:44:45.75	-01:20:55.19	0.7542	0.0002	3	68	502	0.653	
	10:44:44.09	-01:18:44.21	0.7621	0.0002	3	70	517	0.673	
	10:44:44.96	-01:21:06.79	0.7513	0.0002	3	75	551	0.717	
	10:44:43.84	-01:21:20.96	0.7545	0.0003	3	87	637	0.829	
	10:44:48.05	-01:18:53.71	0.7593	0.0002	3	89	654	0.851	
	10:44:39.02	-01:18:59.21	0.7618	0.0002	3	89	656	0.853	
	10:44:42.70	-01:21:23.01	0.7546	0.0003	3	90	662	0.861	
	10:44:40.76	-01:21:22.46	0.7509	0.0002	3	99	725	0.943	
	10:44:41.60	-01:21:50.44	0.7569	0.0002	3	120	885	1.151	
	10:44:44.87	-01:21:59.26	0.7511	0.0003	2	126	928	1.207	
	10:44:38.47	-01:21:47.44	0.7529	0.0002	3	138	1012	1.317	
	10:44:50.81	-01:17:48.06	0.7477	0.0002	3	165	1215	1.581	
	10:44:46.34	-01:17:11.01	0.7552	0.0003	2	168	1235	1.607	
	10:44:45.91	-01:22:44.46	0.7556	0.0006	1	173	1275	1.659	✓
	10:44:54.55	-01:17:24.82	0.7636	0.0004	2	221	1625	2.114	
XMMU J0002-3556 - cl04									
995	00:02:16.10	-35:56:33.79	0.7704						
	00:02:16.06	-35:56:31.92	0.7757	0.0002	3	2	14	0.014	
	00:02:16.55	-35:56:40.46	0.7629	0.0002	4	9	64	0.064	
	00:02:16.45	-35:56:23.33	0.7716	0.0002	3	11	84	0.084	
	00:02:16.74	-35:56:45.52	0.7786	0.0002	3	14	104	0.104	

Table B.1: Continued.

R_{200} (kpc)	RA (J2000)	DEC (J2000)	z	z_{err}	QF	Distance from X-ray centroid ($''$) (kpc) (r/R_{200})			Clipped out
	00:02:17.20	-35:56:10.59	0.7767	0.0002	3	27	198	0.199	
	00:02:15.60	-35:56:59.77	0.7812	0.0002	3	27	198	0.199	
	00:02:17.11	-35:57:11.12	0.7631	0.0002	4	39	291	0.292	
	00:02:19.60	-35:56:43.27	0.7662	0.0003	2	44	322	0.323	
	00:02:18.43	-35:55:42.85	0.7686	0.0002	3	58	432	0.434	
	00:02:13.17	-35:57:40.17	0.7660	0.0002	3	75	558	0.560	
	00:02:21.61	-35:57:12.78	0.7610	0.0002	2	77	573	0.575	
	00:02:12.14	-35:55:29.82	0.7726	0.0002	3	80	593	0.595	
	00:02:22.21	-35:57:41.61	0.7535	0.0002	3	101	745	0.748	✓
	00:02:23.36	-35:57:52.88	0.7710	0.0002	4	118	877	0.881	
XMMU J1243+1313 - cl05									
890	12:43:12.00	+13:13:09.59	0.7913						
	12:43:12.04	+13:13:10.06	0.7890	0.0002	4	1	6	0.007	
	12:43:12.27	+13:12:57.43	0.7883	0.0002	2	13	96	0.108	
	12:43:11.04	+13:13:15.56	0.7881	0.0002	3	15	114	0.128	
	12:43:12.84	+13:12:51.33	0.7951	0.0002	2	22	164	0.184	
	12:43:11.91	+13:13:41.82	0.7986	0.0002	3	32	241	0.271	
	12:43:09.84	+13:13:19.20	0.7883	0.0002	3	33	246	0.276	
	12:43:10.07	+13:12:46.10	0.7869	0.0002	3	37	274	0.308	
	12:43:09.58	+13:13:29.65	0.7965	0.0002	2	41	304	0.341	
	12:43:13.32	+13:12:23.79	0.7855	0.0002	3	50	372	0.418	
	12:43:08.65	+13:13:28.68	0.7944	0.0002	2	53	393	0.441	
	12:43:15.84	+13:12:46.21	0.7891	0.0002	4	61	454	0.510	

Table B.1: Continued.

R_{200} (kpc)	RA (J2000)	DEC (J2000)	z	z_{err}	QF	Distance from X-ray centroid (") (kpc) (r/ R_{200})			Clipped out
	12:43:07.34	+13:13:38.53	0.7973	0.0002	2	74	553	0.621	
	12:43:17.28	+13:12:56.39	0.7896	0.0002	4	78	585	0.657	
	12:43:05.99	+13:13:25.76	0.7881	0.0002	4	89	667	0.749	
	12:43:06.64	+13:14:11.63	0.7905	0.0002	2	100	747	0.839	
	12:43:18.87	+13:13:10.29	0.7906	0.0002	2	100	750	0.842	
	12:43:19.43	+13:12:55.46	0.7948	0.0002	3	109	819	0.920	
	12:43:19.90	+13:13:14.44	0.7868	0.0002	3	116	864	0.970	
	12:43:16.46	+13:11:18.53	0.8033	0.0002	3	129	963	1.081	
	12:43:03.51	+13:13:45.55	0.7934	0.0002	1	129	965	1.083	✓
	12:43:19.66	+13:11:59.99	0.7897	0.0002	4	132	985	1.106	
	12:43:17.71	+13:10:59.01	0.8000	0.0002	2	155	1159	1.301	
	12:43:23.40	+13:11:58.40	0.7858	0.0002	3	181	1354	1.520	
	12:43:22.60	+13:11:34.68	0.7899	0.0002	3	182	1358	1.525	
	12:43:22.74	+13:11:31.98	0.7962	0.0002	3	185	1381	1.550	
	12:43:25.67	+13:11:45.22	0.7937	0.0002	2	217	1621	1.820	
XMMU J0954+1738 - cl06									
952	09:54:17.10	+17:38:05.89	0.8276						
	09:54:16.57	+17:38:03.52	0.8219	0.0002	3	8	60	0.063	
	09:54:16.54	+17:38:09.70	0.8258	0.0002	4	9	68	0.071	
	09:54:18.54	+17:38:06.95	0.8253	0.0002	3	21	156	0.164	
	09:54:18.35	+17:38:25.06	0.8269	0.0002	2	26	199	0.209	
	09:54:15.00	+17:38:02.82	0.8335	0.0002	2	30	229	0.241	
	09:54:15.95	+17:37:33.58	0.8265	0.0002	4	36	275	0.289	

Table B.1: Continued.

R_{200} (kpc)	RA (J2000)	DEC (J2000)	z	z_{err}	QF	Distance from X-ray centroid			Clipped out
						($''$)	(kpc)	(r/R_{200})	
	09:54:18.10	+17:38:39.67	0.8324	0.0002	3	37	278	0.292	
	09:54:19.52	+17:38:25.27	0.8360	0.0002	3	40	301	0.316	
	09:54:17.72	+17:37:08.33	0.8166	0.0002	3	58	442	0.464	
	09:54:19.67	+17:38:52.95	0.8310	0.0002	3	60	453	0.476	
	09:54:15.90	+17:35:18.99	0.8233	0.0002	1	168	1274	1.338	✓
XMMU J0152-1338 - cl08									
811	01:52:41.30	-13:38:54.30	0.8289						
	01:52:41.34	-13:38:55.98	0.8307	0.0004	2	2	14	0.017	
	01:52:41.28	-13:38:57.65	0.8265	0.0012	1	3	26	0.032	✓
	01:52:41.12	-13:39:07.88	0.8303	0.0003	3	14	105	0.129	
	01:52:42.70	-13:38:59.13	0.8261	0.0002	4	21	160	0.197	
	01:52:39.42	-13:38:55.74	0.8233	0.0002	3	27	209	0.257	
	01:52:40.74	-13:39:21.01	0.8261	0.0003	2	28	212	0.261	
	01:52:40.18	-13:39:24.00	0.8307	0.0005	3	34	257	0.317	
	01:52:43.18	-13:38:29.43	0.8268	0.0002	3	37	281	0.346	
	01:52:35.82	-13:39:14.94	0.8326	0.0002	2	82	626	0.771	
	01:52:34.90	-13:39:29.40	0.8318	0.0002	1	100	757	0.933	✓
	01:52:47.19	-13:38:00.09	0.8256	0.0002	3	102	771	0.950	
	01:52:39.15	-13:40:31.43	0.8222	0.0005	1	102	775	0.955	✓
	01:52:36.99	-13:40:14.94	0.8324	0.0002	2	102	777	0.957	
	01:52:36.03	-13:40:15.85	0.8295	0.0002	3	112	851	1.048	
	01:52:32.85	-13:40:01.84	0.8279	0.0002	3	140	1067	1.315	

Table B.1: Continued.

R ₂₀₀ (kpc)	RA (J2000)	DEC (J2000)	z	z _{err}	QF	Distance from X-ray centroid ($''$) (kpc) (r/R ₂₀₀)		Clipped out
XMMU J2356-3441 - cl09								
1065	23:56:16.50	-34:41:41.79	0.9391					
	23:56:16.50	-34:41:38.42	0.9407	0.0002	3	3	27	0.025
	23:56:16.14	-34:41:36.61	0.9452	0.0002	3	7	54	0.051
	23:56:15.46	-34:41:39.26	0.9305	0.0003	3	13	103	0.097
	23:56:15.08	-34:41:29.36	0.9427	0.0002	3	22	170	0.160
	23:56:14.35	-34:41:22.22	0.9433	0.0003	4	33	260	0.244
	23:56:14.57	-34:41:00.70	0.9453	0.0002	3	47	374	0.351
	23:56:18.82	-34:41:01.50	0.9376	0.0003	3	49	390	0.366
	23:56:12.58	-34:41:22.38	0.9462	0.0002	4	52	411	0.386
	23:56:20.99	-34:41:55.14	0.9374	0.0002	3	57	448	0.420
	23:56:11.35	-34:41:38.43	0.9421	0.0002	4	64	501	0.470
	23:56:21.48	-34:41:59.02	0.9375	0.0005	3	64	503	0.472
	23:56:20.30	-34:40:57.36	0.9365	0.0002	3	65	509	0.478
	23:56:11.86	-34:40:59.34	0.9357	0.0002	3	71	562	0.527
	23:56:10.93	-34:40:53.16	0.9389	0.0002	2	84	663	0.622
	23:56:10.41	-34:40:49.56	0.9381	0.0002	4	91	721	0.677
	23:56:23.86	-34:41:56.21	0.9384	0.0002	3	92	724	0.679
	23:56:08.42	-34:41:16.29	0.9414	0.0002	4	103	810	0.760
	23:56:27.29	-34:41:48.55	0.9376	0.0002	3	133	1050	0.985
	23:56:03.74	-34:42:10.86	0.9356	0.0002	2	160	1261	1.183
	23:56:01.50	-34:41:19.36	0.9374	0.0002	3	186	1469	1.378

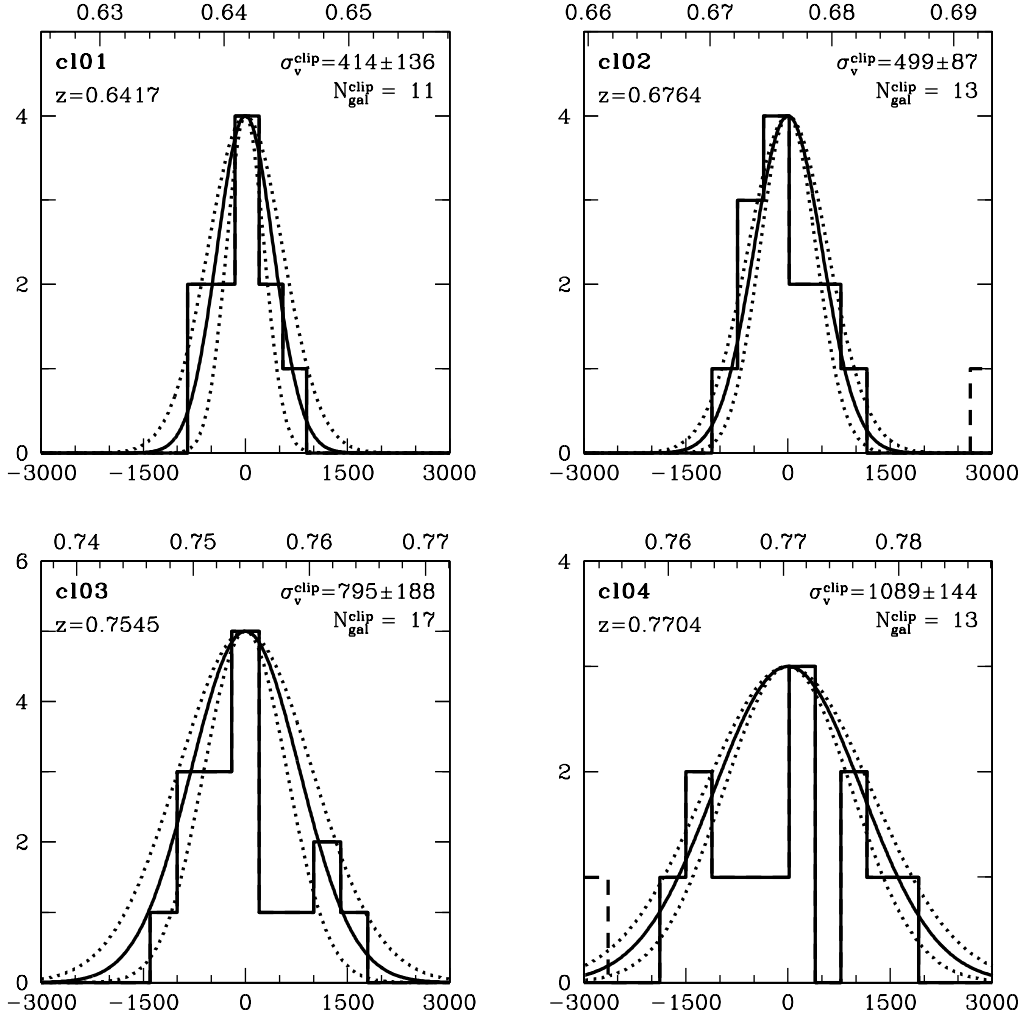


Figure B.1: Rest-frame velocity histograms of the first four (from c101 to c104) “XDCP sample” clusters listed in Tab. 6.2. On the bottom and top side of each panel the peculiar velocity (in km/s) and the redshift values are reported, respectively. In each panel the cluster ID, σ_v and its uncertainty, σ_{cl} and the number of the clipped members N_{cl} are indicated. The dashed histograms refer to those galaxies with peculiar velocities $|v| < 3000 \text{ km s}^{-1}$ from z_{cl} , but discarded as members by the iterative 3σ clipping process described in the text. The solid curve is the best gaussian fit of the distribution with variance equal to σ_v , whereas the dotted ones represent its $\pm 1\sigma$ uncertainty.

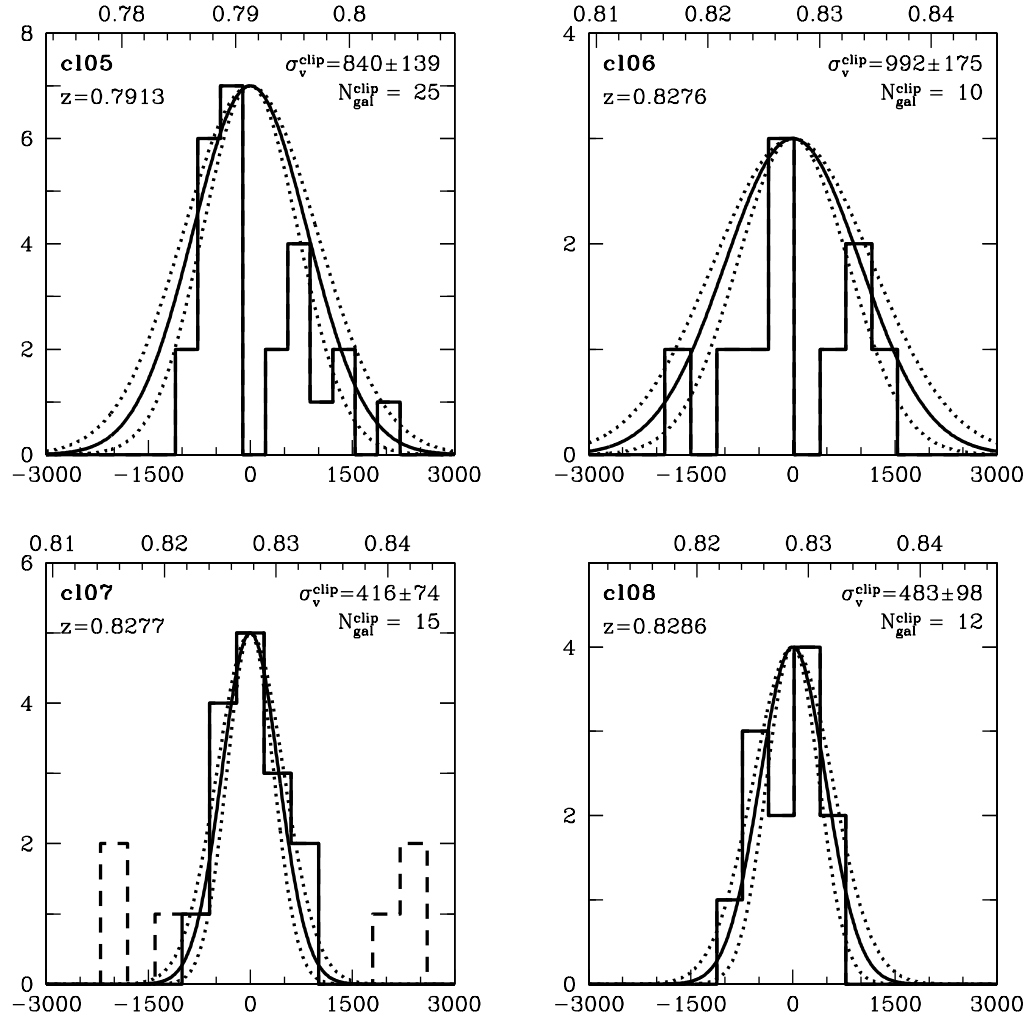


Figure B.2: as Fig. B.1, for cl05 to cl08.

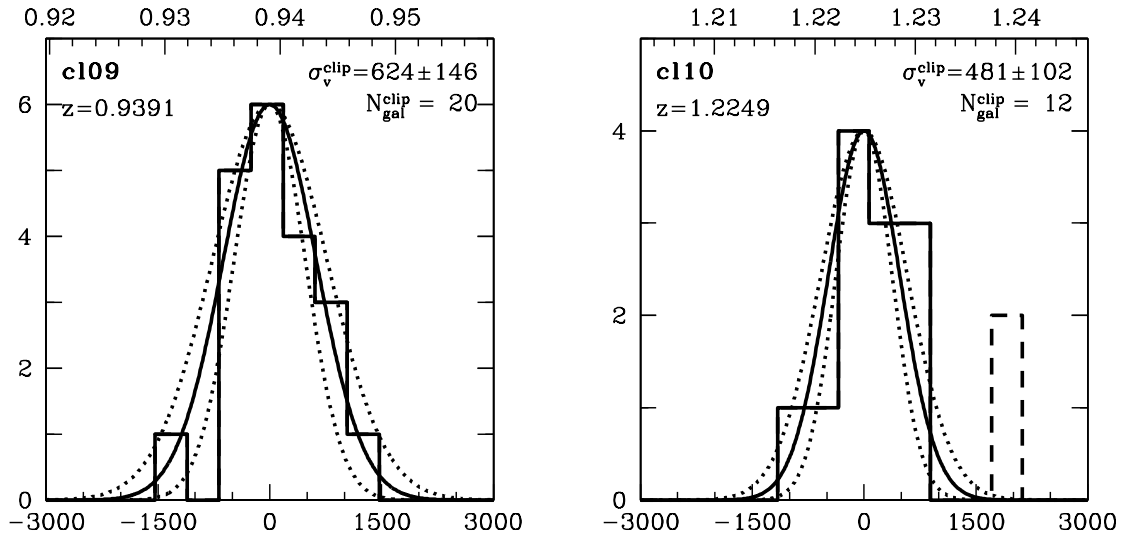


Figure B.3: as Fig. B.1, for c109 and c110.

Appendix C

Velocity histograms of “literature sample” clusters

In this Appendix I show the rest-frame velocity histograms of those 12 “literature sample” clusters with a public redshift set. As in Appendix B, I also overplot the best gaussian fit whose variance is the σ_v^{clip} computed with the method described in Sec. 6.6.2. I also report the σ_v^{lit} values and plot the corresponding gaussian fit in red.

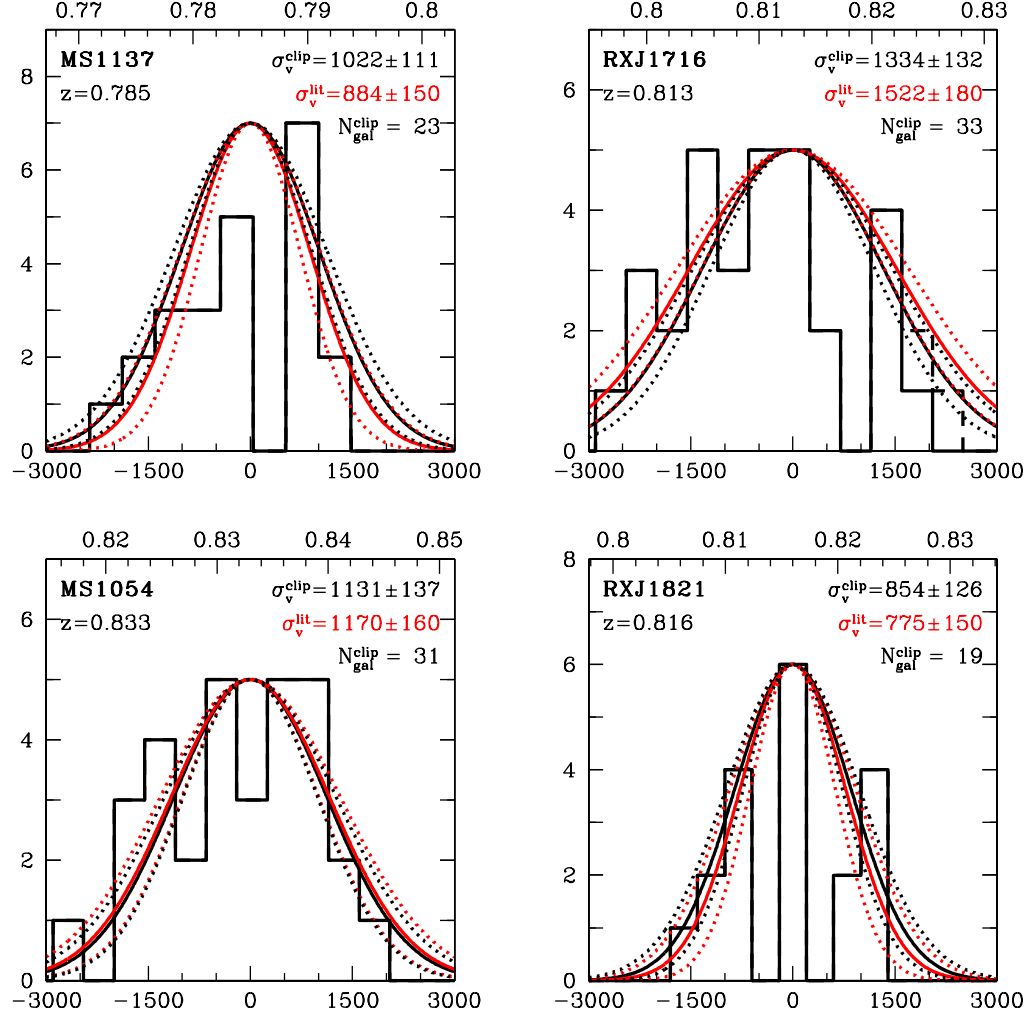


Figure C.1: Rest-frame velocity histograms of those “literature sample” clusters with a public redshift set. In addition to the same details present in Fig. B.1, here I also report, for each cluster, the public value of σ_v^{lit} (and its uncertainty) as listed in Tab. 6.3.1 and I show them with red gaussian curves. Albeit our analysis sometimes produced slightly different values of z_{cl} w.r.t. the ones stated by the authors, such differences are always limited to $c \cdot \Delta z_{\text{cl}} / (1 + z_{\text{cl}}) \lesssim 100 \text{ km s}^{-1}$ and hence the two gaussian curves of each cluster show the same central values. Our estimates of σ_v are, within the errors, in agreement with σ_v^{lit} , albeit sometimes the distributions are far from being gaussian (see e.g. SpARCS0035).

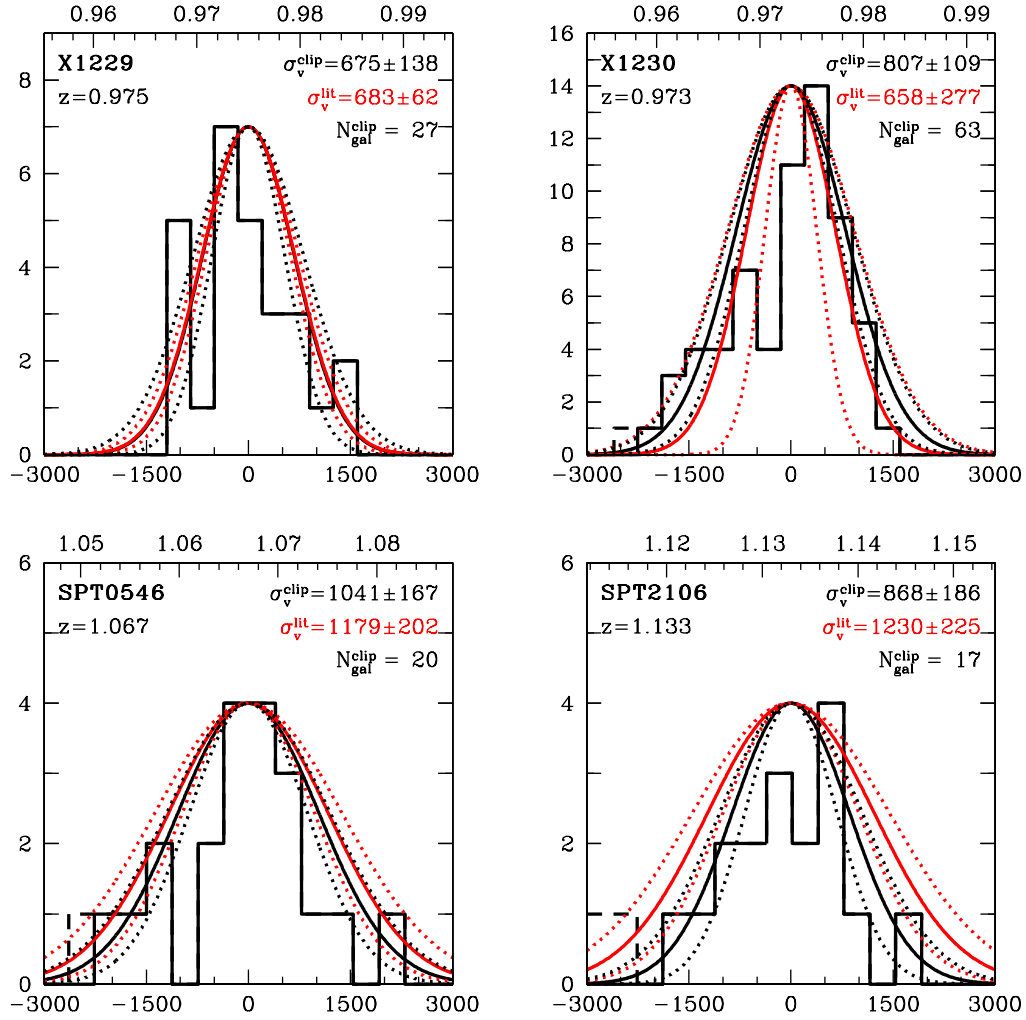


Figure C.2: as Fig. C.1

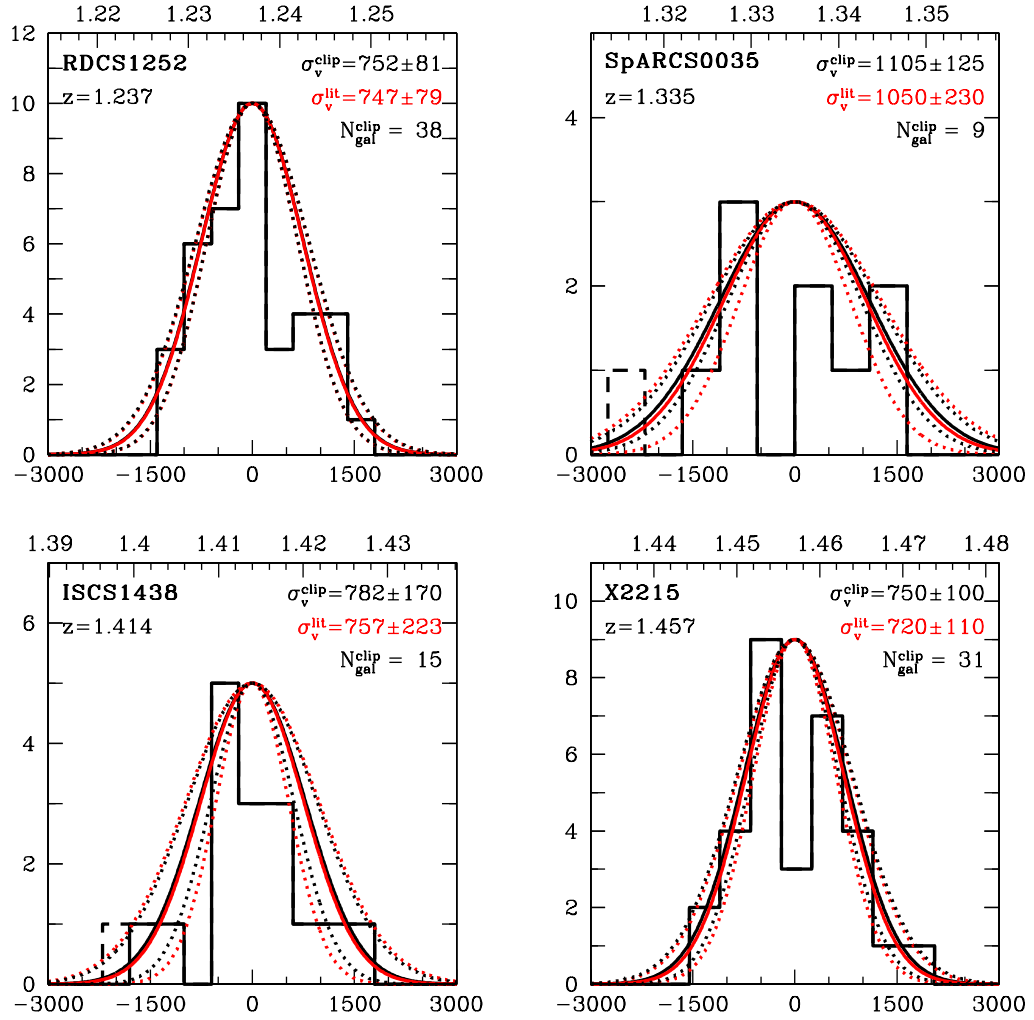


Figure C.3: as Fig. C.1

Acknowledgements

In the last three years I had the chance to get to know many people who preciousy contributed to achieve the present goal. First of all, I would like to thank my supervisor, Hans Böhringer, for his positive attitude, constant support, insightful advices, and several constructive discussions we had in these three years. You significantly helped me to grow as a scientist.

Secondly, I wish to warmly thank Rene Fassbender: your precious and fruitful collaboration provided me several tools for work and life in general. It was really a pleasure working together. I also owe to thank Daniele Pierini - thank you for your patience and the invaluable scientific and human support you gave me! - and Miguel Verdugo: thank you for the time you always were ready to spend for helping me. I wish also to thank Piero Rosati, Angela Bongiorno, Gayoung Chon, Robert Šuhada, and Martin Mühlegger for their precious collaboration and constructive discussions. I am also grateful to Jonny and Rob for their helpful advices on the English grammar kindly provided for this thesis.

In addition, I would like to thank those people who helped me to have a great time throughout the last three years. Thank you (H)Anna, Barbara, Giancarlo, Michele, and Viola, for the mutual support, the good chats and the passion for the good and typical food we have shared and cultivated in such a tireless way! Hope the distances will not prevent us to meet each other again in the future. I also wish to thank all my friends living far away because you never stopped to send me your support through the large distances.

Special thanks go to Annalisa: your (our) smiles always put me away from any trouble. Definitively you have been my easiest way toward serenity.

Finally, I owe very special thanks to my parents. Grazie per la costante fiducia che mi avete sempre dimostrato in questi anni e il sacrificio, lo so bene, di vedermi sempre di più lontano. Nulla avrebbe potuto realizzarsi senza di voi.

Bibliography

Abell, G. O. 1958, ApJS, 3, 211

Akritas, M. G. & Bershadsky, M. A. 1996, ApJ, 470, 706

Andernach, H., Tago, E., Einasto, M., Einasto, J., & Jaaniste, J. 2005, in *Astronomical Society of the Pacific Conference Series*, Vol. 329, *Nearby Large-Scale Structures and the Zone of Avoidance*, ed. A. P. Fairall & P. A. Woudt, 283–287

Andersson, K., Benson, B. A., Ade, P. A. R., et al. 2011, ApJ, 738, 48

Angulo, R. E., Springel, V., White, S. D. M., et al. 2012, ArXiv e-prints

Appenzeller, I., Fricke, K., Fürtig, W., et al. 1998, *The Messenger*, 94, 1

Arnaud, M., Pointecouteau, E., & Pratt, G. W. 2005, A&A, 441, 893

Arnaud, M., Pointecouteau, E., & Pratt, G. W. 2007, A&A, 474, L37

Bahcall, N. A. & Fan, X. 1998, ApJ, 504, 1

Bailer-Jones, C. A., Bizenberger, P., & Storz, C. 2000, in *Presented at the Society of Photo-Optical Instrumentation Engineers (SPIE) Conference*, Vol. 4008, *Society of Photo-Optical Instrumentation Engineers (SPIE) Conference Series*, ed. M. Iye & A. F. Moorwood, 1305–1316

Balogh, M. L., Baldry, I. K., Nichol, R., et al. 2004, ApJ, 615, L101

Balogh, M. L., Morris, S. L., Yee, H. K. C., Carlberg, R. G., & Ellingson, E. 1999, ApJ, 527, 54

Bartelmann, M. 1996, A&A, 313, 697

Baum, W. A. 1959, PASP, 71, 106

- Beers, T. C., Flynn, K., & Gebhardt, K. 1990, *AJ*, 100, 32
- Bertin, E. & Arnouts, S. 1996, *A&AS*, 117, 393
- Birkinshaw, M., Hughes, J. P., & Arnaud, K. A. 1991, *ApJ*, 379, 466
- Biviano, A., Murante, G., Borgani, S., et al. 2006, *A&A*, 456, 23
- Böhringer, H., Mullis, C. R., Rosati, P., et al. 2005, *ESO Messenger*, 120, 33
- Böhringer, H., Schuecker, P., Guzzo, L., et al. 2004, *A&A*, 425, 367
- Böhringer, H., Schwarz, R. A., & Briel, U. G. 1993, 368
- Böhringer, H., Voges, W., Huchra, J. P., et al. 2000, *ApJS*, 129, 435
- Bongiorno, A., Mignoli, M., Zamorani, G., et al. 2010, *A&A*, 510, A56
- Borgani, S. 2006, [arXiv:astro-ph/0605575](https://arxiv.org/abs/astro-ph/0605575)
- Borgani, S., Rosati, P., della Ceca, R., Tozzi, P., & Norman, C. 2000, in *Large Scale Structure in the X-ray Universe, Proceedings of the 20-22 September 1999 Workshop*, Santorini, Greece, eds. Plionis, M. & Georgantopoulos, I., Atlantisciences, Paris, France, ed. M. Plionis & I. Georgantopoulos, 167
- Boselli, A. & Gavazzi, G. 2006, *PASP*, 118, 517
- Bower, R. G., Lucey, J. R., & Ellis, R. S. 1992, *MNRAS*, 254, 601
- Bradač, M., Allen, S. W., Treu, T., et al. 2008, *ApJ*, 687, 959
- Briel, U. G., Henry, J. P., & Boehringer, H. 1992, *A&A*, 259, L31
- Brodwin, M., Ruel, J., Ade, P. A. R., et al. 2010, *ApJ*, 721, 90
- Butcher, H. & Oemler, Jr., A. 1978, *ApJ*, 219, 18
- Carlstrom, J. E., Ade, P. A. R., Aird, K. A., et al. 2011, *PASP*, 123, 568
- Cavaliere, A., Lapi, A., & Menci, N. 2002, *ApJ*, 581, L1
- Cimatti, A., Daddi, E., Renzini, A., et al. 2004, *Nature*, 430, 184
- Collins, C. A., Stott, J. P., Hilton, M., et al. 2009, *Nature*, 458, 603

- Cowie, L. L., Songaila, A., Hu, E. M., & Cohen, J. G. 1996, *AJ*, 112, 839
- Cutri, R. M., Skrutskie, M. F., van Dyk, S., et al. 2003, 2MASS All Sky Catalog of point sources. (The IRSA 2MASS All-Sky Point Source Catalog, NASA/IPAC Infrared Science Archive)
- Danese, L., de Zotti, G., & di Tullio, G. 1980, *A&A*, 82, 322
- De Lucia, G. & Blaizot, J. 2007, *MNRAS*, 375, 2
- de Propriis, R., Eisenhardt, P. R., Stanford, S. A., & Dickinson, M. 1998, *ApJ*, 503, L45
- Dicker, S. R., Korngut, P. M., Mason, B. S., et al. 2008, in Society of Photo-Optical Instrumentation Engineers (SPIE) Conference Series, Vol. 7020, Society of Photo-Optical Instrumentation Engineers (SPIE) Conference Series
- Dickinson, M., Papovich, C., Ferguson, H. C., & Budavári, T. 2003, *ApJ*, 587, 25
- Donahue, M., Voit, G. M., Gioia, I., et al. 1998, *ApJ*, 502, 550
- Donahue, M., Voit, G. M., Scharf, C. A., et al. 1999, *ApJ*, 527, 525
- Drory, N., Feulner, G., Bender, R., et al. 2001, *MNRAS*, 325, 550
- Eisenhardt, P. R., De Propriis, R., Gonzalez, A. H., et al. 2007, *ApJS*, 169, 225
- Eisenstein, D. J., Hogg, D. W., Fukugita, M., et al. 2003, *ApJ*, 585, 694
- Ettori, S., Tozzi, P., Borgani, S., & Rosati, P. 2004, *A&A*, 417, 13
- Fabian, A. C., Crawford, C. S., Edge, A. C., & Mushotzky, R. F. 1994, *MNRAS*, 267, 779
- Fabian, A. C., Nulsen, P. E. J., & Canizares, C. R. 1991, *A&A Rev.*, 2, 191
- Fassbender, R. 2007, Phd thesis, Ludwig-Maximilians-Universität München, astro-ph/0806.0861
- Fassbender, R., Böhringer, H., Nastasi, A., et al. 2011a, *New Journal of Physics*, 13, 125014
- Fassbender, R., Böhringer, H., Santos, J. S., et al. 2011b, *A&A*, 527, A78

- Fassbender, R., Nastasi, A., Böhringer, H., et al. 2011c, *A&A*, 527, 10
- Fioc, M. & Rocca-Volmerange, B. 1997, *A&A*, 326, 950
- Foley, R. J., Andersson, K., Bazin, G., et al. 2011, *ApJ*, 731, 86
- Franzetti, P., Scodeggio, M., Garilli, B., et al. 2007, *A&A*, 465, 711
- Gallazzi, A. & Bell, E. F. 2009, *ApJS*, 185, 253
- Gallazzi, A., Charlot, S., Brinchmann, J., White, S. D. M., & Tremonti, C. A. 2005, *MNRAS*, 362, 41
- Garilli, B., Fumana, M., Franzetti, P., et al. 2010, *PASP*, 122, 827
- Gavazzi, G., Pierini, D., & Boselli, A. 1996, *A&A*, 312, 397
- Gavazzi, G. & Scodeggio, M. 1996, *A&A*, 312, L29
- Giodini, S., Pierini, D., Finoguenov, A., et al. 2009, *ApJ*, 703, 982
- Gioia, I. M., Henry, J. P., Maccacaro, T., et al. 1990, *ApJ*, 356, L35
- Gioia, I. M., Henry, J. P., Mullis, C. R., Ebeling, H., & Wolter, A. 1999, *AJ*, 117, 2608
- Gioia, I. M., Wolter, A., Mullis, C. R., et al. 2004, *A&A*, 428, 867
- Gladders, M. D. & Yee, H. K. C. 2005, *ApJS*, 157, 1
- Gobat, R., Daddi, E., Onodera, M., et al. 2011, *A&A*, 526, 133
- Gobat, R., Rosati, P., Strazzullo, V., et al. 2008, *A&A*, 488, 853
- Guennou, L., Adami, C., Ulmer, M. P., et al. 2010, *A&A*, 523, A21
- Gunn, J. E. & Gott, J. R. I. 1972, *ApJ*, 176, 1
- Guth, A. H. 1981, *Phys. Rev. D*, 23, 347
- Haarsma, D. B., Leisman, L., Donahue, M., et al. 2010, *ApJ*, 713, 1037
- Halliday, C., Milvang-Jensen, B., Poirier, S., et al. 2004, *A&A*, 427, 397
- Harrison, E. R. 1970, *Phys. Rev. D*, 1, 2726

- Henry, J. P., Evrard, A. E., Hoekstra, H., Babul, A., & Mahdavi, A. 2009, *ApJ*, 691, 1307
- Henry, J. P., Gioia, I. M., Maccacaro, T., et al. 1992, *ApJ*, 386, 408
- Hilton, M., Lloyd-Davies, E., Stanford, S. A., et al. 2010, *ApJ*, 718, 133
- Hilton, M., Stanford, S. A., Stott, J. P., et al. 2009, *ApJ*, 697, 436
- Hopkins, A. M. & Beacom, J. F. 2006, *ApJ*, 651, 142
- Hopkins, P. F., Cox, T. J., Kereš, D., & Hernquist, L. 2008, *ApJS*, 175, 390
- Horne, K. 1986, *PASP*, 98, 609
- Jenkins, A., Frenk, C. S., White, S. D. M., et al. 2001, *MNRAS*, 321, 372
- Juneau, S., Glazebrook, K., Crampton, D., et al. 2005, *ApJ*, 619, L135
- Kaiser, N. 1986, *MNRAS*, 222, 323
- Kalberla, P. M. W., Burton, W. B., Hartmann, D., et al. 2005, *A&A*, 440, 775
- Kenney, J. D. P., van Gorkom, J. H., & Vollmer, B. 2004, *AJ*, 127, 3361
- Kinney, A. L., Calzetti, D., Bohlin, R. C., et al. 1996, *ApJ*, 467, 38
- Komatsu, E., Smith, K. M., Dunkley, J., et al. 2011, *ApJS*, 192, 18
- Kravtsov, A. V., Vikhlinin, A., & Nagai, D. 2006, *ApJ*, 650, 128
- Lamareille, F., Mouhcine, M., Contini, T., Lewis, I., & Maddox, S. 2004, *MNRAS*, 350, 396
- Le Fèvre, O., Mellier, Y., McCracken, H. J., et al. 2004, *A&A*, 417, 839
- Lerchster, M., Seitz, S., Brimiouille, F., et al. 2011, *MNRAS*, 411, 2667
- Lidman, C., Rosati, P., Tanaka, M., et al. 2008, *A&A*, 489, 981
- Lilly, S. J., Le Fèvre, O., Renzini, A., et al. 2007, *ApJS*, 172, 70
- Longair, M. S., ed. 1998, *Galaxy formation*
- Lubin, L. M., Mulchaey, J. S., & Postman, M. 2004, *ApJ*, 601, L9

- Mantz, A., Allen, S. W., Ebeling, H., Rapetti, D., & Drlica-Wagner, A. 2010, *MNRAS*, 406, 1773
- Marriage, T. A., Acquaviva, V., Ade, P. A. R., et al. 2011, *ApJ*, 737, 61
- McDonald, M., Bayliss, M., Benson, B. A., et al. 2012, *Nature*, 488, 349
- Menanteau, F., Hughes, J. P., Barrientos, L. F., et al. 2010, *ApJS*, 191, 340
- Menanteau, F., Hughes, J. P., Sifón, C., et al. 2012, *ApJ*, 748, 7
- Mignoli, M., Cimatti, A., Zamorani, G., et al. 2005, *A&A*, 437, 883
- Mihos, J. C., Harding, P., Feldmeier, J., & Morrison, H. 2005, *ApJ*, 631, L41
- Milvang-Jensen, B., Noll, S., Halliday, C., et al. 2008, *A&A*, 482, 419
- Mühlegger, M. 2010, PhD Thesis TU München
- Mullis, C. R., Rosati, P., Lamer, G., et al. 2005, *ApJ*, 623, L85
- Mushotzky, R. F. 1984, *Physica Scripta Volume T*, 7, 157
- Nastasi, A., Fassbender, R., Böhringer, H., et al. 2011, *A&A*, 532, L6
- Nastasi, A., Scodeggio, M., Fassbender, R., et al. 2013, *ArXiv e-prints*
- Navarro, J. F., Frenk, C. S., & White, S. D. M. 1997, *ApJ*, 490, 493
- Ortiz-Gil, A., Guzzo, L., Schuecker, P., Böhringer, H., & Collins, C. A. 2004, *MNRAS*, 348, 325
- Padmanabhan, T. 1993, *Structure Formation in the Universe*
- Pannella, M., Carilli, C. L., Daddi, E., et al. 2009, *ApJ*, 698, L116
- Papovich, C., Momcheva, I., Willmer, C. N. A., et al. 2010, *ApJ*, 716, 1503
- Patel, S. G., Holden, B. P., Kelson, D. D., Illingworth, G. D., & Franx, M. 2009, *ApJ*, 705, L67
- Peacock, J. A. 1999, *Cosmological Physics* (*Cosmological Physics*, by John A. Peacock, pp. 704. ISBN 052141072X. Cambridge, UK: Cambridge University Press, January 1999.)

- Peebles, P. J. E. 1993, *Principles of Physical Cosmology*
- Perlmutter, S., Aldering, G., Goldhaber, G., et al. 1999, *ApJ*, 517, 565
- Piccinotti, G., Mushotzky, R. F., Boldt, E. A., et al. 1982, *ApJ*, 253, 485
- Pierini, D., Maraston, C., Bender, R., & Witt, A. N. 2004, *MNRAS*, 347, 1
- Pierini, D., Šuhada, R., Fassbender, R., et al. 2012, *A&A*, 540, A45
- Planck Collaboration, Ade, P. A. R., Aghanim, N., et al. 2011a, *A&A*, 536, A1
- Planck Collaboration, Ade, P. A. R., Aghanim, N., et al. 2011b, *A&A*, 536, A8
- Poggianti, B. M., Aragón-Salamanca, A., Zaritsky, D., et al. 2009, *ApJ*, 693, 112
- Pratt, G. W., Croston, J. H., Arnaud, M., & Böhringer, H. 2009, *A&A*, 498, 361
- Press, W. H. & Schechter, P. 1974, *ApJ*, 187, 425
- Puchwein, E., Sijacki, D., & Springel, V. 2008, *ApJ*, 687, L53
- Reichert, A., Böhringer, H., Fassbender, R., & Mühlegger, M. 2011, *A&A*, 535, A4
- Reiprich, T. H. & Böhringer, H. 2002, *ApJ*, 567, 716
- Reiss, D. J., Germany, L. M., Schmidt, B. P., & Stubbs, C. W. 1998, *AJ*, 115, 26
- Rettura, A., Rosati, P., Nonino, M., et al. 2010, *ApJ*, 709, 512
- Ricker, P. M. & Sarazin, C. L. 2001, *ApJ*, 561, 621
- Riess, A. G., Macri, L., Casertano, S., et al. 2011, *ApJ*, 730, 119
- Romeo, A. D., Napolitano, N. R., Covone, G., et al. 2008, *MNRAS*, 389, 13
- Rosati, P. 2001, in *ASP Conf. Ser. 234: X-ray Astronomy 2000*, 363
- Rosati, P., Borgani, S., Gilli, R., et al. 2011, *Memorie della Societa Astronomica Italiana Supplementi*, 17, 8
- Rosati, P., della Ceca, R., Norman, C., & Giacconi, R. 1998, *ApJ*, 492, L21
- Rosati, P., Stanford, S. A., Eisenhardt, P. R., et al. 1999, *AJ*, 118, 76

- Rosati, P., Tozzi, P., Ettori, S., et al. 2004, *AJ*, 127, 230
- Salpeter, E. E. 1955, *ApJ*, 121, 161
- Santos, J. S., Fassbender, R., Nastasi, A., et al. 2011, *ArXiv e-prints*
- Santos, J. S., Rosati, P., Gobat, R., et al. 2009, *A&A*, 501, 49
- Saro, A., Bazin, G., Mohr, J., & Dolag, K. 2012, *ArXiv e-prints*
- Scodeggio, M., Franzetti, P., Garilli, B., et al. 2005, *PASP*, 117, 1284
- Scodeggio, M., Zanichelli, A., Garilli, B., Le Fèvre, O., & Vettolani, G. 2001, in *Astronomical Society of the Pacific Conference Series*, Vol. 238, *Astronomical Data Analysis Software and Systems X*, ed. F. R. Harnden Jr., F. A. Primini, & H. E. Payne, 451
- Sifon, C., Menanteau, F., Hasselfield, M., et al. 2012, *ArXiv e-prints*
- Smith, G. P., Khosroshahi, H. G., Dariush, A., et al. 2010, *MNRAS*, 409, 169
- Smith, J. A., Tucker, D. L., Kent, S., et al. 2002, *AJ*, 123, 2121
- Springel, V., White, S. D. M., Jenkins, A., et al. 2005, *Nature*, 435, 629
- Stanford, S. A., Elston, R., Eisenhardt, P. R., et al. 1997, *AJ*, 114, 2232
- Steidel, C. C., Shapley, A. E., Pettini, M., et al. 2004, *ApJ*, 604, 534
- Strazzullo, V., Rosati, P., Pannella, M., et al. 2010, *A&A*, 524, 17
- Strazzullo, V., Rosati, P., Stanford, S. A., et al. 2006, *A&A*, 450, 909
- Sunyaev, R. A. & Zel'dovich, Y. B. 1972, *Comments on Astrophysics and Space Physics*, 4, 173
- Tanaka, M., Finoguenov, A., & Ueda, Y. 2010, *ApJ*, 716, L152
- Testi, L. 2010, *Memorie della Societa Astronomica Italiana Supplementi*, 14, 90
- Thomas, D., Maraston, C., Bender, R., & Mendes de Oliveira, C. 2005, *ApJ*, 621, 673
- Thomas, D., Maraston, C., Schawinski, K., Sarzi, M., & Silk, J. 2010, *MNRAS*, 404, 1775

- Tran, K., Papovich, C., Saintonge, A., et al. 2010, *ApJ*, 719, L126
- Tran, K.-V. H., Kelson, D. D., van Dokkum, P., et al. 1999, *ApJ*, 522, 39
- Truemper, J. 1992, *QJRAS*, 33, 165
- Vanderlinde, K., Crawford, T. M., de Haan, T., et al. 2010, *arXiv:1003.0003*
- Voit, G. M. 2005, *Reviews of Modern Physics*, 77, 207
- Whiley, I. M., Aragón-Salamanca, A., De Lucia, G., et al. 2008, *MNRAS*, 387, 1253
- White, M., Cohn, J. D., & Smit, R. 2010, *MNRAS*, 408, 1818
- White, S. D. M., Navarro, J. F., Evrard, A. E., & Frenk, C. S. 1993, *Nature*, 366, 429
- Williamson, R., Benson, B. A., High, F. W., et al. 2011, *ApJ*, 738, 139
- Wilman, D. J., Pierini, D., Tyler, K., et al. 2008, *ApJ*, 680, 1009
- Wilson, G., Muzzin, A., Lacy, M., et al. 2006, *Astronomy*
- Wilson, G., Muzzin, A., Yee, H. K. C., et al. 2009, *ApJ*, 698, 1943
- Wittman, D., Dell’Antonio, I. P., Hughes, J. P., et al. 2006, *ApJ*, 643, 128
- Worthey, G. & Ottaviani, D. L. 1997, *ApJS*, 111, 377
- Wu, X.-P., Xue, Y.-J., & Fang, L.-Z. 1999, *ApJ*, 524, 22
- Zeldovich, Y. B. 1972, *MNRAS*, 160, 1P
- Zhang, Y.-Y., Andernach, H., Caretta, C. A., et al. 2011, *A&A*, 526, A105
- Zwicky, F., Herzog, E., & Wild, P. 1968, *Catalogue of galaxies and of clusters of galaxies*

Curriculum vitae

Personal

Date of birth 09 March 1983
Place of birth Erice (Trapani)
Nationality Italian

Education

2009 - 2012 PhD student of the International Max Planck Research School at the Max-Planck-Institut für extraterrestrische Physik (Garching bei München, Germany).
Thesis topic: Multiwavelength study of distant galaxy clusters.
Supervisor: Prof. Dr. Hans Böhringer

2009 Master degree in Astrophysics and Cosmology at the University of Bologna.
Grade: 110/110 cum Laude.
Thesis Topic: Study of the relations between Star formation activity, morphology and AGN activity for a sample of GMASS massive galaxies at $1 \leq z \leq 3$.
Supervisor: Prof. Dr. Andrea Cimatti

2006 Bachelor degree in Astronomy at the University of Bologna.
Grade: 107/110.
Thesis topic: New hypothesis on the role of Pop III stars in the early universe.
Supervisor: Prof. Dr. Corrado Bartolini

2001 High School Diploma.
Grade: 100/100

Publications

1. 2013 - *F-VIPGI, a new adapted version of VIPGI for FORS2 spectroscopy. Application to a sample of 16 X-ray selected galaxy clusters at $0.6 \leq z \leq 1.2$* , **Nastasi, A.**; Scodeggio, M.; Fassbender, R.; Böhringer, H.; Pierini, D.; Verdugo, M.; Garilli, B.M. and Franzetti, P., A&A in press, arXiv:1301.2327
2. 2012 - *AGN triggering in the infall regions of distant X-ray luminous galaxy clusters at $0.9 < z \leq 1.6$* , Fassbender, R. and Šuhada, R. and **Nastasi, A.**, Advances in Astronomy, vol. 2012, Article ID 138380, 15 pages, 2012. doi:10.1155/2012/138380
3. 2012 - *First simultaneous optical/near-infrared imaging of an X-ray selected, high-redshift cluster of galaxies with GROND. The galaxy population of XMMU J0338.7 + 0030 at $z = 1.1$* , Pierini, D., Šuhada, R., Fassbender, R., **Nastasi, A.**, Böhringer, H.; Salvato, M.; Pratt, G. W.; Lerchster, M.; Rosati, P.; Santos, J. S.; de Hoon, A.; Kohnert, J.; Lamer, G.; Mohr, J. J.; Mühlegger, M.; Quintana, H.; Schwope, A.; Biffi, V.; Chon, G.; Giodini, S.; Koppenhoefer, J.; Verdugo, M.; Ziparo, F.; Afonso, P. M. J.; Clemens, C.; Greiner, J.; Krühler, T.; Küpcü Yoldaş, A.; Olivares E., F.; Rossi, A.; Yoldaş, A., A&A, 540, A45
4. 2011 - *The X-ray luminous galaxy cluster population at $0.9 < z \lesssim 1.6$ as revealed by the XMM-Newton Distant Cluster Project*, Fassbender, R.; Böhringer, H.; **Nastasi, A.**; Šuhada, R.; Mühlegger, M.; de Hoon, A.; Kohnert, J.; Lamer, G.; Mohr, J. J.; Pierini, D.; Pratt, G. W.; Quintana, H.; Rosati, P.; Santos, J. S.; Schwope, A. D., NJP, 13 (2011) 125014
5. 2011 - *Discovery of the X-ray selected galaxy cluster XMMU J0338.8+0021 at $z = 1.49$. Indications of a young system with a brightest galaxy in formation*, **Nastasi, A.**; Fassbender, R.; Böhringer, H.; Šuhada, R.; Rosati, P.; Pierini, D.; Verdugo, M.; Santos, J. S.; Schwope, A. D.; de Hoon, A.; Kohnert, J.; Lamer, G.; Mühlegger, M.; Quintana, H., A&A, 532, L6
6. 2011 - *Discovery of a massive X-ray luminous galaxy cluster at $z = 1.579$* , Santos, J. S.; Fassbender, R.; **Nastasi, A.**; Böhringer, H.; Rosati, P.; Šuhada, R.; Pierini, D.; Nonino, M.; Mühlegger, M.; Quintana, H.; Schwope, A. D.; Lamer, G.; de Hoon, A.; Strazzullo, V., A&A, 531, L15
7. 2011 - *Exploring the galaxy cluster-group transition regime at high redshifts. Physical properties of two newly detected $z > 1$ systems*,

Šuhada, R.; Fassbender, R.; **Nastasi, A.**; Böhringer, H.; de Hoon, A.; Pierini, D.; Santos, J. S.; Rosati, P.; Mühlegger, M.; Quintana, H.; Schwobe, A. D.; Lamer, G.; Kohnert, J.; Pratt, G. W., *A&A*, 530, A110

8. 2011 - *The X-ray luminous galaxy cluster XMMU J1007.4+1237 at $z = 1.56$. The dawn of starburst activity in cluster cores*,
Fassbender, R.; **Nastasi, A.**; Böhringer, H.; Šuhada, R.; Santos, J. S.; Rosati, P.; Pierini, D.; Mühlegger, M.; Quintana, H.; Schwobe, A. D.; Lamer, G.; de Hoon, A.; Kohnert, J.; Pratt, G. W.; Mohr, J. J., *A&A*, 527, L10
9. 2011 - *A pan-chromatic view of the galaxy cluster XMMU J1230.3+1339 at $z = 0.975$. Observing the assembly of a massive system*,
Fassbender, R.; Böhringer, H.; Santos, J. S.; Pratt, G. W.; Šuhada, R.; Kohnert, J.; Lerchster, M.; Rovilos, E.; Pierini, D.; Chon, G.; Schwobe, A. D.; Lamer, G.; Mühlegger, M.; Rosati, P.; Quintana, H.; **Nastasi, A.**; de Hoon, A.; Seitz, S.; Mohr, J. J., *A&A*, 527, A78